UNIVERSITÀ
degli STUDI
di CATANIA

Dipartimento
di Fisica
e Astronomia
"Ettore Majorana"

PhD programme in physics

Simone Amaducci

Accurate measurement of the ^{235}U(n,f) cross section at n_TOF between thermal energy and 170 keV, relative to ^{6}Li(n,t) and ^{10}B(n,α)

PhD thesis

Supervisors:
Chiar.mo Prof. S. Cherubini
Dr. L. Cosentino

---

academic year 2019/2020

Sai cos'è la nostra vita? La tua e la mia? Un sogno fatto in Sicilia. Forse stiamo ancora lì e stiamo sognando.

Leonardo Sciascia
[Candido ovvero un sogno fatto in Sicilia]

L'aereo, ah, l'aereo è invece alluminio lucente, l'aereo è davvero saltare il fosso,
l'aereo è sempre "The Spirit of Saint Louis", "Barone Rosso"
e allora ti prende quella voglia di volare che ti fa gridare in un giorno sfinito,
di quando vedi un jumbo decollare e sembra che s' innalzi all'infinito.

Francesco Guccini
[Argentina]

Contents

Introduction

Since its discovery in the late '30s, neutron induced nuclear fission of ^{235}U revolutionized the human society because of profound civil and military implications that followed. Being the ^{235}U the only fissile element found in appreciable quantities in nature, its fission reaction has been extensively studied in past decades. The main civil application is represented by the production of electricity that in the future can provide a fundamental contribution to the easing of the greenhouse effect. In fact nuclear fission represents a continuous and reliable source of energy with low production of carbon dioxide, that is able to work in synergy with the renewable. The great part of present days nuclear reactors use enriched uranium as fuel, even if safety reasons as well as handling and long-term disposal of nuclear waste, currently represent the main limit to the growth of nuclear power. New generation nuclear reactors, such as the Fast Reactors or the Accelerator-Driven Systems, can represent a turning point because of their high intrinsic safety and lower radiotoxicity. Their ability to burn the long-term nuclei can drastically improve the nuclear waste cycle, increasing the efficiency and reducing the amount of nuclear waste requiring long-term disposal. However, these crucial steps forward require a highly accurate knowledge of the ^{235}U(n,f) reaction in a wide energy range as well as the ones of the many the actinides to be burned.

Besides, the ^{235}U(n,f) cross section is one of the most important neutron standard, *i.e.* a restrict group of very well known cross sections, which are employed as reference for measuring neutron induced cross sections and for measuring neutron fluxes. International agencies as

Cross Section Evaluation Working Group (CSEWG) and the International Atomic Energy Agency (IAEA) cooperatively manage the definition of the standard cross sections and periodically update their values, on the basis of the available experimental data. The role of the standard neutron data is therefore relevant to ensure high quality nuclear data, being their accuracy limited by the uncertainty of the employed reference. Improving the accuracy of a widespread standard cross section, such as for ^{235}U(n,f), can have a significant impact over a large number of measurements that use it as a reference.

In addition to the technological applications, the accurate knowledge of the neutron induced fission cross sections on ^{235}U and other actinides isotopes is fundamental to refine the theoretical models, which require systematic measurements of the fission chain reactions. Reliable fission models has important implications in several scientific fields. Among these, the fission recycling process occurring in the scenario of the nucleosynthesis in explosive environments of neutron star mergers, represents the state of the art of the multi-messenger astronomy. In fact, it is well ascertained that the fission recycling plays a major role into the determination of the final element abundances.

The definition of a standard neutron cross section includes one, or many, well defined energy interval where its use is recommended. In particular, the ^{235}U fission is considered a standard for thermal neutrons (E_n = 0.0253 eV), in the integral from 7.8 eV to 11 eV and over the interval ranging from 150 keV to 200 MeV. Even though below 150 keV this cross section is not a standard, it is usually employed as reference to measure the cross section of neutron induced reactions, especially for the actinides. Recently, significant discrepancies in the order of 5-10% were found in the interval between 10 keV and 30 keV in some measurements employing the ^{235}U(n,f) as reference, including the n_TOF flux [1] and the ^{235}U(n,γ) cross section measurement by Jandel *et al.* [2]. The need to clarify the origin of these inconsistencies, motivated a new accurate measurement of ^{235}U(n,f) cross section at n_TOF, in the energy range from thermal to 170 keV. This measurement represents also an opportunity to improve the accuracy of the ^{235}U(n,f) data in this low energy range, providing new datasets to the evaluators to further refine this cross section. The measurement was carried out adopting the so-called *Ratio Method* technique, by employing

the reactions ^{6}Li(n,t) and ^{10}B(n,α) as references, whose cross sections are standard from thermal to 1 MeV.

The Thesis is organized as follows: Chapter 1 provides a brief description of the fission process. Theoretical models are briefly reviewed and the general framework of standard neutron cross sections with its implications in experimental physics is discussed. In the sections 1.3 the areas of interest for which the present measurement is especially relevant are presented, *i.e.* the technologies for the nuclear waste transmutation and the fission recycling process in the rapid-process nucleosynthesis.

Chapter 2 describes the n_TOF facility, where the measurement has been performed in 2016. This is a neutron beam facility located at CERN, with excellent characteristic in terms of high energy resolution and instantaneous flux, offering a unique environment to perform accurate neutron induced cross section measurements. The chapter includes a detailed description of the dedicated experimental apparatus, which represents the first example of in-beam fission measurement at n_TOF based on silicon detectors. It consists of a compact stack of six single pad silicon detectors placed along the neutron beam, arranged to measure the reaction products emitted in the forward and in the backward directions from Li, B and the U samples. The adopted configuration allowed to have a very high geometrical efficiency, able to compensate to a large extent any source of systematic uncertainty arising from the angular distribution of the reaction products.

The data analysis is described in Chapter 3. The *Ratio Method* allowed to remove the contribution of all the constant sources of systematic uncertainty, normalizing the ^{235}U cross section to its standard integral, defined between 7.8 eV and 11 eV. Moreover, the use of two independent references has permitted to verify the consistency of both, ensuring the robustness of the final results. The minimization and the careful handling of all the sources of uncertainty represented an important aspect of the measurement. The typical neutron energy uncertainty of n_TOF, ranging between 10^{-3} and 10^{-4}, was achieved using the time-of-flight technique and accurately calibrating the flight path using several resonances of the ^{235}U fission cross section. In addition, the consistency of the experimental ^{235}U(n,f) cross section with the standard values in the energy intervals where they overlaps represented an additional validation for the mea-

surement.

The experiment required an accurate characterization of the experimental apparatus, whose performances has been simulated and optimized using the Geant4 Monte Carlo code. The implementation of the setup and the interaction of the n_TOF beam with the elements in Geant4 followed several validation steps, during which the consistency of all available geometrical and physical quantities were checked, as well as the absence of hidden correlation. The choice to generate directly the reaction products, to overcome the unbearable cost in terms of computing time of neutrons, represented a major breakthrough for the simulations, which required additional verifications. The simulation were used to evaluate the detection efficiency of Li and B detectors as a function of the incident neutron energy and the absorption of neutrons in all the materials placed along the beam. Results are described in the Chapter 4.

The final results are presented in Chapter 5. The n_TOF ^{235}U(n,f) experimental cross section is compared with the major libraries and with the IAEA standard, with particular care for the interval 10 keV to 30 keV. In particular in the range 9 keV to 18 keV an average overestimation of 5% has been found, partially confirming the origin of the inconsistencies that motivated the present measurement. Finally, the ratio between the B and Li yields is shown in comparison with the ratio of the standard values, in order to further validate the experimental results. Moreover, this quantity resulted to be a dataset of interest for the next evaluation of the standard cross sections.

Chapter 1

Nuclear Fission

1.1 Fission process

Nuclear fission is an extremely complex nuclear reaction during which the nucleus passes through a progressive deformation and finally splits in two lighter fragments, with the contemporary release of a significant amount of kinetic energy (hundred of MeV). After the discovery of the neutron by Chadwick [3], Enrico Fermi and his collaborators started a systematic study of the interaction of this new particle with various elements [4]. One of the more studied elements was uranium, the heaviest nucleus present in nature with atomic number 92. Their intention was to produce a heavier element by means of neutron capture reactions and consequent β-decay. These experiments erroneously recognized the β-radioactivity subsequent to the uranium irradiation as a signature of the neutron capture and the production of the heavier element [5]. The real nature of these β-emitters was correctly identified by Hahn, Strassman and Meitner as the unstable fragments produced by the neutron induced uranium fission [6]. This unexpected result was achieved through difficult chemical analysis, that was able to identify the presence of Barium isotopes among the radioactive elements, justified only by the rupture of the uranium nucleus.

Meitner and Frisch were the first to recognize that if the nucleus is divided in two similar fragments, the Coulomb mutual repulsion would

result in a total kinetic energy of ≈ 200 MeV [7]. The hypothesis was later confirmed by the observations of Frisch himself [8]. The first extensive theoretical description of fission was given by Bohr and Wheeler [9] and was based on the Liquid Drop Model proposed by Gamow [10].

1.1.1 Liqid Drop Model

The Liquid Drop Model (LDM) provides a first evaluation of the energetics associated with small nuclear deformation, with very few initial assumptions. In analogy with the semi-empirical formula of Weizsacker [11], the first and dominant term in the mass equation is proportional to the nuclear volume, expressing the fact that the nuclear binding energy is proportional to the number of nucleons. The second term, which has opposite sign, is proportional to the surface area and takes into account the reduction associated with the nucleons close to the surface. This term is small for a sphere while it increases with any deformation of the nucleus. The third term is the Coulomb contribution, describing the repulsive force among the protons. Finally, a fourth term proportional to (N-Z)^2/A represents the symmetry of the nucleus connected with the empirical observation that in the absence of Coulomb forces stable nuclei prefer to have, as far as possible, equal numbers of protons and neutrons.

The LDM considers small nuclear deformations, assuming that the volume of the nucleus itself is conserved, representing the saturation property of the nuclear density. Because of the volume conservation the first term of the mass equation is constant as well. If a small, axially symmetric deformation is considered, the radius can be expressed as:

$$R(\theta) = R_0[1 + \alpha_2 P_2(cos\theta)] \tag{1.1}$$

where R_0 is the radius of the original sphere, $P_2(cos\theta)$ is the Legendre polynomial with θ the angle of the radius vector, and the coefficient α_2 is the magnitude of the quadrupole deformation (here we are not considering higher order multipole deformations since their contribution is much smaller of α_2). The surface and Coulomb energies for such small

deformation are:

$$E_s = E_s^0(1 + \frac{2}{5}\alpha_2^2) \quad E_c = E_c^0(1 - \frac{1}{5}\alpha_2^2) \tag{1.2}$$

Depending on the values of E_s and E_c, the liquid drop may be stable or unstable under the deformation. Therefore, under small deformation the energy change is given by:

$$\Delta E = \Delta E_s + \Delta E_c = \frac{2}{5}\alpha_2^2 E_s^0 - \frac{1}{5}\alpha_2^2 E_c^0 \tag{1.3}$$

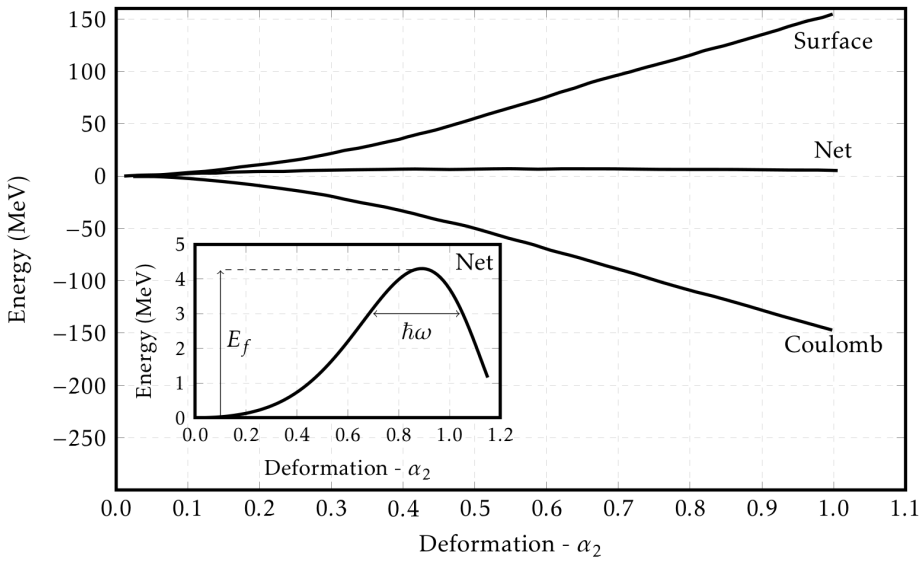

Figure 1.1: Surface and Coulomb contributions to the nucleus total energy as a function of the deformation parameter α_2. The inset reports a zoom of the net value, presenting the characteristic barrier shape (Courtesy of A. Stamatopoulos [12]).

It is interesting to note that the two contributions have usually similar values and nearly cancel each other, as shown in figure 1.1, reporting the variable components of E_s and E_c as function of the deformation parameter α_2. The net value represents the fission barrier shown in the inset, with maximum height of $\approx$ 4 MeV for α_2 $\approx$0.9, while the variable components of the two individual contributions have values around 130 MeV. This

makes evident the need to carefully evaluate the surface and Coulomb energy, in order to obtain accurate deformation energies from the LDM. Defining the fissility parameter as $x = E_c^0/E_s^0$, a drop requires x<1 for being stable. On the contrary for x>1 there is no potential energy barrier to prevent the spontaneous splitting of the drop. A semi-empirical estimation of x as a function of Z and A was provided by Green, who obtained $x = Z^2/(50.13A)$. Typical values for heavy nuclei, such as ^{235}U, are ≈ 0.7, while for Z>125 the LDM predicts the absence of any barrier. In order to properly describe nuclear deformations, formula 1.1 should include higher order Legendre polynomials, thus extended to:

$$R(\theta) = (R_0/\lambda)[1 + \sum_{n=1} \alpha_n P_n(cos\theta)] \tag{1.4}$$

where the parameter λ is only a scale factor, taking into account the conservation of the nuclear volume. Figure 1.2 shows the variation of the nuclear shape with different values of the parameters α_2 and α_4. In the the bottom-right of the map, beyond the scission line, the nucleus is no longer stable and undergoes fission.

Besides the barrier height, other properties are of interest for the fission, in particular the curvature at the saddle point and the total width of the barrier itself, useful for determining the spontaneous fission lifetimes. The LDM has some limitation in describing adequately the full shape of the fission barrier, since the surface of the potential energy beyond the saddle point is difficult to describe. Moreover, many heavy nuclei are well known to have appreciable deformations in their ground state, while the LDM predicts a spherical shape. Finally, most of the experimental data are available for heavy nuclei, with $Z \approx 92$, where single particle effects may change significantly the fission barrier shape. For such nuclei a second minimum in the potential energy is present, resulting in a double barrier that makes the description of its penetration rather more complicated.

1.1.2 Strutinsky Hybrid Model

The need of incorporating the single particle effects given by the nuclear shell structure led Strutinsky to propose the microscopic-macroscopic

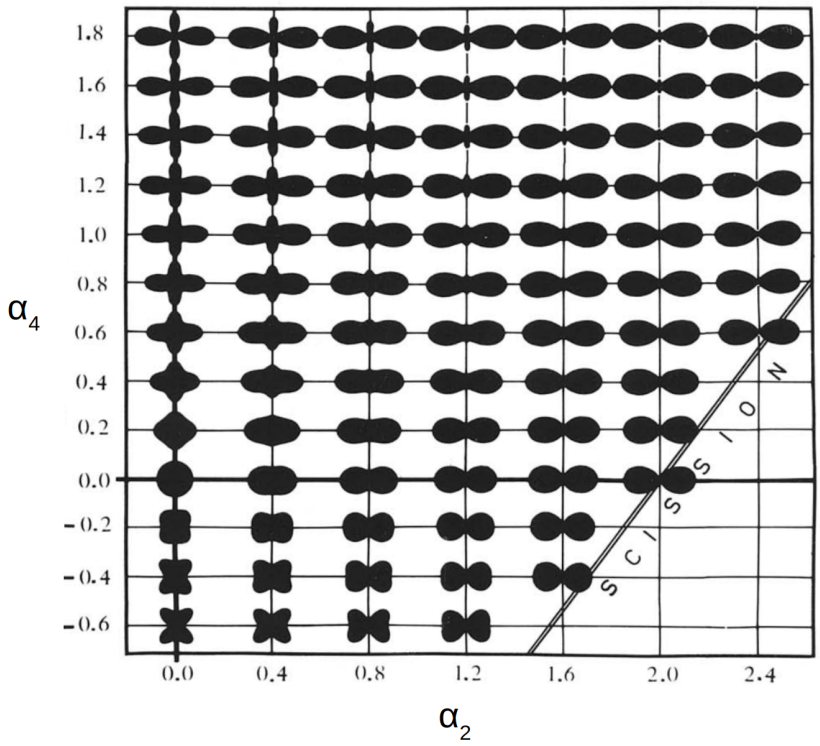

Figure 1.2: Nucleus deformations with different values of α_2 and α_4, the double line indicates the locus of scission (from [13]).

model [14]. In this model the shell effects are considered as a correction to the LDM which contains the dominant contributions, namely the Coulomb and surface terms. Therefore, the total energy should be expanded to include additional terms, corresponding to the pairing energy (δP) and the shell correction (δU), both depending on the nuclear deformation:

$$E_{tot} = E_{LDM} + \delta P + \delta U \tag{1.5}$$

The pairing term expresses the fact that the total energy is lower when the number of protons and neutrons are even, so there is a equal quantity of particles with opposite sign of spin. Thus, the pairing energy is given

by:

$$\delta P(N,Z) = \begin{cases} -\delta_0 & \text{N,Z even} \\ 0 & \text{A odd} \\ +\delta_0 & \text{N,Z odd} \end{cases} \tag{1.6}$$

The shell correction δU is calculated as a difference $\delta U = U - \tilde{U}$, where U is the total energy obtained with a realistic model, having nonuniform energy spacing and level degenerancies, while $\tilde{U}$ is the one obtained with a uniform level distribution. Systematic errors arising from the general problem of calculating the total energy from a single particle model will be compensated, while the effects arising from special degenerancies of the shell model are preserved, thus representing a clear advantage. The correction is negative for spherical nuclei at or near closed shells, representing the fact that they have a lower total energy and a stronger binding, while in the case of mid-shell nuclei the correction is positive. The situation is reversed if a deformation is taken into account, indeed in this case the correction is typically positive for closed shell nuclei and negative for the mid-shell ones. The shell correction thus favors non-spherical shapes for the latters and it is strong enough to dominate the LDM contribution.

The superposition of the shell correction and the pairing term on the LDM to calculate the nuclear energy as a function of deformation produces a double-humped barrier, schematically shown in figure 1.3. As determined experimentally but contrary to the LDM assumptions, it is to be noted that the shell correction creates a local minimum for a non-zero deformation, this indicates the existence of a ground state having a non-spherical equilibrium shape. Moreover a second minimum in the potential barrier is present, corresponding roughly to the LDM saddle point. The excitation levels in the first potential well are indicated as Class-I levels and are typically more dense and narrow, while the ones in the second minima are indicated as Class-II levels and are wider and less dense. An extended description of the double-humped fission barrier has been provided by Bjornholm and Lynn [16].

The introduction of the shell and pairing corrections to the LDM, and the consequent existence of a double-humped barrier, allows one to justify many experimental evidences for which the LDM was inadequate.

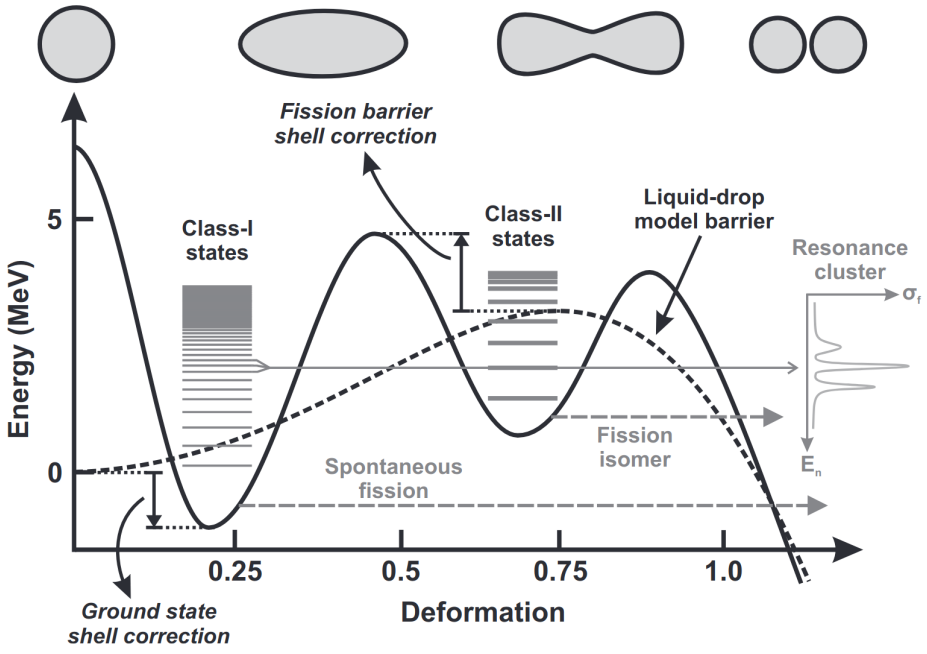

Figure 1.3: Double-humped fission barrier obtained with the pairing and shell corrections (continuous line), compared with the fission barrier obtained with the LDM (dashed line) (Courtesy of A. Tsinganis [15]).

In particular the hybrid model is able to explain the existence of fission isomers, *i.e.* nuclear states that undergo fission with very long half-life if compared to the typical values of the γ-decay half-life. These phenomena can be understood with the existence of the second minimum in the fission barrier, for which the γ-decay to the ground state of the nucleus is much less favored than the fission through the second hump of the barrier. Moreover the existence of the Class-II state justifies the observed "clustering" of fission resonances. Each cluster corresponds to a Class-II state, which has a higher fission width, since it only needs to penetrate a much thinner barrier, while the internal structure is due to the narrower and denser Class-I states. Whenever the nucleus is excited to a Class-I state that is well-matched in energy and spin-parity with a Class-II state, then the fission probability is higher and a resonance is observed in the measured fission cross-section. The spacing between clusters cor-

responds to the spacing of Class-II states, while the spacing within each cluster is characteristic of Class-I states. As an example, figure 1.4 shows the ^{240}Pu(n,f) cross section, in which the clustering effect is very clear.

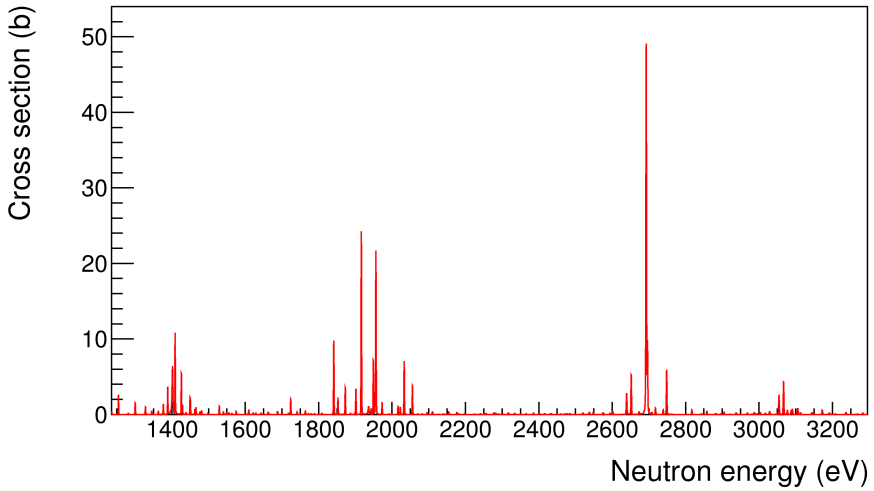

Figure 1.4: Resonance clustering in the ^{240}Pu(n,f) cross section evaluated by ENDF/B-VIII library. The Class-II spacing determines the separation between each cluster, while the separation between resonances belonging to the same cluster corresponds to the Class-I spacing.

1.1.3 Fission cross section

According to the concise description of the fission process presented in the previous sections, the main features of the neutron fission cross sections can be explained. For neutrons of energy smaller than ≈ 0.1 eV, in case of heavy nuclei like ^{235}U, the cross section essentially depends on the time spent by the incident neutron inside the nucleus. Therefore, the cross section results to be inversely proportional to the incident neutron velocity. We can express this with the "1/v law".

$$\sigma \propto \frac{1}{v} \propto \frac{1}{\sqrt{Energy}} \tag{1.7}$$

With increasing neutron energy, the cross section presents a large

amount of resonances, corresponding to the excited states of the compound nucleus. These cross sections presents an high resonance density for heavy nuclei but at the same time are generally narrow and can be resolved experimentally. Figure 1.5 shows the fission cross sections for the two most abundant isotopes of uranium, namely ^{235}U and ^{238}U, evaluated by the library ENDF/B-VIII. In the ^{235}U(n,f) cross section, the resonances are resolved for neutron energy below 2.2 keV, where the boundary of the *Resolved Resonance Region* (RRR) is set. Increasing the energy the resonances cannot be separated any longer, since the spacing is of the same order of magnitude of the widths, giving rise to the so-called *Unresolved Resonance Region* (URR). Initially the grouping of individual resonances gives rise to structures in the cross section which vanish for neutron energy above $\approx$ 10 keV, where the cross section becomes rather smooth.

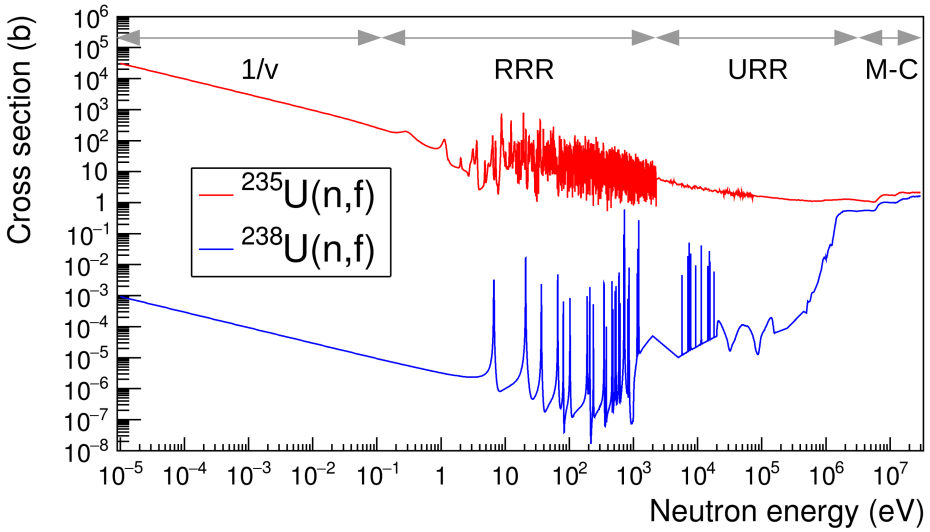

Figure 1.5: Evaluation of the ^{235}U and ^{238}U fission cross sections by ENDF/B-VIII library. The gray arrowed lines indicate the approximate energy intervals corresponding to the "1/v", Resolved Resonance Region, Unresolved Resonance Region and Multi-Chance fission respectively.

It is interesting to note the large difference between the fission cross sections of the two uranium isotopes for neutron energy lower than 1 MeV. This different magnitude is mainly due to the pairing energy de-

scribed in the previous section. Indeed, thanks to the positive contribute of δP, the neutron binding energy for n+^{235}U is higher than the *activation energy*, *i.e.* the difference between the peak of the fission barrier and the ground state. This compound nucleus is therefore unstable against fission, even after the absorption of a very low energy neutron, consequently the ^{235}U(n,f) cross section is very high at thermal energy. In the case of even-even nuclei, such as ^{238}U, the contribute δP has opposite sign, resulting in a compound binding energy lower than the fission activation energy, thus the ^{238}U fission cross section is many orders of magnitude lower than the one of ^{235}U. When the kinetic energy of the incident neutron is enough to compensate the δP contribution, the ^{238}U(n,f) cross section increases significantly, reaching values of the same order of magnitude of the ^{235}U(n,f) cross section. This threshold effect is typically observed for $E_n \approx$1 MeV, *i.e.* typical values of δP for heavy nuclei [17]. Finally in the MeV energy region the fission cross section of both the elements exhibits a series of "steps" which correspond to the *multi-chance fission*. The compound nuclei can undergo fission after the pre-equilibrium emission of one (second-chance fission), two (third-chance fission) or more neutrons (nth-chance fission). This is possible since the typical time-scale of a neutron emission is significantly shorter than the fission one [18].

1.2 Standard neutron cross sections

Neutron standard cross sections referes to a restricted group of very well-known reactions, that are tipically employed to measure neutron fluxes or for measurements of neutron induced reactions where the cross sections is measured relatively to these references. By adopting the thin sample approximation, the cross section of a given reaction is calculated by the following expression:

$$\sigma(E_n) = \frac{R(E_n)}{\phi(E_n)\rho\varepsilon(E_n)} \tag{1.8}$$

where $R(E_n)$ is the reaction rate, $\phi(E_n)$ the incident neutron flux, ρ the sample areal density and $\varepsilon(E_n)$ the detection efficiency. If a reference reaction can be used during the measurement, the knowledge of the neu-

tron flux is not required and the measurement can be considered self-consistent, provided that the reference cross section is well known, or better it is a standard in the energy region of interest. The condition to apply this method is that the samples of the standard reaction and of the reaction to study are exposed to the same neutron flux, apart possible differences due to the interaction of the beam with the components of the experimental setup or size of the samples. The expression 1.8 thus becomes:

$$\sigma_X(E_n) = \frac{R_X(E_n)\rho_{std}\varepsilon_{std}(E_n)}{R_{std}(E_n)\rho_X\varepsilon_X(E_n)}\sigma_{std}(E_n) \tag{1.9}$$

where the suffix $_{std}$ indicates the quantities relative to the standard reaction, the $_X$ the ones relative to the reaction we are measuring and $\sigma_{std}(E_n)$ is the standard cross section employed. This approach eliminates the need of directly measure the neutron flux with dedicated devices, which may complicate the experimental design and possibly introduce additional sources of uncertainty.

Given the key role played by the standard cross sections, the accuracy of their data must be as best as possible, since they limit the accuracy of the measurements that refer to them. The Cross Section Evaluation Working Group (CSEWG) and the International Atomic Energy Agency (IAEA) cooperatively manage the definition of the standard cross sections and the respective neutron energy intervals in which they are considered standard [19]. The first complete evaluation of the neutron standards has been made by Carlson et al. [20] in 2006, that is strictly correlated with the ENDF/B library released in the same year, *i.e.* ENDF/B-VII.0 [21], since the same standard cross section has been accepted. Concerning the 2006 evaluation, a set of 400 experimental data with covariance matrices of uncertainties has been combined to perform R-matrix model fits for the light-elements cross sections and non-model least-squares fits for all the other cross sections. These fits have been calculated using the so-called GMAP code [22, 23] developed by Poenitz, which allows to fit all types of cross section (absolute and shape), their ratios, spectrum-averaged cross sections and thermal constants.

For what said before, it is evident that the evaluation of a neutron standard is a complex process that requires a careful selection of the ex-

perimental datasets and a proper fitting procedure. Hence the complete knowledge of all the uncertainties is essential, with particular care to the hidden systematic errors and to the correlations between the datasets and uncertainties. The neutron standard working group is responsible to keep this database constantly updated with the most recent experimental data.

Table 1.1: Neutron standard cross sections released by CSEWG and IAEA in 2017.

Reaction	**Energy interval**
H(n,n)	1 keV to 20 MeV
^{3}He(n,p)	0.0253 eV to 50 keV
^{6}Li(n,t)	0.0253 eV to 1 MeV
^{10}B(n,α)	0.0253 eV to 1 MeV
^{10}B(n,$\alpha_1\gamma$)	0.0253 eV to 1 MeV
C(n,n)	10 eV to 1.8 MeV
Au(n,γ)	0.0253 eV, 0.2 to 2.5 MeV, 30 keV MACS
^{235}U(n,f)	0.0253 eV, 7.8-11 eV, 0.15 MeV to 200 MeV
^{238}U(n,f)	2 MeV to 200 MeV

In order to be used as a reference, a neutron reaction must have specific characteristics, among the more important are: a smooth energy dependence in the standard energy interval, negligible competitive reactions and a relatively simple production and management of targets with low contaminants. The standard cross sections released in 2017 are reported in table 1.1, with the related neutron energy intervals. To point out that the point-wise cross section value for thermal neutrons, namely having energy 0.0253 eV, is defined as a standard for two reaction, *i.e.* Au(n,γ) and ^{235}U(n,f). For ^{235}U(n,f) the integral of the cross section between 7.8 eV and 11 eV is as well defined standard quantity, resulting very conve-

nient during the normalization of experimental data, since the interval contains a large resonance and the borders are located in two minimum, thus removing any significant border effect. Finally the *Maxwellian Averaged Cross Section* (MACS) of ^{197}Au(n,γ) at T = 30 keV, *i.e.* the convolution of the reaction cross section with a Maxwellian neutron energy distribution at a temperature T, is also defined as a standard.

In addition to the definition of the standard neutron cross sections, the working group handles different additional quantities, useful to be employed as references. In particular they provide fission reference cross sections up to 1GeV (table 1.2), the reference cross sections for prompt gamma-ray production (table 1.3) and the prompt fission neutron spectra for the ^{235}U(n,f) reaction induced by thermal neutrons and for ^{252}Cf spontaneous fission (table 1.4). In particular the so-called *reference cross sections* play the same role of standard cross sections, hence having the same proprieties such as a smooth cross section as a function of energy, but they are not as well known.

Table 1.2: Neutron reference cross sections released by CSEWG and IAEA in 2017.

Reaction	**Neutron energy interval**
^{nat}Pb(n,f)	$\approx$ 20 up to 1 GeV
^{209}Bi(n,f)	$\approx$ 20 up to 1 GeV
^{235}U(n,f)	200 MeV to 1 GeV
^{238}U(n,f)	200 MeV to 1 GeV
^{239}Pu(n,f)	200 MeV to 1 GeV

Among the standard cross sections the ^{235}U(n,f) plays a relevant role since it is one of the two that may be employed until 200 MeV, together with the fission of ^{238}U which, however, has a fission threshold of $\approx$ 1 MeV [17]. The ^{235}U fission can be used as a standard seamless from 150 keV to 200 MeV. Below 150 keV the ^{235}U(n,f) cross section is not defined as a standard, but it is currently used as reference, in particular to measure

Table 1.3: Prompt γ-ray production reference cross sections released by CSEWG and IAEA in 2017.

Reaction	**Neutron energy interval**
^{10}B(n,$\alpha_1\gamma$)	0.0253 eV to 1 MeV
^{7}Li(n,n'γ)	0.8 MeV to 8 MeV
^{48}Ti(n,n'γ)	3 MeV to 16 MeV

Table 1.4: Prompt fission neutron spectra generated with ^{252}Cf spontaneous fission or ^{235}U fission induced by thermal neutrons, released by CSEWG and IAEA in 2017.

Reaction	**Outgoing neutron energy**
^{235}U(n$_{th}$,f)	0.00001 eV - 30 MeV
^{252}Cf(sf)	0.00001 eV - 30 MeV

the cross sections of neutron induced reactions of actinides (see as examples [24, 25, 26, 27]). Its accurate knowledge preferably within $\approx$ 1% is therefore needed and can have important implications in strategic technological applications, as the new generation of future critical or subcritical reactors.

1.3 Application fields of fission

1.3.1 Nuclear energy and waste transmutation

Nuclear power represents one of the main sources of electric power worldwide, accounting for around $\approx$ 10% of total power production in 2018 according to IAEA [28]. Nuclear energy has considerable advantages in terms of economic sustainability and practically zero emission of greenhouse gases, however the public concerns, in particular regarding the ra-

dioactive waste disposal, dominate the debate about nuclear energy and limit its growth. Recently, the possibility of handling the nuclear waste to reduce its radiotoxicity, the so-called Partitioning and Transmutation (P&T), is being revisited in order to find innovative solutions and new options to be applied for the fuel cycle. The primary objective of P&T is to reduce the long-term hazard of the exhausted fuel by transforming the long-lived radionuclides, in particular the transuranic elements (TRUs), into short-lived or inactive elements. Indeed the radiotoxicity of the exhausted fuel is dominated by the $^{241}\mathrm{Pu} \longrightarrow {}^{241}\mathrm{Am} \longrightarrow {}^{237}\mathrm{Np}$ chain and therefore to effectively reduce the hazard the TRUs must be transmuted through fission [29, 30]. The fissioning of actinides is best achieved in fast neutron spectrum systems as Fast Reactors (FRs) or Accelerator-Driven Systems (ADS), where the fraction of fission events relative to radiative capture is higher, thanks to a larger excess of neutrons. Consequently the production of minor actinides is smaller and hence also the long-term radiotoxicity. The P&T strategy requires a complex framework which includes the reprocessing plants, facilities where the TRUs fuel is produced and the development of new reactors dedicated to the waste transmutation.

At present the "Once Through Fuel Cycle" is the most common strategy adopted worldwide in the light water reactors (LWRs), while the "Reprocessing Fuel Cycle" (RFC) results to be more complex and economically less convenient. However, the RFC can be a solution to the growing uranium price in a long-term scenario. Currently the standard strategy consists in the vitrification of High-Level Liquid Waste (HLLW), in order to recycle the major actinides, namely uranium and plutonium, around 99.9% of which can be extracted, preventing their storage in the geological repository. The fuel containing relevant quantities of plutonium, indicated as mixed-oxide (MOX), is then used in special authorized plants. During the LWR-MOX cycle $\approx 25\%$ of plutonium is burned, while $\approx 10\%$ is transformed into long-term minor actinides. The resulting balance is clearly convenient but the LWR-MOX cycle is not a definitive solution to eliminate the radiotoxicity of the radioactive waste. On the contrary, the combination of LWR-MOX and Fast Reactors can significantly increase the utilization rates of actinides. Indeed the characteristics of FRs, in particular their hard neutron spectra, enhance the resource utilization

through breeding and minor actinides burning, while at the same time the higher actinides generation through captures is suppressed compared to LWR.

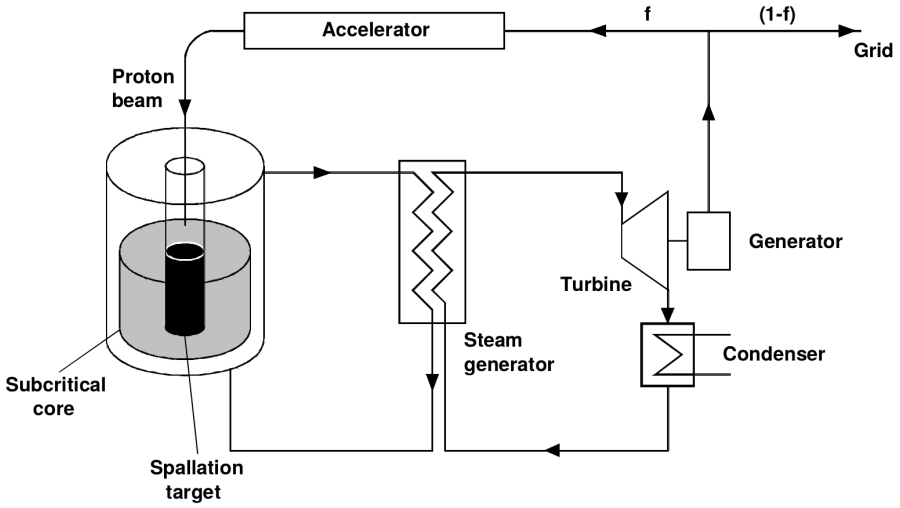

Figure 1.6: Basic concept of an ADS reactor, the fraction of the produced energy **f** is used to power the accelerator, while the remaining **1-f** represents the net energy produced.

An alternative transmutation system is represented by the Accelerator-driven Systems [31, 32]. The basic idea of ADS is to couple a powerful linear proton accelerator ($\approx$ 1 GeV, >10 mA current intensity) with a sub-critical core containing the fissionable material. figure 1.6 shows the sketch of the ADS concept, where is evident that the accelerator is powered by the reactor itself, thus ensuring an intrinsic safety. The proton beam impacts on a lead-bismuth target, where the neutrons are produced through a spallation process (more details in section 2.1). These neutrons are able to sustain the chain reactions in the sub-critical core which surrounds the spallation target itself. The "efficiency" of a reactor powered by an accelerator is significantly lower than the present LWR, since the majority of energy released by a fission event ($\approx$ 200 MeV) is employed to accelerate the protons, with a net energy gain $\approx$ 20 MeV for fission event. The lower efficiency is compensated by the transmutation capabilities of these reactors and by the improved safety, consequence of the subcritical-

ity condition and of the possibility to control the reactor dynamic acting on the proton beam current. Nevertheless many technological issues have to be addressed before the ADS can be considered for commercial use, in particular concerning the proton accelerator performances, the characteristic of the spallation target and the structural materials.

In this context nuclear data play a fundamental role to improve the physics models, by reducing the uncertainties and thus optimizing the design of the core, the radiation shielding, the safety and everything is involved in the design of this new generation reactors. Nowadays, high precision neutron cross section data are available mainly for uranium and plutonium isotopes, in the energy range from thermal to several MeV, reflecting the global interest in fast neutron reactors. Although the current existing nuclear databases are sufficient for a first evaluation of dedicated transmutation ADS and critical reactors, a detailed assessment requires more precise and complete basic nuclear data. In particular the lack of accurate data for minor actinides and high mass plutonium isotopes need to be overcome with new dedicated measurements. The use of innovative coolants, as liquid lead and bismuth, requires to know their neutron cross section and that of all the contaminants with sufficient accuracy. Finally, the transmutation process needs accurate cross section data from 1 keV to several MeV for the fission fragments, as well as all the structural materials employed in the transmutations devices , in particular for those concerning the capture cross sections. For most of these measurements the ^{235}U(n,f) reaction is used as reference reaction, so that the accurate knowledge of its cross section in the energy range of interest plays a fundamental role to guarantee high precision data from the measured reactions.

1.3.2 Fission recycling in r-process

The production of the elements found in nature is assigned to a variety of nuclear processes, each one being characterized by a specific environment. The origin of the lighter elements (Hydrogen, Helium and Lithium) during the so-called Big Bang Nucleosynthesis (BBN) is well ascertained [33, 34], although remaining problems in understanding the abundance of primordial ^{7}Li. An additional source of light elements is

given by the interaction of energetic nuclei of galactic cosmic rays (CGR) with the nuclei of the interstellar medium (ISM)[35], whose contribute is relevant for Li, Be and B production. All the other elements are produced in the stars, during the different phases of their evolution. In particular the fusion reactions, occurring in the stellar core, are responsible of producing all the elements up to the iron peak, hence having Z lower than ≈ 26. Even though explosive staged of massive stars can synthesize few elements beyond iron [36, 37], it is well-established since the '50 that the production of heavier elements is mostly assigned to neutron-induced reactions [38, 39].

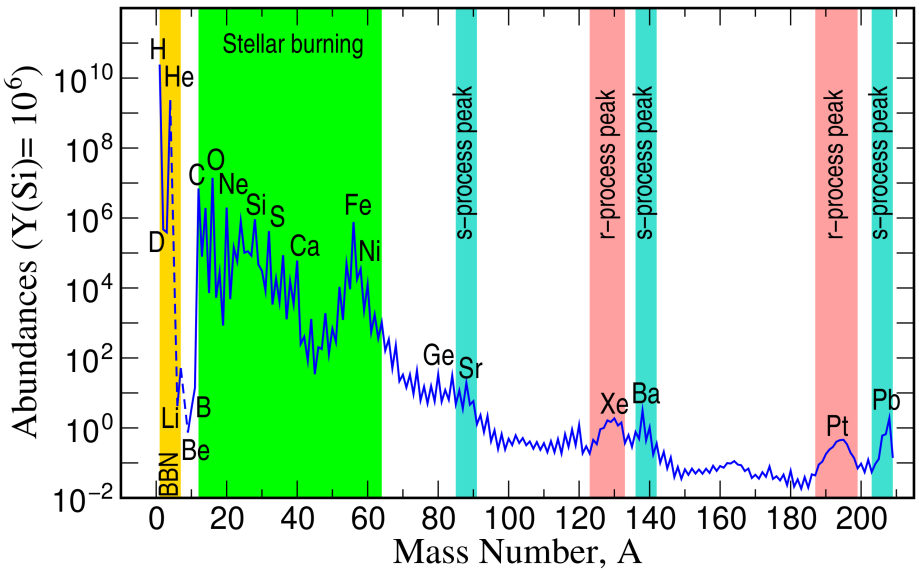

Figure 1.7: Abundances of elements in the solar system as a function of mass number (from [40]). The abundances are scaled so $Y_{Si} = 10^6$ for historical reasons.

The main processes involving neutron captures are the slow (s)-process and the rapid (r)-process, named after the respective timescales of the reactions. The s-process is characterized by long time scales, from 50 Myr to 150 Myr, during which the time between two successive neutron captures is usually longer than the mean life time of the isotopes produced by the neutron capture sequence. If unstable the compound nucleus β-decay

and, as a consequence, the nuclei involved in the s-process are all stables, or close to the stability valley. Many reactions of the s-process have been measured in last decades and the respective experimental data are available [41, 42]. This s-process takes place in the so-called ^{13}C pocket [43], which is formed in the outer layers of low-mass AGB stars during their burning phase. This process is mainly powered by the ^{13}C(α,n)^{16}O reaction and it is characterized by a relatively low neutron density (10^8 n/cm^3). On the other hand, the r-process takes place in explosive scenarios, where very high neutron densities (10^{30-35} n/cm^3) are available for rapid sequences of neutron capture reactions, which operate over a timescale of few seconds and quickly produce isotopes close to the neutron drip line and far from stability. Only afterwards these very-unstable isotopes decays toward the valley of stability through a succession of beta decays. Contrary to the s-process, only a few of experimental data are available for the neutron capture reactions of the isotopes involved in the r-process, because of the difficulty to manage the radioactive samples to be measured and because the available neutron fluxes in the neutron beam facilities were not high enough to study most of the reactions related to such a kind of process.

The quest for the r-process environment generated a large number of speculations in the last decades [44, 45]. A possible scenario is the merger of neutron stars (NS) (or black hole and neutron star) [46, 47], but include also rare classes of supernovae [48, 49] as well as hypernovae/collapsars with polar jet ejecta [50, 51] and possibly also accretion disk outflows related to the collapse of fast rotating massive stars [52, 53]. Figure 1.7 shows the typical pattern of the solar system element abundances, with colored areas highlighting the characteristic structures of the main processes. The production of heavy elements (A>60) is determined in large part by the s- and r-processes which produce characteristic peaks, highlighted by the blue and red areas respectively. The r-process peaks are typically located where the value of the neutron separation energy are smaller, while the bottlenecks of the s-process arises from very small neutron capture cross sections.

Neutron induced fission reactions play an important role in the r-process, in particular within the NS-NS merger scenario. Fission determines the region of the nuclear chart where the neutron captures and

beta-decays stop [54, 55]. Moreover, depending on the dynamic conditions, FFs can serve as seed for neutron capture rapid sequences toward the production of other fissionable elements, giving rise to several fission cycles, before all neutrons are used [56], this process is referred to as *fission recycling*. Fission has been suggested to be responsible for the production of a robust r-process pattern, in particular in the case of medium mass nuclei (with A<140) whose abundances are partially determined by the fission yields of very heavy nuclei (with A>280). Figure 1.8 shows the comparison between the r-process solar system abundances and the final abundances calculated with SKYNET [57], with and without the inclusion of fission recycling process, assuming a reasonable electronic fraction Y_e = 0.1. The agreement when the fission is included (blue line) is far better, in particular in the medium mass elements (grey area, corresponding to the lanthanides), where the fission contribute is more relevant.

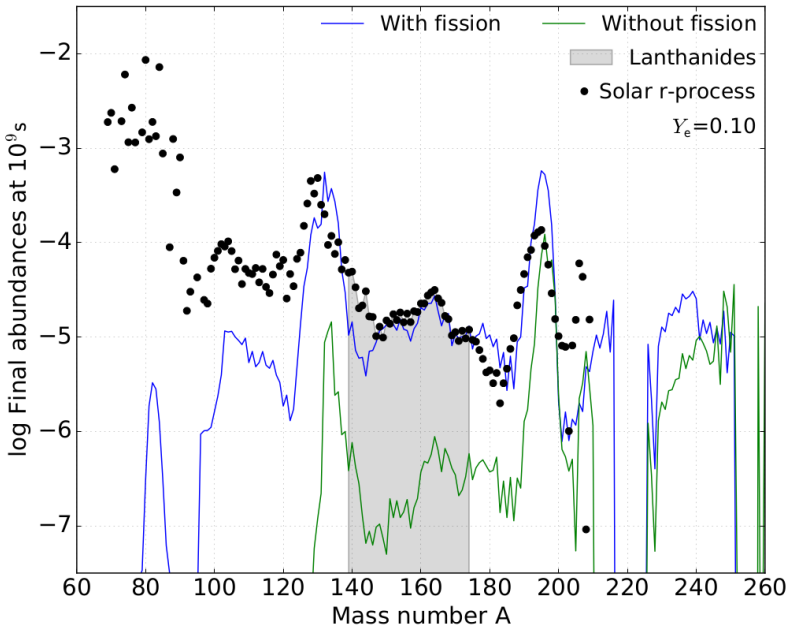

Figure 1.8: r-process abundances in the solar system (solid symbols) are compared to SKYNET calculations with and without fission recycling (from [58]).

The lack of direct nuclear experimental data makes the description of the fission recycling during the r-process extremely challenging, since it strongly depends on the correct modeling of many neutron rich nuclei, in particular of their fission barrier. Due to the dominance of neutron-induced fission, the fission barrier itself is the most important quantity for the determination of reliable fission rates, since the fission process occurs at energies just above the fission barrier. In addition to the description of the different fission reaction channels and the corresponding fission yields [59, 60], it is fundamental to determine the resulting abundances [61]. Finally, during the last phase of the r-process, α-decay competes with the fission, determining the final abundances of Lead, Thorium, Uranium and long-lived actinides. The correct description of transuranic nuclei is necessary to determine the r-process abundances obtained in NS merger, with important consequences for the kilonova lightcurves [62].

1.4 ^{235}U fission as reference

The most recent accurate measurement of n_TOF neutron flux has been performed in 2011, during the so-called Phase-2, and published in 2013 [1]. In order to achieve the required high-accuracy, ranging between 1% and 5% according to the neutron energy interval, four different detection systems based on three different neutron standard reactions have been used for the neutron flux measurement. The Silicon Monitor [63] (SiMon) and the MicroMegas [64, 65] (MGAS(^{10}B)) covered the energy range between thermal and 100 keV, using respectively the standard reactions ^{6}Li(n,t) and ^{10}B(n,α) as converters. At higher energies the experimental setup relied on the ^{235}U(n,f) reaction and three different detectors: MGAS(^{235}U), a calibrated fission chamber from Physikalisch Technische Bundesanstalt [66] (PTB) and a Parallel Plate Avalanche Counters [67, 68] (PPAC). In particular the MGAS(^{235}U) covered the range from 100 keV to 1 MeV, the PTB chamber from 100 keV to 10 MeV and the PPAC was suitable from 10 MeV to 1 GeV. Finally the experimental results were compared with the outcome of the Monte Carlo simulations, made with FLUKA and MCNP.

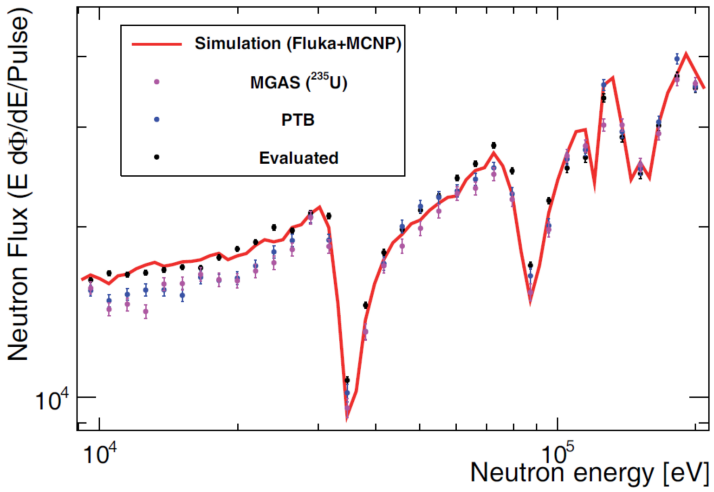

Figure 1.9: n_TOF neutron flux measured in 2001. The combination of SiMon and MGAS(^{10}B) evaluated flux (black points), agrees with the Monte Carlo simulations (red line), while the detectors using ^{235}U fission as reference (blue and purple points) highlights a discrepancy between 10 and 30 keV.

Comparing the flux measured by the different detectors between 10 and 30 keV a relevant discrepancy was observed. The detectors using the ^{235}U(n,f) reaction, hence MGAS(^{235}U) and PTB, agreed with each other but the measured flux were lower by $\approx$ 6-8%, relative to the flux measured by SiMon or MGAS(^{10}B). The observed discrepancy is shown in figure 1.9, where the flux measured using the MGAS(^{235}U) and PTB (purple and blue points respectively) is compared with the combination of SiMon and MGAS(^{10}B) evaluated flux and with the flux predicted by the two Monte Carlo simulations. A possible reason that can justify this discrepancy is that the used ^{235}U(n,f) cross section is overestimated by several percent in that neutron energy region. In this energy interval, most evaluations assign an uncertainty of $\approx$ 1% to the ^{235}U(n,f) cross section, much lower than the observed discrepancy.

An additional evidence of a possible overestimation of the ^{235}U(n,f) cross section in the energy range between 10 keV and 30 keV, emerges considering the ^{235}U(n,γ) cross section measurement published by Jandel

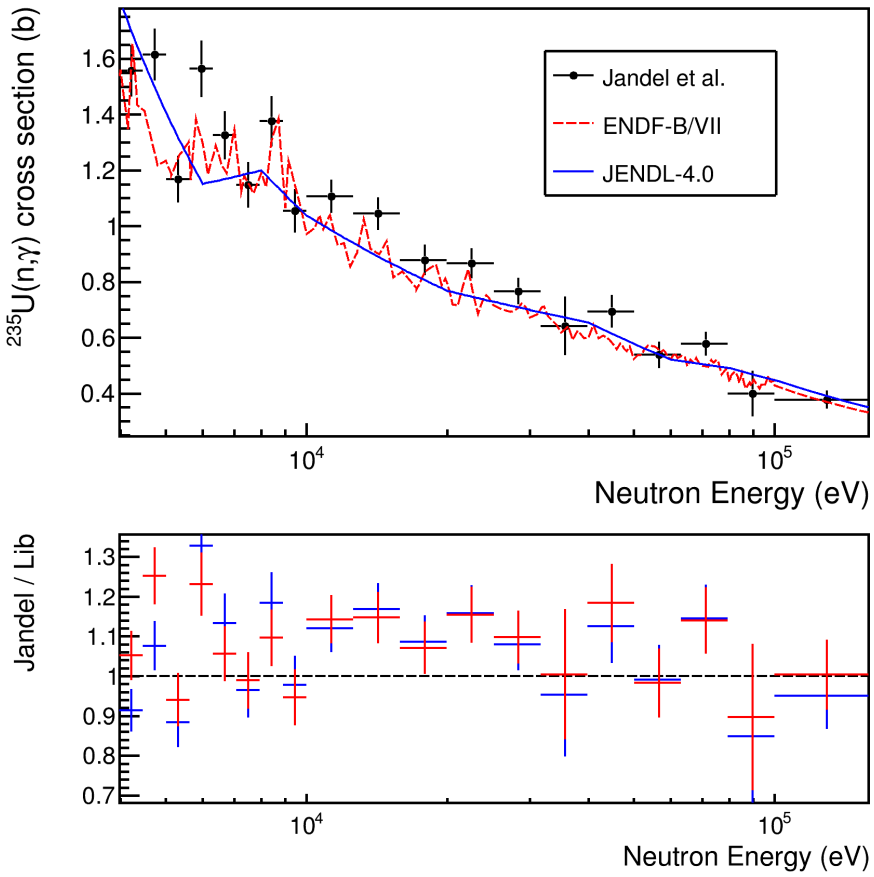

Figure 1.10: Comparison and ratio of ^{235}U(n,γ) cross section measured by Jandel et al. [2], using the ^{235}U(n,f) as reference, respect to the ENDF/B-VII (red) and JENDL-4.0 (blue) libraries.

et al. in 2012 [2]. The top panel of figure 1.10 shows the experimental ^{235}U capture cross section, compared with two major libraries, available when the measurement was performed, namely ENDF/B-VII [21] and JENDL-4.0 [69]. The ratio between the experimental data and the two libraries is reported in the bottom panel of the same figure. In the energy interval from 10 keV to 30 keV the libraries reveal a difference of $\approx$ 10% respect to the Jandel data. Since the capture cross section is extracted relative to the evaluated ^{235}U(n,f) cross section, the observed discrepancy can be

justified even here by an overestimation of the fission cross section.

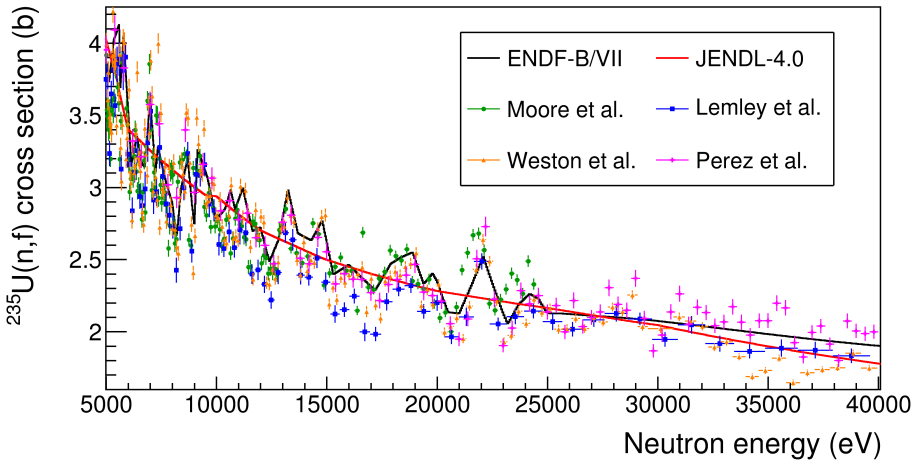

Figure 1.11: Comparison of high resolution experimental ^{235}U fission cross section with the ones provided by ENDF/B-VII and JENDL-4.0 libraries.

1.5 Nuclear data status of ^{235}U(n,f)

Being one of the most studied reactions, many experimental dataset of the ^{235}U(n,f) cross section are available in the experimental repository like EXFOR [70] (Experimental Nuclear Reaction Data). To further investigate over the 10-30 keV discrepancy, the comparison between some suitable EXFOR datased and the cross section evaluated by major libraries is reported below. It is interesting to remark that most of these datasets date back to the 70s and 80s. In particular the cross section measured by Moore et al. [71], Lemley et al. [72], Wagemans et al. [73] and Perez et al. [74] have been considered for our purposes.

Figure 1.11 shows the comparison of the ^{235}U(n,f) cross section evaluated by the ENDF/B-VII and JENDL-4.0 (black and red lines respectively), that where available when the present measurement has been proposed, and different experimental measurements in the energy interval

between 5 and 40 keV. At first glimpse one can notice that the black curve (ENDF/B-VII) better describes the structures present in all the considered dataset, while the red curve (JENDL-4.0) presents a smoother behaviour which in any case does not significantly differ from ENDF/B-VII. All the experimental data clearly underestimate the evaluated cross sections in the energy range between 10 and 30 keV, whilst a good agreement is observed outside of this interval. The presence of a systematic deviation in the 10-30 keV energy range can be better observed considering the ratio between each of the four experimental cross sections and the two evaluations, as shown in figure 1.12. Given the similarities between the two evaluations, each couple of ratios shows a very similar behaviour, so that the following statements are valid for both. In the case of the cross section measured by Moore et al. an average deviation of $\approx$ 7-8% is observed, however it is limited to a narrower interval, *i.e.* between 8 and 15 keV. The data by Lemley et al. shows an ratio around $\approx$ 0.9 between 10 and 23 keV, and a smaller deviation ($\approx$ 5%) between 23 and 28 keV. Finally the Weston and Perez cross sections presents a similar behaviour, with a deviation of $\approx$ 5% in the neutron energy interval from 10 keV to 25 keV.

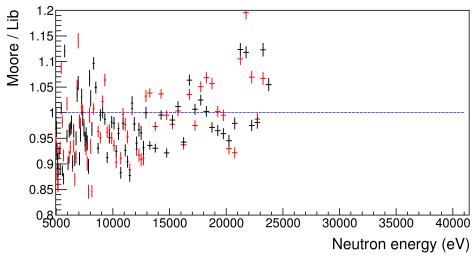

(a) Moore et al.

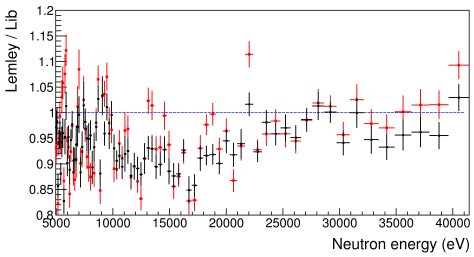

(b) Lemley et al.

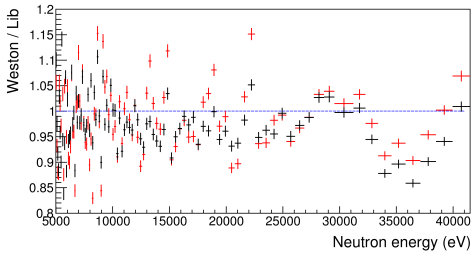

(c) Weston et al.

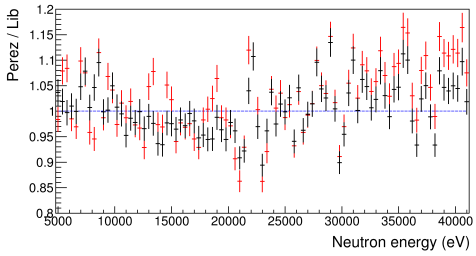

(d) Perez et al.

Figure 1.12: Ratio between different dataset of experimental ^{235}U(n,f) cross section available in EXFOR and the evaluations of ENDF/B-VII (black points) and JENDL-4.0 (red points).

Chapter 2

Experimental setup

Nowadays accurate cross section data of neutron induced nuclear reactions are needed in several scientific and technological fields. This motivated the construction of different facilities worldwide, dedicated to perform accurate cross section measurements, exploiting the time-of-flight technique to measure the neutron energy. Between these facilities n_TOF presents peculiar characteristics, in terms of high energy resolution and high instantaneous flux, allowing to perform the required high quality measurements. The n_TOF facility is based on an idea proposed by Rubbia [75] in late 90s. The first experimental area has been commissioned in 2001 and since then a significant number of accurate neutron cross section measurement has been performed. Even though it was originally proposed to study reactions of interest for applications in nuclear energy production, in particular for the design of present and new generation nuclear reactors and for nuclear waste transmutation, recently the fields of interest increased significantly.

Above all to study the processes of nucleosynthesis induced by neutrons in the framework of the s-process. Furthermore the building of a second experimental area, started in 2013, with a different flight path length and hence higher neutron flux, offered the possibility to perform new measurements, never investigated reactions at n_TOF, concerning for instance the Big Bang Nucleosynthesis (BBN), during which highly active samples have been used.

2.1 n_TOF facility

The n_TOF (neutron time of flight) facility is part of the CERN Accelerator Complex. The neutron beam is produced by means of spallation reactions of high energy protons hitting a lead target. These protons are initially accelerated by the Linac 2 and then injected in the Proton Syncrotron booster, that boosts their momentum to 1.4 GeV/c and then injected in the Proton Syncrotron (PS) where they reach a momentum of 20 GeV/c. The accelerated protons are delivered in bunches, distributed in real time to several experimental halls. The spallation reactions produce a huge number of neutrons ($\approx$ 200 neutrons for each proton) which are suitably moderated in order to give rise to a white energy spectrum. These neutrons, with energy ranging from thermal to a few GeV, are transported through two different beam lines to reach two experimental areas, after a flight path of 180 m and 20 m respectively. These different lengths provide peculiar characteristics of instantaneous flux and neutron energy resolution. The time-of-flight technique is used to measure the energy of the neutrons interacting with the sample under study, with a resolution as small as to 10^{-4} for the farther experimental area and 10^{-3} for the closer one.

In figure 2.1 a sketch of the facility is shown: the proton beam travels underground from the bottom-right of the picture finally impinging on the spallation target. The produced neutrons travel to the experimental areas along two beam lines, made of stainless steel, placed horizontally at an angle of 10° and vertically at 90° with respect to the proton beam direction. The first (Experimental Area 1, EAR1) and the second (Experimental Area 2, EAR2), commissioned in 2014, are placed at the end of the two beam lines respectively. Thanks to the shorter flight path, EAR2 is well optimized to perform measurements requiring high instantaneous flux, such as those involving very low cross sections or radioactive samples with relatively short half life and high activity.

The proton bunches dedicated to n_TOF are characterized by a time width of 7 ns (RMS) and a maximum repetition rate of 1.2 sec. The bunches duration determines the limit of time-of-flight resolution that can be achieved, which in turn determines the energy resolution of the neutrons as a function of their kinetic energy. n_TOF can operate in two

configurations:

- **Dedicated mode:** PS protons are accelerated specifically for n_TOF, each bunch contains around $7{\cdot}10^{12}$ particles.
- **Parasitic mode:** PS protons are primarily accelerated for another experimental area (East Hall) but a fraction of the bunch goes to n_TOF target. In this case the number of protons is smaller ($\approx 3.5{\cdot}10^{12}$).

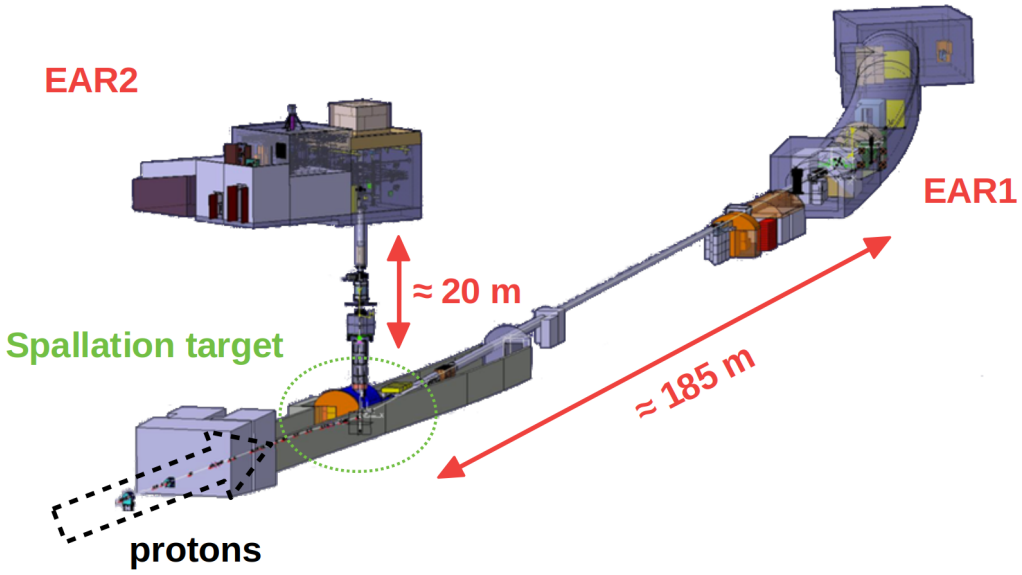

Figure 2.1: Sketch of n_TOF facility, EAR1 is located 185 m downstream respect to the spallation target whilst EAR2 is in 20 m the vertical direction. The black dashed arrow indicates the direction of the incoming proton beam.

n_TOF is characterized by a minimum repetition rate of 0.8 Hz, hence a bunch every $\approx$ 1.2 seconds hits on the spallation target. In principle, in a time-of-flight facility the overlapping of two consecutive neutron bunches may lead to misidentify very low energy neutrons of the i-th bunch as high energy neutrons of the i+1-th bunch. Thus slow neutrons from the previous bunch may represent a background for the current one. This

source of background at n_TOF is not present since the rather slow repetition rate prevents such an overlap, indeed the time-of-flight of thermal neutrons for EAR1 (its flight path 185 meters) is of the order of $\approx$ 100 ms.

As said, the neutrons are produced by spallation reactions, which term refers to a nuclear reaction between a highly energetic light particle and an atomic nucleus, during which many nucleus fragments and other high energy particles are emitted, leaving the residual very different from the initial one. Even though the incident particle can be a light ion or a neutron, usually it is a proton, since this reaction is closely associated with the Accelerator-Driven Systems reactors. The first description of the spallation process has been made by R. Serber [76] in 1947, despite he never uses "spallation" in this paper, while an updated review can be found in [77].

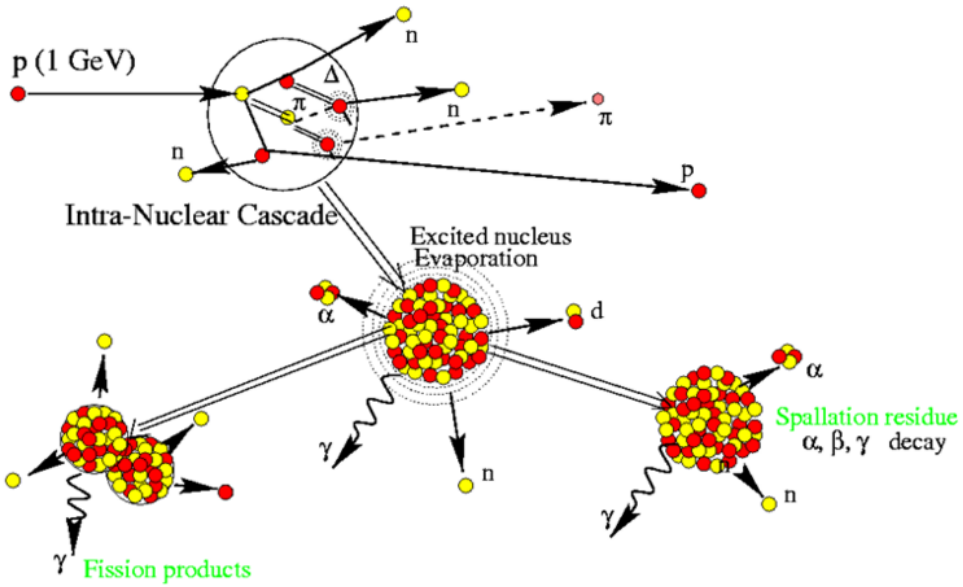

Figure 2.2: Scheme of the spallation process: the high energy proton starts the Intranuclear Cascade, leaving the nucleus in an excited state. This excitation energy is then released through a fission process or light particles emission.

The spallation consists of a set of successive and/or competing nuclear

processes and could be described in a first approximation considering two subsequent stages. In the first stage the initial particle has a kinetic energy typically larger than 100·A MeV and a consequent mean free path of the same order of nucleus size, hence the interactions with the nucleons are like free particles and the process can be represented as a series of binary collisions. During this so called "Intranuclear Cascade" a large number of particles are generated within the nucleus, mainly protons, neutrons and pions. The latter may escape as secondary particles or interact with the nucleus itself, leaving it in an excited state. This stage has a typical time scale of 10^{-22} seconds and the modeling is generally handled with an Intranuclear Cascade code like INCL4[78]. After the cascade process nuclei are generally left in an excited state, therefore they decay to their ground state with a relatively slow de-excitation stage (typical time scale of 10^{-16} s), mostly by nuclear evaporation and fission. The particles emitted during this stage, mainly neutrons but also light charged particles, have an energy between a few MeV and 20 MeV. The low-energy neutrons produced during nuclear de-excitation can be further moderated, reducing their energies to lower values down to the thermal energy. Before the de-excitation takes place, a pre-compound stage occurs which includes the pre-equilibrium emission, multi-fragmentation [79, 80, 81] and the Fermi break-up processes [82].

One peculiarity of such a kind of neutron facilities based on spallation is the presence of the so-called γ-flash, a huge prompt pulse produced by the interaction of the proton beam with the spallation target. Reaching the experimental areas, this γ-flash blinds the detectors for a time interval depending on their properties, that can range from several tens of nanoseconds to a few microseconds, thus significantly limiting the maximum energy limit of the detectors themselves. Nevertheless the γ-flash is usually exploited as initial trigger, in order to have an accurate time reference to measure the time-of-flight of the neutrons. Of course, in order to make the detectors as sensitive as possible to the faster neutrons, several efforts have to be made to shorten the recovery time by acting on the detectors and their read-out electronics.

The amount of neutrons and their energy distribution are strongly dependent on the design and materials of the spallation target. The first target had to be replaced after the first four years of operation (n_TOF-

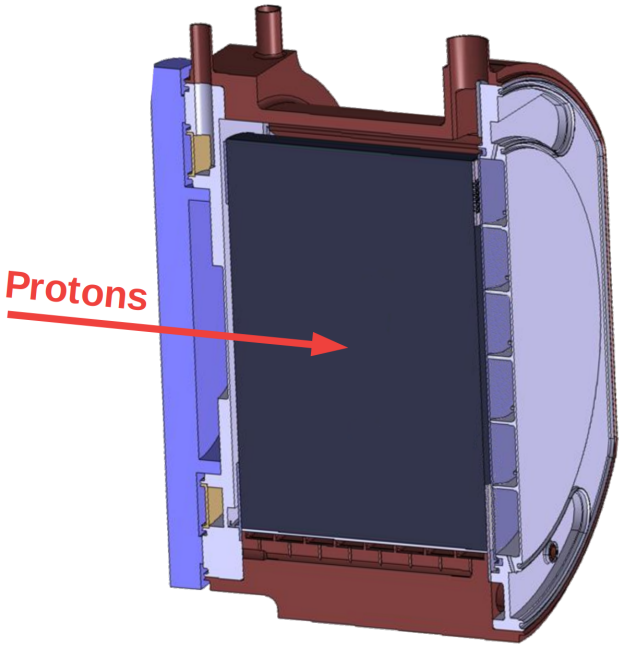

Figure 2.3: Scheme of the spallation target, the PS protons are injected according to the red arrow.

Phase1), because of some degradation caused by insufficient cooling. It has been replaced in 2008, when a new spallation target was installed together with a new cooling/moderator assembly, after having investigated several options to improve the performances and the safety conditions. After its commissioning, a new experimental campaign was started in the following year (n_TOF-Phase2) [83]. This new target was a cylindrical high purity (99.99%) lead block of 60 cm diameter and 40 cm length. A sketch is reported in figure 2.3. The lead core is enclosed in a aluminum alloy vessel, 1 cm thick, that includes the cooling circuit based on the circulation of pressurized demineralized water. A second circuit is placed in front of the neutron exit window toward EAR1. It consists of a 4 cm liquid layer which acts as moderator and is independent of the cooling circuit, making possible to fill it with a different liquid and thus affecting the neutron energy spectrum as a consequence. Initially the moderator consisted of demineralized water, in 2011, during the n_TOF-Phase2, the modera-

tor has been filled with borated water, namely containing a 1.28% of boric acid (H_3BO_3) enriched in ^{10}B, diluted in water. The huge cross section of $^{10}B(n,\alpha)$ reaction at low neutron energy shapes the outcoming flux, reducing the component at energy below 100 eV. Moreover, the reduction of the thermal component decreases the γ background. Indeed the emission of 2.2 MeV γ-rays from the radiative neutron capture on hydrogen is considerably suppressed. The second spallation target operated without any issue during the n_TOF-Phase2 (2008-2013) and n_TOF-Phase3 (2014-2018), completing its planned life span. From 2018 to 2021, profiting by the CERN long shutdown, a new spallation target was developed which is currently being installed [84]. The new target is expected to slightly increase the EAR2 neutron flux and at same time significantly improve the energy resolution, by adding an exit window on the vertical direction and a dedicated moderator circuit, without affecting the working condition in EAR1.

Table 2.1: Overview of n_TOF operative phases, with the corresponding configuration of the spallation target and moderator material.

Phase name	**Year**	**Note**
n_TOF-Phase1	2001-2004	First target configuration
n_TOF-Phase2	2009-2011	Second target configuration & demineralized water as moderator
n_TOF-Phase2	2011-2012	Second target configuration & borated water as moderator
n_TOF-Phase3	2014-2018	Same configuration, EAR2 has been constructed
n_TOF-Phase4	2021-...	Third target configuration

2.1.1 Time of Flight technique

The kinetic energy of the neutrons arriving in the experimental areas is calculated by measuring the time-of-flight, defined as the difference between the time t_n when the neutron is detected in the experimental area and the time t_0 in which it has been produced. The neutron energy is calculated with the relativistic formula:

$$E_n = m_n c(\gamma - 1), \gamma = (1 - v^2/c^2)^{-1/2}, v = \frac{L}{TOF} \tag{2.1}$$

where m_n is the neutron mass, c is the speed of light, L is the flight path and TOF is the measured time of flight. Of course for low energy neutrons the expression 2.1 can be approximated by the classical relationship:

$$E_n = \frac{1}{2} m_n \left(\frac{L}{TOF} \right)^2. \tag{2.2}$$

While t_n is relatively easy to be measured, the correct determination of t_0 is more difficult. To overcome this problem it is convenient to use t_γ as start time, namely the detection of the γ-flash, and correct it for the time spent by gammas to travel from the spallation target to the experimental area, *i.e.* L/c. The time of flight is then:

$$TOF = t_n - t_\gamma + L/c. \tag{2.3}$$

As a first approximation the uncertainty on the neutron energy can be expressed as:

$$\frac{\Delta E_n}{E_n} = 2 \cdot \sqrt{\left(\frac{\Delta t}{t} \right)^2 + \left(\frac{\Delta L}{L} \right)^2}. \tag{2.4}$$

Figure 2.5 shows the classical and relativistic relation between the Time of flight and the incident Neutron Energy in the case of EAR1 (flight path 185 m) and EAR2 (flight path 19.5 m). One can observe that the relativistic effects are relevant starting around 100 MeV.

The uncertainties Δt and ΔL depend on the time resolution of the detectors, on the time width of the proton pulse and on the technique used to determine the flight path L. Those uncertainties are approximately constant against the neutron energy. A long flight path allows to reduce both

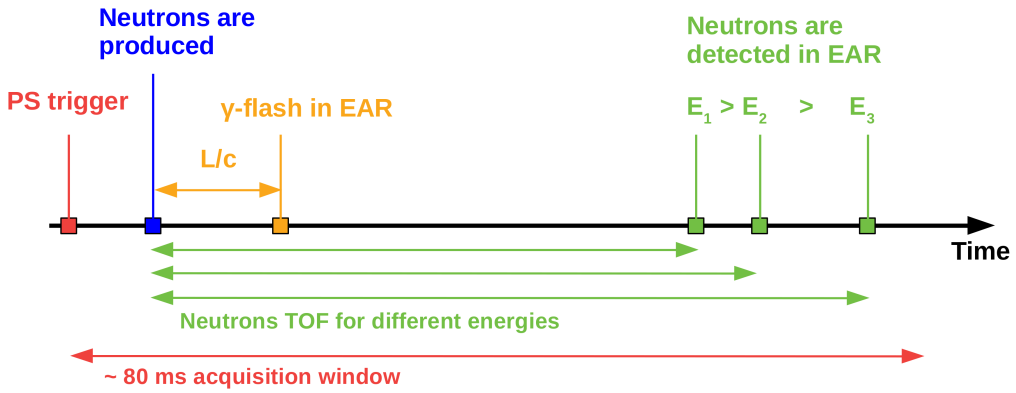

Figure 2.4: Events during each n_TOF pulse. A trigger is sent by the PS when the proton bunch is transferred to n_TOF beam line, followed by the spallation process when protons interact with the lead target. After a time L/c the γ-flash reaches the experimental areas, followed by neutrons, whose arriving time depends on theirs kinetic energy.

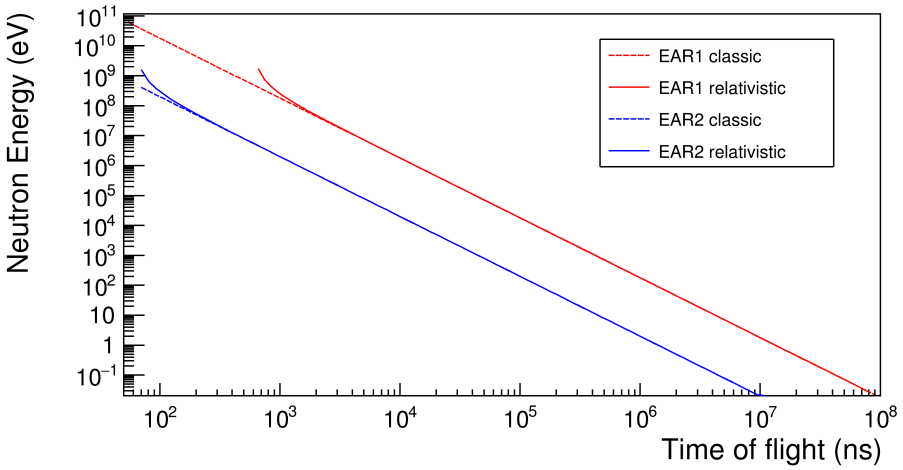

Figure 2.5: Classical and relativistic relation between the Time of flight and the incident Neutron Energy in the case of EAR1 (L = 185 m) and EAR2 (L = 19.5 m).

the ratios in the expression 2.4, moreover by improving the spallation target design the final uncertainty can be further minimized. Around the

world there are different facilities for accurate neutron cross section measurements, all based on the production of neutrons via spallation and time-of-flight technique. They mostly differ for the chosen spallation target and for the flight path length. Among the most active in the recent year are GELINA[85] at JRCIRMM (flight path 10, 30, 50, 60, 100, 200, 300, 400 m), DANCE[86] at LANSCE (20 m) and ANNRI[87] at J-PARK(22 and 28 m). n_TOF is the facility with the higher neutron flux per pulse and wider energy range. A comparison between the n_TOF neutron flux and some of these facilities is shown in section 2.1.4 (figure 2.9).

2.1.2 Experimental area 1

EAR1 is the first experimental area built at n_TOF, commissioned in 2001 and still in operation. For 13 years it has been the only experimental area of the facility before the development of the second experimental area in 2014. The 185 m long flight path provides a very good neutron energy resolution of 10^{-3} to 10^{-4} depending on the neutron energy, well suited to perform accurate measurements such as neutron capture cross sections. This area is located in an underground cave, at the same level of the spallation target, and is classified as Class A Laboratory, hence giving the possibility to handle unsealed radioactive material. The neutron beam line from the spallation target to the experimental area is bent at 10° with respect to the proton beam direction, in order to strongly reduce the quantity of forward-going relativistic particles generated by the spallation process. A sketch reporting the elements placed along the beam line is shown in figure 2.6.

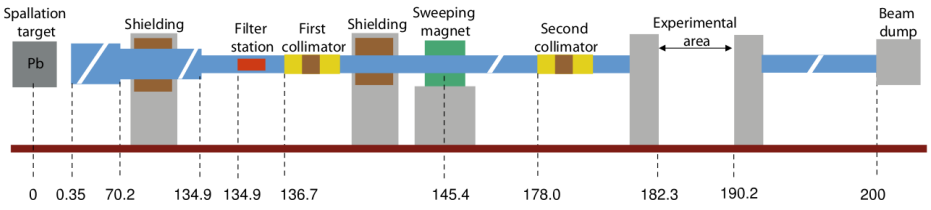

Figure 2.6: EAR1 beam line from the spallation target to the beam dump located at the end of the tunnel (≈ 200 m).

Two collimators along the beam line are designed to shape the beam,

reducing its diameter and suppressing the neutron halo. The second collimator in particular allows to switch between two different diameters, namely 2.2 cm, used in general for capture measurements, and 6 cm used for fission measurements. Furthermore, at a distance of 135 m from the spallation target is the so called filter station, that allows to insert disks of different materials to intercept the beam, in order to study the background by means of the black resonance technique [88]. Moreover, following the first collimator the beam crosses a sweeping magnet, where the charged particles are deflected and swept away. The neutral particles, such as γ-rays or π^0, are not affected. After the experimental area the neutrons travel along a short vacuum pipe till to the beam dump, consisting in a 49 x 49 x 47 cm^3 polyethylene block where three radiation monitors are placed for radiation safety purposes.

2.1.3 Experimental area 2

The second experimental area, built in 2014, is distant approximately 20 meters from the spallation target, along the vertical direction. A shorter flight path implies a higher neutron flux (a factor $\approx$ 35 compared to EAR1) and energy resolution around 10^{-3}. The availability of a high instantaneous neutron flux allows to perform accurate measurements even with short-lived radioactive samples (*i.e.* with very high activity), because of the higher signal to background ratio attainable, that makes it an excellent experimental site in the world for such a kind of measurements. The high n_TOF instantaneous flux and the fact that EAR2 is classified as a Class-A laboratory represents a unique environment, especially for handling extremely radioactive samples. Since its entry into operation, this experimental area made possible new measurements of particular interest in the framework of the big bang nucleosynthesis, the two beryllium destruction channels have been explored in order to possibly solve the cosmological lithium problem [89, 90].

A scheme of EAR2 beam line is reported in figure 2.7. The elements along the line are similar to those adopted for EAR1, with two collimators that shape the neutron beam, a sweeping magnet (in case of EAR2 it is a permanent magnet) and a filter box for background analysis. Since the spallation target is not optimized for the vertical direction, the lead upper

surface is not perpendicular to the beam, thus meaning that the thickness of the lead layer crossed by the neutrons is not uniform. Moreover, since the moderator layer containing borated water is not present on the top side, a larger thermal component is present in the flux. Finally, the wide angle (90°) between the proton beam and the EAR2 beam line implies that the high energy neutrons produced during the first stage of the spallation process due to the Intranuclear Cascade are missing, so that the neutron spectrum presents an energy limit of $\approx$ 200 MeV. Even though a shorter flight path guarantees a significantly higher neutron flux, some drawbacks are present. In particular, having the neutrons in EAR2 a shorter time of flight compared to EAR1, they are closer to the γ-flash and the detection requires detectors with faster recovery time. Moreover, the γ-flash is stronger and the missing borated water on top of the target, implies that the detectors are more easily saturated. Finally, shorter time of flight means worst resolution, about an order of magnitude larger than in EAR1.

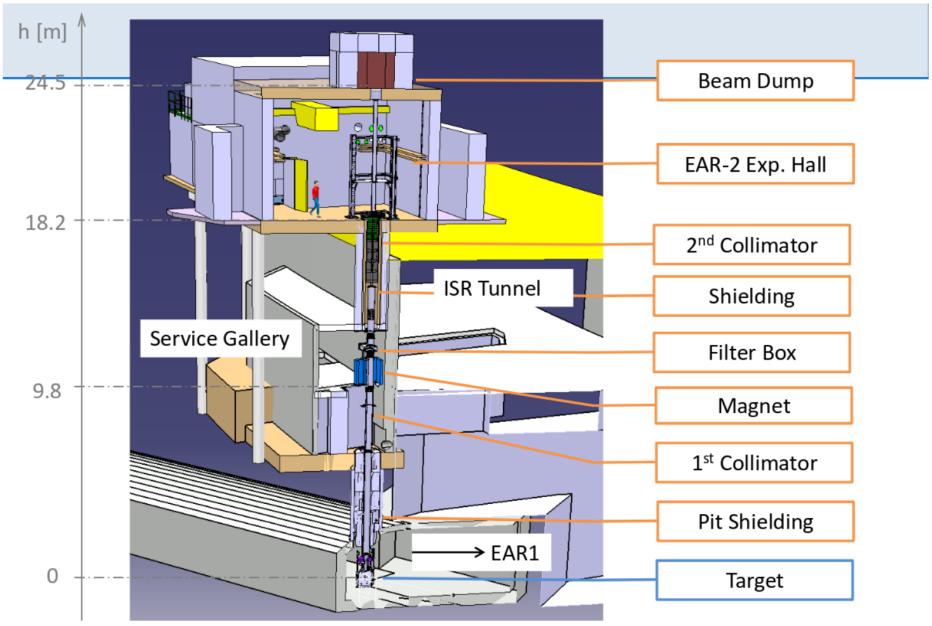

Figure 2.7: Scheme of the second n_TOF experimental area, the Class-A laboratory is located vertically over the spallation target approximately at $\approx$ 20 meters.

2.1.4 n_TOF neutron flux

As previously said, the different flight path to reach the two experimental areas of n_TOF implies that the two fluxes have peculiar characteristics both in term of integral and energy intervals. In figure 2.8 the comparison between the EAR1 (red) and EAR2 flux (blue) is shown. The EAR1 flux has an extremely wide range of neutron energies ranging from thermal to 1 GeV. The flux in the figure refers to the last n_TOF configuration (2011), that is characterized by the effects of the borated water as moderator, which was installed in the spallation target during the n_TOF-Phase2. This moderator significantly reduces the amount of low energy neutrons. In the interval from 1 eV to 100 keV the shape is almost flat, with a moderate but constant growth as the neutron energy increases. Beyond 100 keV the flux in both areas has a significant increase due to neutrons emitted in the second stage of the spallation process, during the processes of evaporation and fission, whose typical energy is up to 10 MeV.

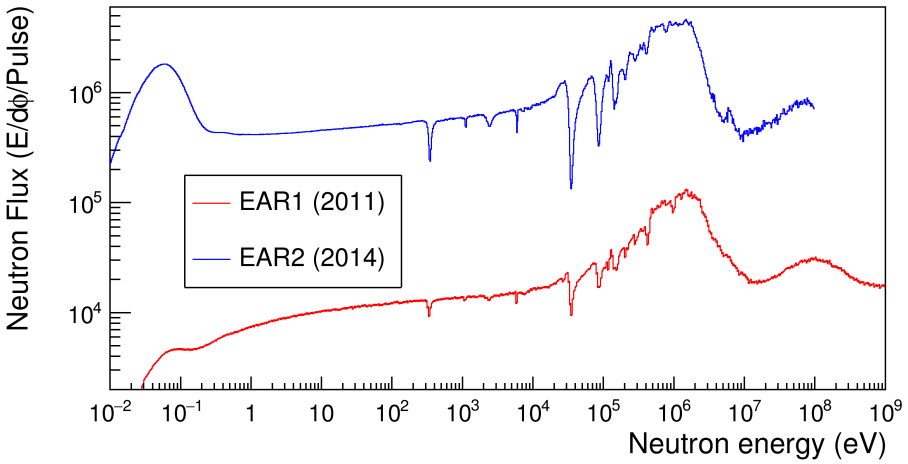

Figure 2.8: Comparison between between the EAR1 (red) and EAR2 flux (blue).

The behaviour of both fluxes as a function of the neutron energy present several absorption dips, in correspondence of resonances of the elements present in the beam line, in which a significant fraction of neutrons are absorbed or scattered off-beam. The largest contribute arises

from the aluminum vessel containing the spallation target, indeed the ^{27}Al(n,tot) cross section has huge resonances in the keV region. In particular aluminum is responsible for the large neutron absorption at 35 keV (smaller absorption dips due to aluminum are located at 5.9, 80, 120 and 150 keV). The dips are more pronounced in the EAR2 flux, since the spallation target used during the n_TOF-Phase2 was not optimized for the vertical direction, and larger thickness of aluminum were present. Apart from the difference in the low energy region, the flux shape at higher energy is very similar between EAR1 and EAR2. The number of neutrons per pulse, integrated in several energy intervals, is reported in table 2.2, together with the ratio between the two experimental areas.

Table 2.2: Number of neutrons per pulse, in several neutron energy ranges for EAR1 and EAR2, and their ratio.

Energy range (eV)	**Neutron/Pulse EAR1**	**Neutron/Pulse EAR2**	**EAR2/EAR1**
0.01 to 0.1	$5.03 \cdot 10^3$	$1.2 \cdot 10^5$	23.9
0.1 to 1	$1.33 \cdot 10^4$	$2.64 \cdot 10^6$	199
1 to 10	$2.07 \cdot 10^4$	$1.28 \cdot 10^6$	61.8
10 to 100	$2.6 \cdot 10^4$	$9.96 \cdot 10^5$	38.2
100 to 10^3	$2.96 \cdot 10^4$	$1.12 \cdot 10^6$	37.8
10^3 to 10^4	$3.33 \cdot 10^4$	$1.23 \cdot 10^6$	37
10^4 to 10^5	$4.54 \cdot 10^4$	$1.47 \cdot 10^6$	32.4
10^5 to 10^6	$1.34 \cdot 10^5$	$2.03 \cdot 10^6$	15.1
10^6 to 10^7	$1.61 \cdot 10^5$	$5.93 \cdot 10^6$	36.9
10^7 to 10^8	$5.49 \cdot 10^4$	$4.61 \cdot 10^6$	83.9

In figure 2.9 a comparison between a few time-of-flight facilities is

shown, with their respective fluxes reported in terms of neutrons per pulse per unit area (top panel) and neutrons per second per unit area (true flux, bottom panel) respectively. The extremely wide neutron energy range of n_TOF flux sticks out, in particular in EAR1 where it is possible to perform measurements up to 1 GeV. The higher number of neutrons per pulse respect to other facilities in the world is evident in the upper panel, in particular for EAR2. The neutron fluxes integrated in one second are shown in the bottom panel, that depend on the repetition rate available the facilities. At n_TOF the maximum repetition rate is limited by the mechanical stress that can be sustained by the spallation target, in particular by the target cooling time required after each proton pulse.

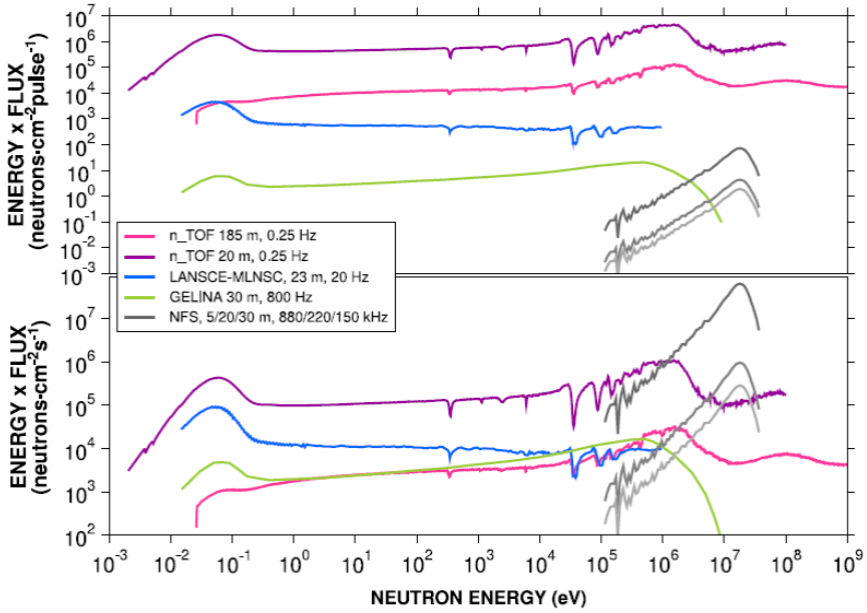

Figure 2.9: Comparison between different neutron beam facilities' flux for pulse (top panel) and for second (bottom panel).

2.1.5 n_TOF resolution function

The resolution function (RF) of the neutron beam is an important characteristic of any neutron beam facility, in particular for those where neu-

trons are produced by spallation and a low energy component is obtained by means of thermalization with a moderator around the target. In particular, the RF is defined as the distribution of the neutron flight time for neutrons of a given kinetic energy. Profiting by the relation between TOF and flight path, it is convenient to express the RF in term of flight path as:

$$L_{Eff} = L_{Geo} + \lambda(E_n), \tag{2.5}$$

where L_{Eff} is the effective length, L_{Geo} is the distance from the spallation target's exit window to the experimental area and $\lambda(E_n)$ is a pseudo-distance called moderation length, *i.e.* a convenient additional flight path which is a function of the neutron energy. Moreover, if expressed in term of the moderation length the dependence on the neutron energy results to be weaker. The main contribution to the RF is given by the moderation process inside the spallation target, whose typical size is small but not negligible compared to the flight path. Figure 2.10 shows the moderation insider the spallation target, during which the neutron travels an additional flight path $\lambda(E_n)$ depending on its kinetic energy. Since this additional distance fluctuates, the time-to-energy relation is not univocal: a given neutron energy value corresponds to a distribution of time of flights, and vice versa. In addition, the primary proton pulse duration (7 ns RMS) is not negligible for high energy neutrons and significantly contributes to the overall distribution.

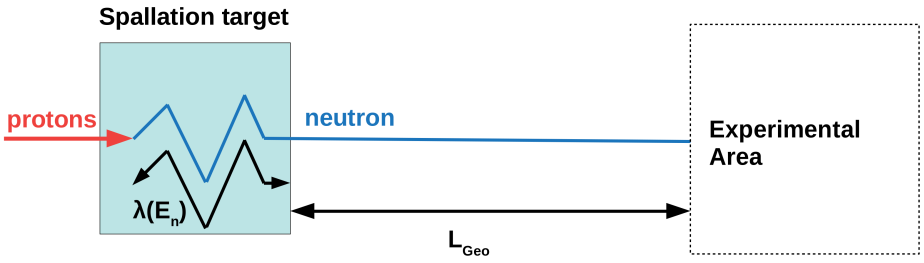

Figure 2.10: Sketch of the moderation process, after the production the neutron (blue line) travels an additional length inside the spallation target, depending on its kinetic energy.

The resolution function can not be measured directly but it needs to

be calculated analytically or estimated using Monte Carlo simulations. During n_TOF Phase1 an analytical approach was initially adopted, with a parameterization requiring 7 energy dependent parameters to describe the resolution function from 1 eV to 1 MeV [91], in order to be employed in the SAMMY[92] and REFIT[93] codes. However a numerical approach based on Monte Carlo simulations, performed with CAMOT[94] and FLUKA[95, 96] during Phase1 and with FLUKA and MCNP[97] during Phase2, was proved to be more effective in describing the n_TOF experimental conditions. The resulting resolution function has been afterward validated by measurements of well-known resonances.

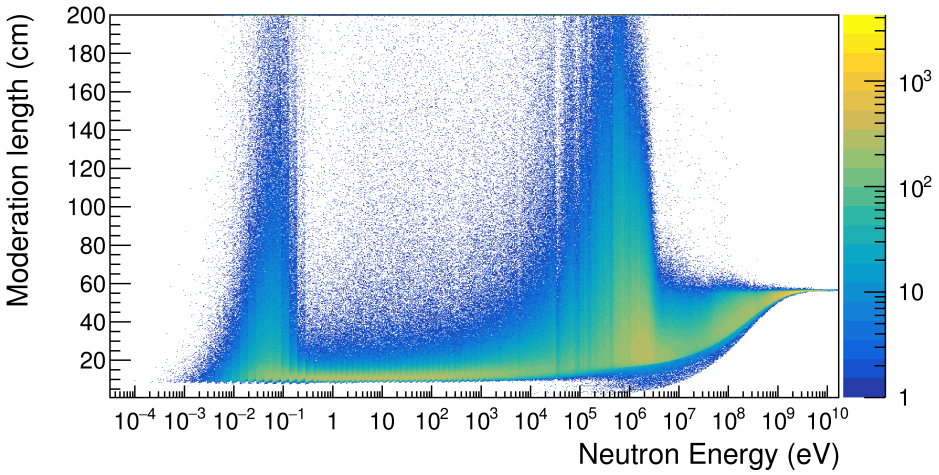

Figure 2.11: n_TOF resolution function, *i.e.* the distribution of the moderation length as a function of the neutron energy.

The numerical resolution function of n_TOF, *i.e.* the distribution of the moderation length as a function of the neutron energy is reported in figure 2.11. At a first glimpse one can notice that the moderation length distribution results to be larger at low energies and from 0.1 MeV to 10 MeV. At low energies the distribution is affected by the moderation process responsible for the production of thermal neutrons, in fact the collision of the neutrons with the nuclei is a stochastic process and the effective geometrical path could vary significantly. In the 0.1 MeV to 10 MeV interval the distribution is determined by the evaporation and fission processes

that produce these neutrons. At neutron energy $\approx$ GeV it becomes narrower and with an upper bound corresponding to the spallation target size, since the neutrons are mostly produced through the Intranuclear Cascade in the first layers of the target.

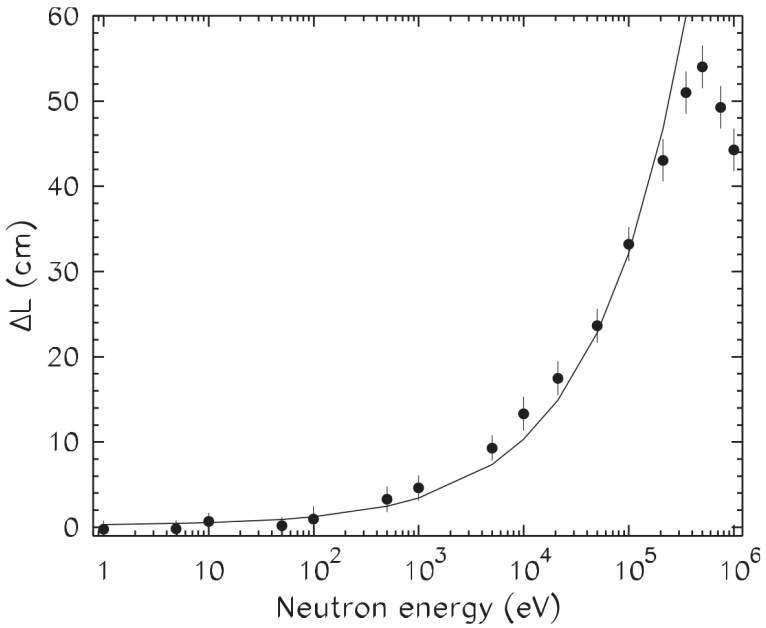

Figure 2.12: Energy-dependent term of the average moderation distance for neutron energies between 1 eV and 1 MeV, extracted from FLUKA+CAMOT simulations (symbols) and fitted with equation 2.6 (solid curve).

With an acceptable level of approximation it is possible to follow a simplified approach, as that proposed by Lorusso et al. [98]. In this approximation, the variable component of the flight path $\lambda(E_n)$ depends in average from the square root of the neutron energy, according to the expression:

$$\lambda(E_n) = 0.101 \cdot \sqrt{E_n} \tag{2.6}$$

The constant 0.101 presents in the formula 2.6 has been determined by fitting the results of the simulations made with FLUKA and CAMOT.

Figure 2.12 shows the average moderation distance calculated in the simulations and the resulting fit with equation 2.6. This approach is valid below few hundred of keV, hence over all the interval of interest for the present work. In case the measured cross section presents resonances, the application of the RF is required to correct them, thus improving the shape. In fact, the non univocal time-to-energy relation expressed by the resolution function implies that the measured resonance widths are larger than the values. Moreover, the asymmetric shape of the moderation length distribution determines the presence of a low energy tail in each resonance in the experimental spectra.

2.2 Experimental apparatus

The ^{235}U(n,f) cross section has been measured relative to two reference reaction, whose cross sections are defined by the IAEA as standards of measurement, namely ^{6}Li(n,t) and ^{10}B(n,α). The two reference reactions are:

$$ {}^{6}_{3}Li \; + \; {}^{1}_{0}n \longrightarrow {}^{3}_{1}H(2.73MeV) \; + \; {}^{4}_{2}He(2.05MeV) \tag{2.7} $$

$$ {}^{10}_{5}B \; + \; {}^{1}_{0}n \longrightarrow \begin{cases} {}^{4}_{2}He(1.78MeV) + {}^{7}_{3}Li(1.01MeV) & BR \approx 94\% \\ {}^{4}_{2}He(1.47MeV) + {}^{7}_{3}Li^{\star}(0.84MeV) & BR \approx 6\% \end{cases} \tag{2.8} $$

Both are defined as standards from 0.025 eV (thermal neutrons) up to 1 MeV and have a 1/v dependence, apart from a wide resonance in the ^{6}Li(n,t) cross section at $\approx$ 250 keV. Such a smooth behavior represents a clear advantage when using these reactions as reference. Indeed, the presence of narrow resonances would require the use of the resolution function, making the analysis of the reference reactions more complex and introducing additional sources of uncertainty. Moreover, in presence of a narrow resonance even a small mismatch in the time-to-energy conversion would result in a wrong evaluation of the reference cross section at that energy.

The experimental apparatus, specially made for the experiment, was based on silicon detectors arranged in a suitably mechanical setup. A sketch of this setup is reported in figure 2.13. In details there was six single pad silicons detectors and three pairs of ^{6}Li, ^{10}B or ^{235}U samples respectively, which characteristics are listed in table 2.3. Each detector was coupled with a single sample arranged parallel to the silicon surface at a small distance ($\approx$ 1mm). The separation between the two was kept as small as possible in order to maximize the geometrical efficiency. The samples and detectors were mounted on PCB frames and inserted into dedicated grooves in the aluminum support, to guarantee a high mechanical stability and the correct alignment of all the elements.

During the measurement the experimental apparatus was placed directly on the neutron beam, so that all the elements were crossed by the incoming neutrons approximately in the central position. For each reaction the two detectors were arranged in a back-to-back configuration, hence the succession of the elements crossed by the neutron beam was sample-detector-detector-sample. In this way the first detector measured the reaction products emitted in the forward direction with respect to the incoming beam, whereas the second detector measured the products emitted in the backward direction. Every detector was only hit by reaction products emitted by the associated sample, since the other silicons and the aluminum backings shielded it from the products emitted by other samples. This arrangement was chosen to minimize the systematic uncertainty that can arise from the angular distribution of the reaction products. Indeed, for the evaluation of the detection efficiency we made use of the best estimate of the angular distribution of the reaction products, provided by ENDF/B-VIII, that is based on few partial measurements and theoretical guesses. With the adopted arrangement any possible overestimation in the forward or backward efficiency is compensated to a large extent by the detector in the opposite direction.

In the following the six silicon detectors will be named as Li_f, Li_b, B_f, B_b, U_f, U_b, standing respectively for ^{6} Li, ^{10}B, ^{235}U, forward and backward with respect to the beam direction.

The total length of the setup was about 10 cm. Even though the samples have different shape and size, they were much larger than the neutron beam width of Gaussian shape with σ = 7 mm. The setup was

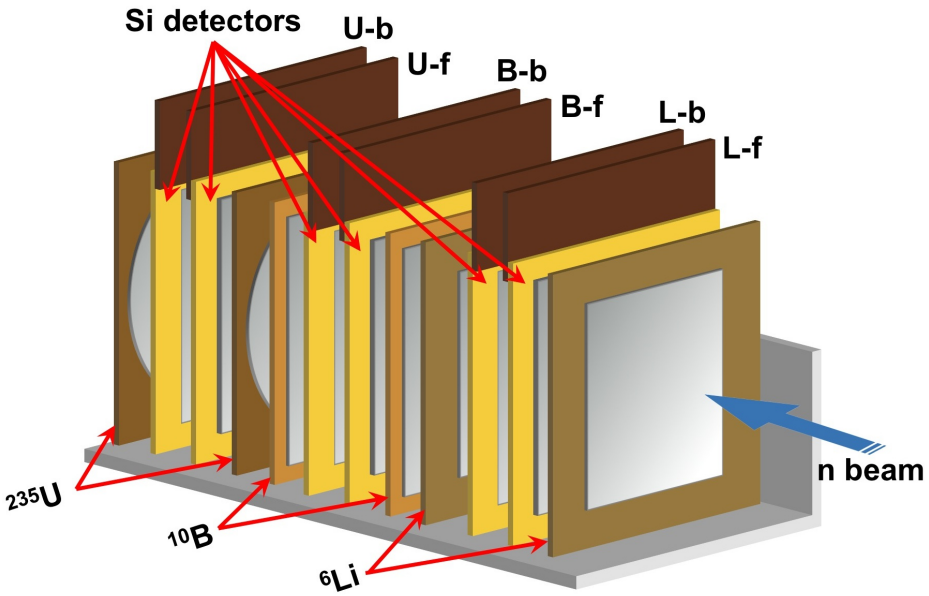

Figure 2.13: Sketch of the experimental setup. The neutron beam impinges on the back side of the first lithium fluoride sample and crosses all the detectors and samples.

aligned by using two gafchromic, that are films containing a dye which changes color when exposed to ionizing radiation [99], so that the shadow of the beam is impressed after a suitable irradiation time. The impressed area corresponding to the beam spot revealed a distance of the beam center from the axis of the detectors of 1 cm in the horizontal direction and 0.5 cm on the vertical. Because the detectors and samples sizes were much larger than the neutron beam, this misalignment did not represent a problem and therefore the apparatus position was left unchanged. The alignment procedure with the gafchromic films assured an accuracy of 1 mm, and the effect of this uncertainty was later studied in detail with the Monte Carlo simulation described in chapter 4 and duly taken into account.

The adoption of the silicon detectors presents a series of advantages, in particular the good energy resolution allows an efficient discrimination between the reaction products in each of the two reference reactions. Moreover, in previous measurements [89, 90] we ascertained that silicon

Table 2.3: Characteristics of the six samples (two for each type of deposit).

Material	**Enrichement**	**Size (mm)**	**Thickness**	**Atoms/cm^2**	**Backing**
LiF	95% ^{6}Li	$\square$ 47 $\times$ 47	1.89 (3) μm	$1.14{\cdot}10^{19}$	50 μm
B_4C	100% ^{10}B	$\square$ 70 $\times$ 70	0.08 (5) μm	$8.28{\cdot}10^{17}$	18 μm
H_2O_2U	99.93% ^{235}U	$\oslash$ 40	0.145 (16) μm	$6.18{\cdot}10^{17}$	250 μm

detectors were substantially immune from radiation damage induced by the n_TOF neutron beam during a time span of two months, therefore their radiation hardness was good enough to ensure a good stability during the whole measurement. Despite silicons have already been used at n_TOF to detect charged particles also in-beam configuration, the present measurement represented the first case they were employed to detect fission fragments. In light of the high accuracy results which will be shown in the next chapters, this technique proved to be highly effective to perform cross section measurements of neutron induced fission reactions, most importantly with small systematic uncertainty. It is currently under study the opportunity to perform a campaign of fission cross section measurements with experimental equipements having the same design concept.

As described above, for each reaction a configuration with two samples and two silicon detectors was employed. While the emission of the fission fragments results to be isotropic in the energy range of interest for this measurement, for both the reference reactions the angular distribution depends on the neutron's kinetic energy. This results into a detection efficiency that depends on the neutron energy. The correction for this effect was estimated by means of a dedicated Monte Carlo simulation code, and is described in detail in section 4.3. The forward/backward configuration with large solid angle covered by the detectors makes up for any forward-backward anisotropy, and to a large extent it reduces the dependence of the estimated efficiency on any systematics, in particular on the angular distribution of reaction products.

The single pad silicon detectors have an active area of 5x5 cm^2, and

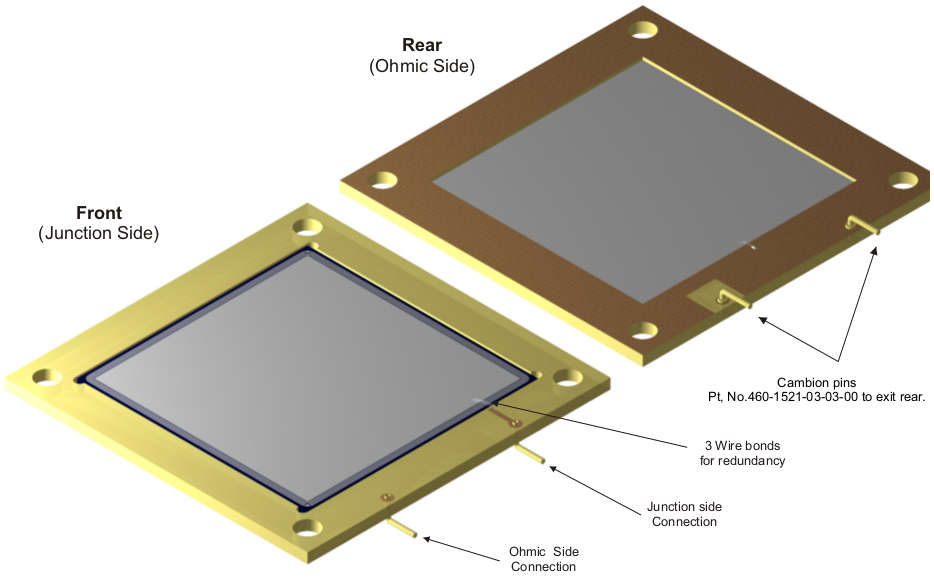

Figure 2.14: Sketch of a silicon detector employed for the measurement, these silicons are single pad 5x5 cm^2 and 200 μm thickness.

like for the active samples this area was much larger than the beam size, allowing to relax the need of a very accurate alignment. Their thickness was 200 μm, thicker than the maximum range of the reaction products and hence sufficient to stop all of them. The most penetrating particles were the tritons generated in the ^{6}Li(n,t) reaction, with a range of 50 μm in silicon. On the other hand the α-particles produced in the ^{10}B(n,α) reaction, and more the fission fragments, have a shorter range. The detector datasheet specifies the presence of a 500 nm aluminum dead layer on the entrance window of the silicon diode, whose final effect was to slightly modify the shape of the energy spectra, in particular for the products emitted at very large angles. This effect is more relevant for the detectors coupled with ^{10}B samples, given the higher stopping power of the alphas due to the relatively low Q-value of the ^{10}B(n,α) reaction. Clearly the presence of this layer has been included in the Monte Carlo simulations code, as will be described in detail in chapter 4.

A picture of the assembled experimental apparatus is reported in figure 2.15. The setup was positioned inside the reaction chamber shown in figure 2.16, which was kept at 10^{-6} mbar during the measurement, in

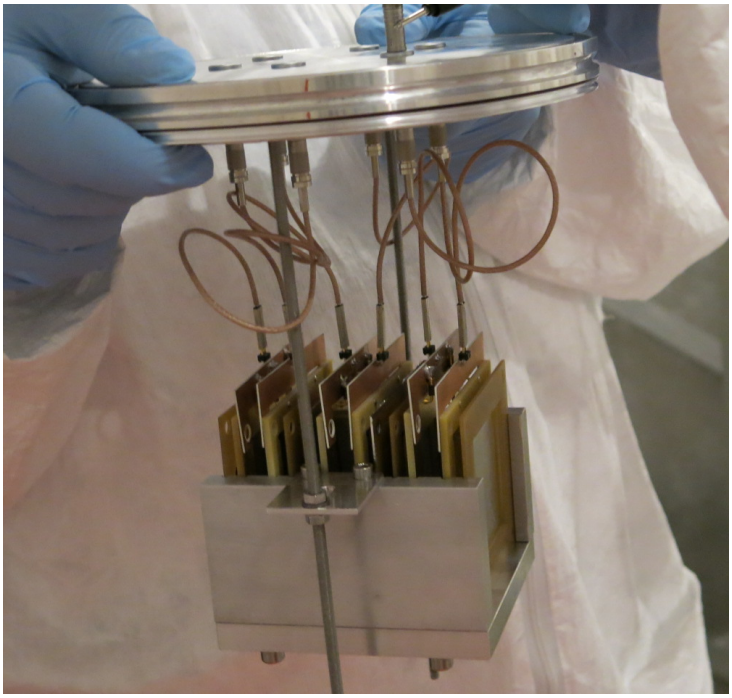

Figure 2.15: The experimental setup during its installation. The detectors and samples are in place on the aluminum support that is to be fixed on the reaction chamber's upper flange.

order to prevent the energy loss of the reaction products in the ≈ 1 mm distance between each sample and the associated detector. The front-end electronics for the detectors consisted of the MPR-16-LOG multichannel linear-logarithmic preamplifier, produced by Mesytec [100], followed by six ORTEC 474 timing filter amplifier modules [101]. The preamplifier has a linear behaviour up to a deposited energy of about 10 MeV, while above this value its response becomes logarithmic. The choice of this preamplifier has been motivated because this lin-log behaviour minimizes the deleterious effects of the γ-flash, that is particularly relevant considering that the detectors were directly exposed to the neutron beam. The full waveforms of detector signals were acquired by the standard n_TOF Data Acquisition System[102], based on SPDevicesADQ14DC4C cards of 1 GS/s maximum sampling rate, 14 bits resolution and 256 MBytes onboard memory and stored on the CERN's advanced storage manager[103]

(CASTOR).

Figure 2.16: The experimental setup installed in the first n_TOF experimental area. The setup was contained in the aluminum reaction chamber, the neutron beam came from the wall on the left and reached the chamber traveling through the shown carbon fiber vacuum pipe.

Chapter 3

Data Analysis

3.1 Pulse Shape Analysis

The high-performance digital data acquisition system of n_TOF operates by sampling and recording the detectors output waveforms for each beam pulse, throughout the overall time-of-flight range, that in EAR1 is around 100 ms. The first step of the offline data analysis is to select the useful detector pulses in the stored waveforms and calculate their corresponding time-of-flight and amplitude with the best resolution and Signal to Noise ratio. This task is carried out by a powerful and flexible code developed specifically for n_TOF [104], named *Pulse Shape Analysis* (PSA). The PSA software handles the wide variety of pulses produced by the detectors employed in the experiments, with a minimal number of explicit assumptions about their features, based on a pulse template adjustment and a set of analysis parameters bound to each detector type.

In this paragraph the term signal refers to the 100 ms continuous stream of data (waveform), recorded with a 1 GHz sampling rate by the n_TOF data acquisition system (DAQ). The first aspect addressed in the PSA is the recognition of each pulse and the evaluation of its correct amplitude: the whole procedure is illustrated in the example of figure 3.1. In the top panel the signal recorded from one of the silicon detectors is shown in black, while the red line represents the baseline that is calculated by the PSA routine. The middle panel shows the pulse tagging

procedure, that is based on the check of the correct sequence of crossing two thresholds by the signal derivative. For each i-th point the derivative is calculated with the following expression:

$$d_i = \sum_{j=1}^{min[N,i,P-1-i]} (s_{i+j} - s_{i-j}) \tag{3.1}$$

where s_i is the value of the signal in the i-th point and N is a step-size parameter to be suitably chosen. P is the total number of points and its role in the upper index of the sum, as well as i, is to cope with the start and end limits of the signal. In order to maximize the Signal to Noise ratio, a reasonable value for N should be larger than the period of the noise and shorter than the pulse width. In order to recognize the presence of a valid pulse in the recorded signal, its derivative must cross two predefined thresholds in a given order. These thresholds must be chosen to reject most of the noise and at the same time preserve the lowest pulses, therefore it is convenient to express the thresholds in terms of the root mean square (RMS) of the noise. When the step-size parameter N is optimized, the distribution of the derivative values follows a quasi-Gaussian shape. The PSA performs a preliminary Gaussian fit of the derivative distribution, and the resulting standard deviation is adopted as the RMS of the noise. The thresholds values are set at ± 3.5 RMS, that under the assumption of normally distributed noise correspond to a 99.95% confidence level. Valid pulses are recognized by checking their correct threshold-crossing sequence, that in our case is lower-lower-upper-upper. The final value of the step-size parameter used for the Li and B detectors was N = 300, while for the U detectors was N = 200. As prescribed by the PSA, the values for the U detectors are approximately equal to the pulses rise time ($\approx$ 200 ns), while for Li and B detectors are slightly higher, in order to take into account the higher noise.

Once the pulses are correctly recognized the routine calculates the baseline, choosing one among several available methods. The baseline calculation method used for our analysis was the *weighted moving average*, which is the most appropriate whenever a clear information about the baseline is available [105]. The baseline values are calculated by using the

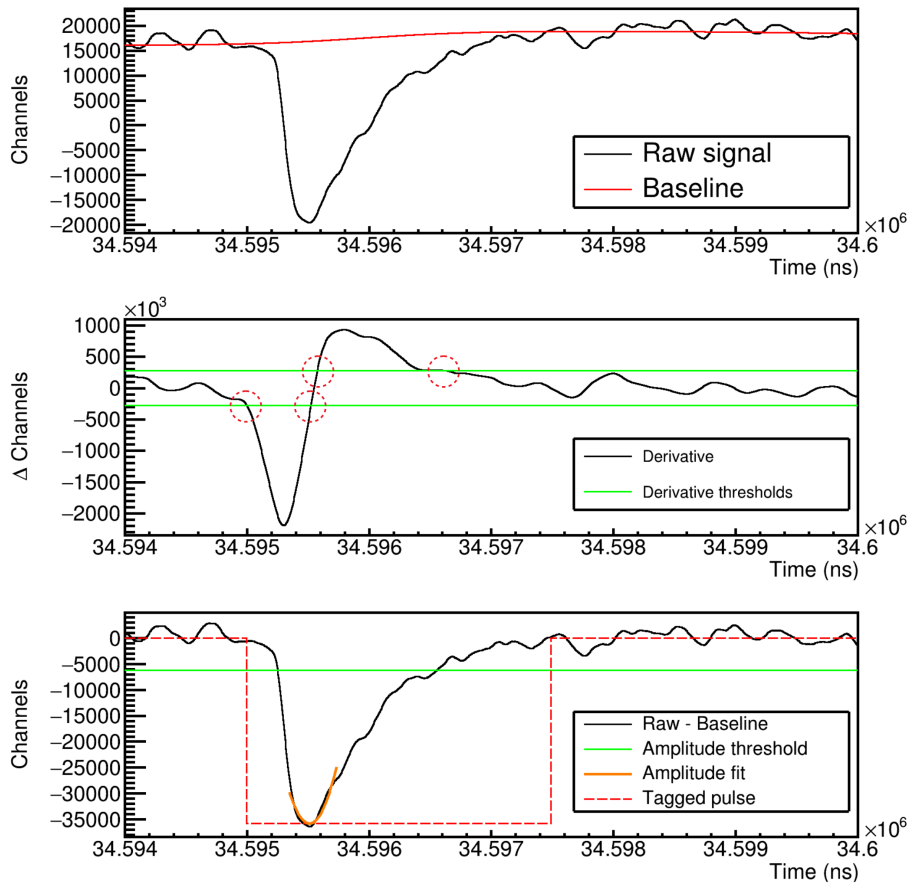

Figure 3.1: Top: raw signal with the baseline calculated thought the moving average method. Middle: derivative of the signal and thresholds for the pulse recognition, the red dashed circles indicated the four thresholds crossing. Bottom: signal after the baseline subtraction with a parabolic fit done to determine the amplitude (orange) and the threshold.

following expression:

$$b_i = \frac{\sum_{j=max[0,i-N]}^{min[i+N,P-1]} s_j w_j \{1 + cos[(j-i)\frac{\pi}{N}]\}}{\sum_{j=max[0,i-N]}^{min[i+N,P-1]} w_j \{1 + cos[(j-i)\frac{\pi}{N}]\}} \tag{3.2}$$

where weights w_j are suitably set so that inside the recognized pulses

their value is much lower than unity, thus excluding the pulses from the baseline calculation. The final step for the pulse shape analysis is finalized to extract the pulse amplitude, by choosing one among three different methods: search for the highest point, parabolic fitting to the top of the pulse and a predefined pulse shape adjustment. Since the silicon detector signal was shaped by the preamplifier, the pulse shape depended on the characteristics of the preamplifier and was pretty smooth. The chosen method was the parabolic fit, which was performed in a small interval around the maximum value of each pulse. Clearly it represents a better option than simply selecting the highest point and at the same time does not require to define a *predefined pulse*, whose definition contains a dose of arbitrariness. In the example of figure 3.1 the fit of the pulse performed after the baseline subtraction, is shown in orange.

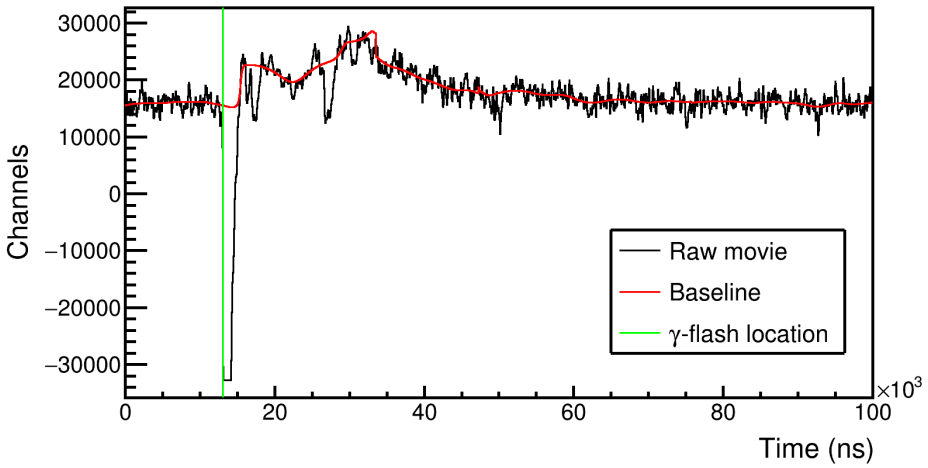

Figure 3.2: Beginning of the signal measured in a silicon detectors (black), the green line indicates the location of the γ-flash while the red line is the baseline calculated with the *weighted moving average* method.

The final step of the PSA optimization has been the correct recognition of the γ-flash. Indeed, the rising edge of the γ-flash represents the reference start signal to measure the time-of-flight of each pulse, making its identification a key aspect for a correct time-to-energy conversion. Several options are available that can be selected depending on the detector response to the γ-flash, in particular in our case it was identified as the

first signal that crosses a fixed high amplitude threshold. The adopted digital threshold value was -20000 DAQ-channels, approximately an order of magnitude larger than the electronic noise, corresponding to ≈ 40 mV . Figure 3.2 shows the signal in the proximity of the γ-flash (black line), that occurred about 13 μs after the DAQ started, triggered by the protons-on-target signal coming from the accelerator. The vertical green line indicates the time value where the PSA identifies the γ-flash, while the red line is the baseline, calculated with the *weighted moving average* method. The baseline highlights an instability due to the preamplifier recovery time after the huge saturated pulse. In figure 3.3 a zoom of the γ-flash region is shown.

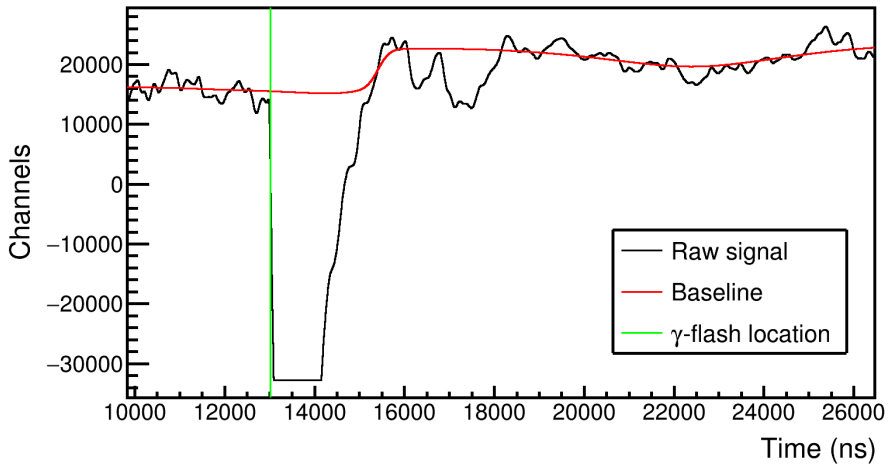

Figure 3.3: Zoom of figure 3.2, it can be observed that in this case the γ-flash saturates the detector.

3.2 Time to energy conversion

The time to energy calibration profited by the high quality data measured with the fission silicon detectors. The presence of many well-known resonances in the ^{235}U(n,f) cross section allowed to perform a reliable preliminary estimation of the flight path length, in particular exploiting forty prominent resonances between 2 and 35 eV (figure 3.4).

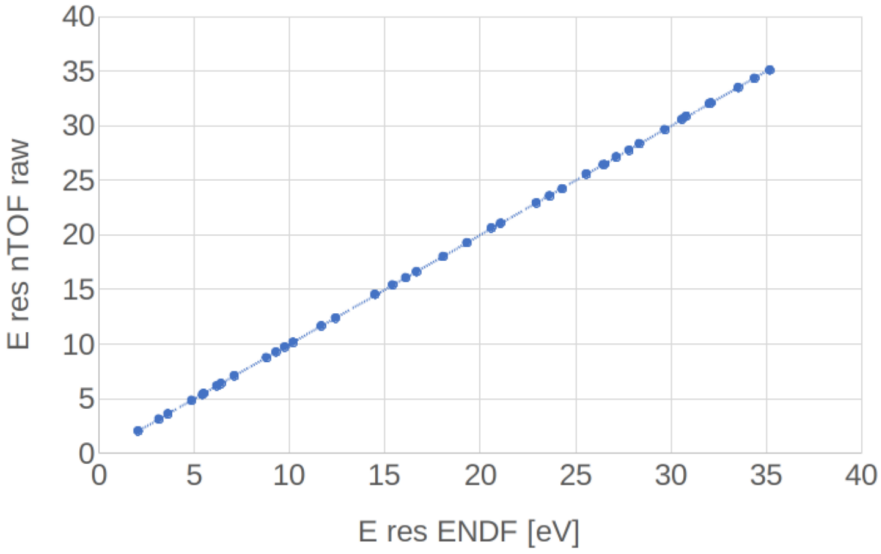

Figure 3.4: Energy of the resonance in the ENDF/B-VIII evaluated ^{235}U(n,f) cross section *versus* energy in the n_TOF experimental data after the preliminary time-to-energy calibration.

Once a preliminary estimate was obtained, the flight path length was fine-tuned through the minimization of the χ^2 between experimental data and libraries in a well-defined energy interval. The energy interval chosen for its minimization was between 8.4 and 35 eV, in order to exclude the dip at 7.8, where very few counts were expected. Figure 3.5 shows the value of the χ^2/NDF as a function of the flight path, calculated using the evaluation of ENDF/B-VIII as a reference. The adopted value for flight path of the U_f detector is 183.49(2) m, corresponding to the minimum value of $\chi^2/\text{NDF} \approx 4.5$. Such a rather large χ^2/NDF value was due to the fact that no resonance shape correction had been applied at this stage of the analysis (Doppler effect, resolution function): several shape differences were present between the raw data and the reference library, even though the resonance positions and amplitudes were correct. The flight path for all the other detectors was then calculated with respect to U_f, since the experimental apparatus geometry was known with an accuracy smaller than 1 mm, negligible compared to the 2 cm uncertainty obtained

with the χ^2 minimization. Considering that, no additional source of uncertainty had been introduced and the flight path was assumed to be known with an uncertainty of 2 cm, the relatively uncertainty of tof was calculated to be $1.1 \cdot 10^{-4}$.

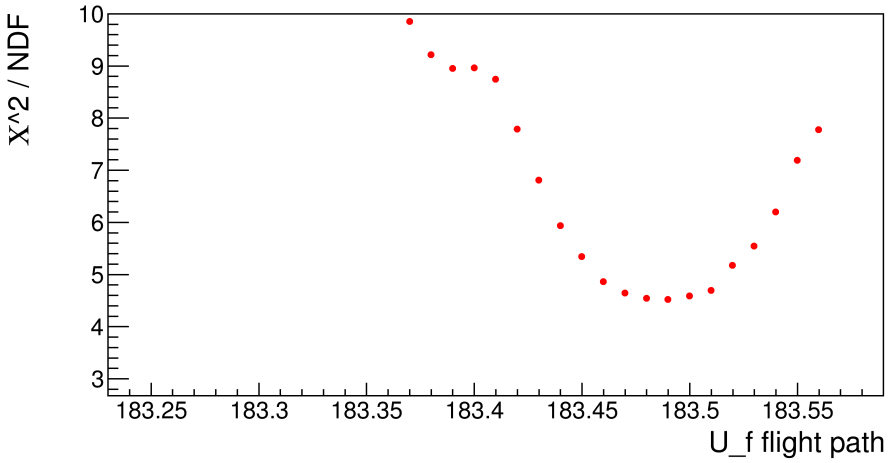

Figure 3.5: χ^2/NDF between experimental data and ENDF/B-VIII library in the neutron energy interval between 8.4 and 35. eV for different flight paths. The adopted value is 183.49(2) m.

To verify the accuracy of this procedure, we profited of the aluminum resonance at 5.9 keV, visible as a narrow absorption dip in the n_TOF flux, due to a significant amount of aluminum along the beamline. In figure 3.6 the neutron flux measured with the Li_f and Li_b detectors in the energy interval of the aluminum resonance is shown. The neutron energy corresponding to this absorption dip was estimated with a Gaussian fit, whose mean value is 5903.3±1.3 eV, compatible with the resonance energy value provided by ENDF/B-VIII library of 5904.47 eV.

3.3 Reaction tagging

The reaction products were selected on the basis of the energy deposited in the silicon detectors, for each detector the deposited energy *versus* neutron energy is represented in the two-dimensional scatter plot shown in

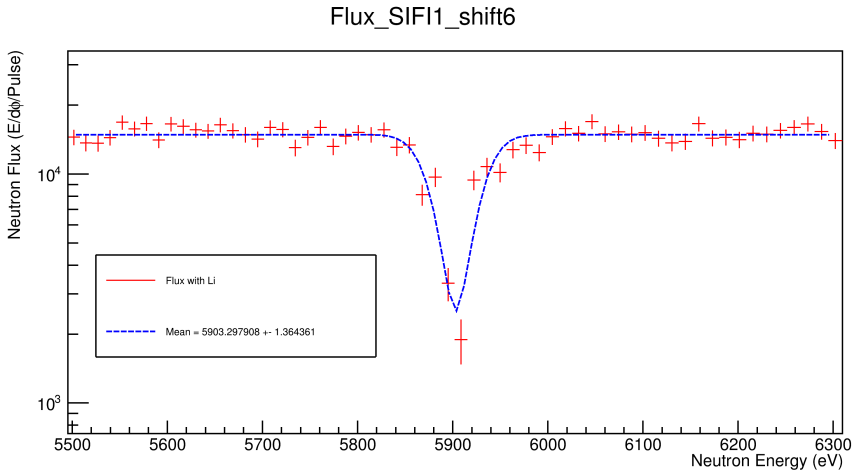

Figure 3.6: Neutron flux measured with Li_f and Li_b detectors in the energy region of the aluminum resonance at 5904.47 eV and the Gaussian fit to check the correctness of the obtained time-to-energy relation.

the figures 3.7, 3.9 and 3.11. The plots on top refer to the data measured by the detectors placed in the forward direction with respect to the beam direction, while the bottom plots refer to the detectors in the backward direction. In each plot the red line represents the experimental threshold used to discriminate the reaction products with the higher energy, that are tritium for ^{6}Li, alpha particles for ^{10}B and fission fragments for the ^{235}U samples. As clearly evident from the Li and B plots, the threshold values depends on the incident neutron energy because of the kinematic effects and the angular anisotropy of the products. The kinetic energy boost starts to be significant from a few keV, showing a slight increase of the deposited energy in the forward direction, and a decrease in the backward. But the effect that contributes more significantly to the shape change of the amplitude spectra, and consequently to the neutron energy behaviour of the threshold, is due to the angular anisotropy of the reaction products as a function of the neutron energy. The emission angle of the charged particles is particularly relevant since it determines the effective thickness of the crossed samples, the dead layers included, and hence affecting the energy lost by the particles before to reach the sensitive re-

gion of the detectors. The thickness of boron carbide samples was only 0.080 μm, thinner than the 0.5 μm of the aluminum dead layer on the detectors, that thus provided the main contribution to the energy loss. On the contrary, the 1.79 μm thickness of the lithium fluoride samples was larger than the aluminum dead layer, therefore the sample played the main role in the energy loss.

The plots in figure 3.7 are related to the detectors coupled with the lithium fluoride samples. The thresholds (red line) indicate how the tritons produced in the reaction ^{6}Li(n,t)^{4}He were selected, rejecting the events due to alpha particles, background and electronic noise. This cut was very effective mainly because the energy of tritons (2.73 MeV) is significantly higher than the 2.05 MeV of the alpha particles, and in addition the energy loss of the alphas in the dead layer was significantly larger. The electronic noise was rather low and did not affect the measurement results.

For the Li_b detector the threshold was set in the minimum of the valley between tritons and alpha particles, identified by means of a parabolic fit. As previously said, the amplitude (channel value) is a function of the neutron energy, because of the reaction anisotropy in the keV neutron energy range, therefore the position of this minimum varies and the experimental threshold follows its behaviour. Due to a not well understood electronic mishap, the Li_f detector response was of lower quality than expected, and the minimum of the valley between tritons and alphas was not reliably defined at all neutron energies. In this case the threshold was set closer to the triton peak, at a value chosen by means of a suitable Monte Carlo simulation which is described in chapter 4. Such a solution has allowed to overcome this difficulty at the price of a reduction of the detection efficiency, nonetheless not significantly affecting the statistical uncertainty because of the high reaction yield. The forward focusing of the reaction products increases with the neutron energy and implies a decreasing of the average energy lost in the dead layer. For such a reason the triton and alpha peaks move to higher amplitudes in the keV region. The two plots shown in figure 3.8 report the projection on the Y-axis of the two-dimensional scatter plot 3.7 integrated in three energy intervals of interest. The upper plot refers to the detector in the forward direction, for which the energy spectrum shifts to higher values of amplitude,

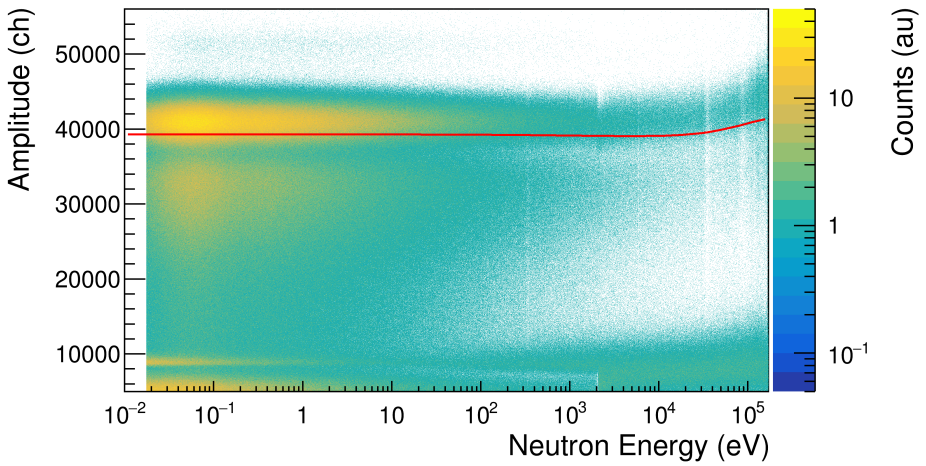

(a) Li_f

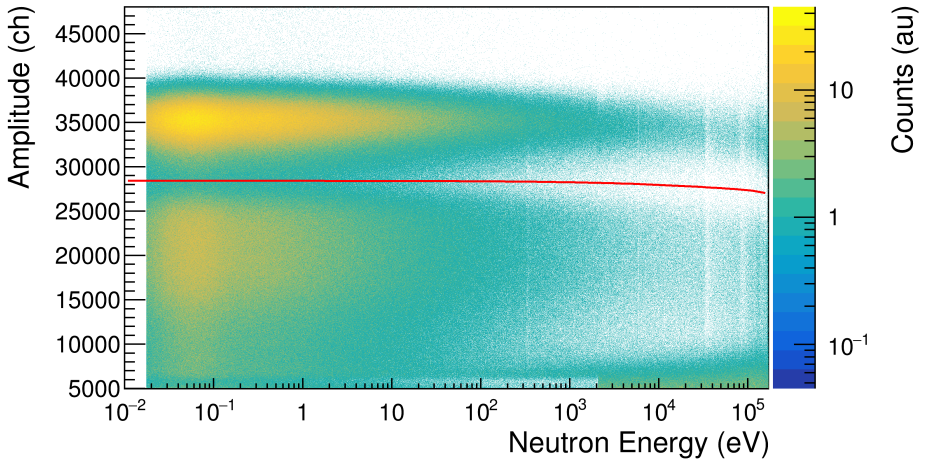

(b) Li_b

Figure 3.7: Two-dimensional scatter plot of the deposited energy *versus* the incident neutron energy for the detectors coupled with lithium fluoride samples.

while the bottom plot shows the amplitude spectra of the backward detector Li_b, which shifts toward lower values. In any case the shift results to be relatively small for neutron energies below 10 keV, while the large

decrease of the counts is due to the typical 1/v behavior of the ^{6}Li(n,t) cross section.

The case of boron carbide is slightly more problematic, since the Q-value of ^{10}B(n,α)^{7}Li reaction is 2.310 MeV with a branching ratio of 94% and 2.792 MeV with the branching ratio of 6%, when the ^{7}Li is produced in the ground state. Most of the alpha particles are therefore produced with a kinetic energy of 1.47 MeV, that means a high energy lost in the dead layers. For such reason, the boron carbide samples has been chosen much thinner than the lithium fluoride, but with the drawback of a lower counting rate and the consequent larger statistical uncertainty. The alpha particles can be easily separated by the events due to ^{7}Li, that is produced with only 0.84 MeV kinetic energy and overlaps with the background and the electronic noise. As in the case of lithium, the experimental threshold was set in the minimum of the valley between the alpha particles and the ^{7}Li+noise. The two-dimensional scatter plot relative to B_f and B_b detectors are shown in figure 3.9, with the red line representing the experimental threshold. Because of the electronic noise background, the threshold for the backward detector B_b increases for neutron energy larger than $\approx$ 50 keV.

In analogy with the lithium case, in figure 3.10 the Y-axis projection of the two-dimensional plots of figure 3.9 are shown, with the three neutron energy intervals of interest that have been considered. As for the lithium detector, increasing the neutron energy the amplitude spectra of the forward detector B_f presents a shift toward higher values, while a slight shift in the opposite direction is observed in the backward detector B_b. Respect to the lithium detectors the energy dependence is less pronounced, mainly because of the lower anisotropy in the angular distribution of the reaction products. Moreover, it is possible to see the increasing contribute of the background in the keV neutron energy region, caused by the proximity to the γ-flash. Indeed, in both the plots the red curves (higher neutron energy) show a larger number of background counts compared to the green one, even though the alpha peak contains fewer events.

The case of the uranium samples was significantly different, first of all because in the energy range of interest the fission fragments are emitted isotropically. Moreover, the boost induced by the kinetic energy of

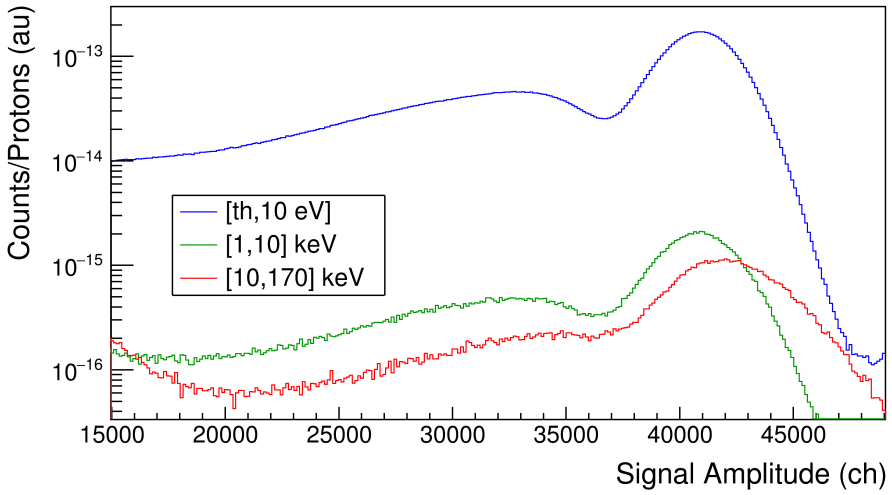

(a) Li_f

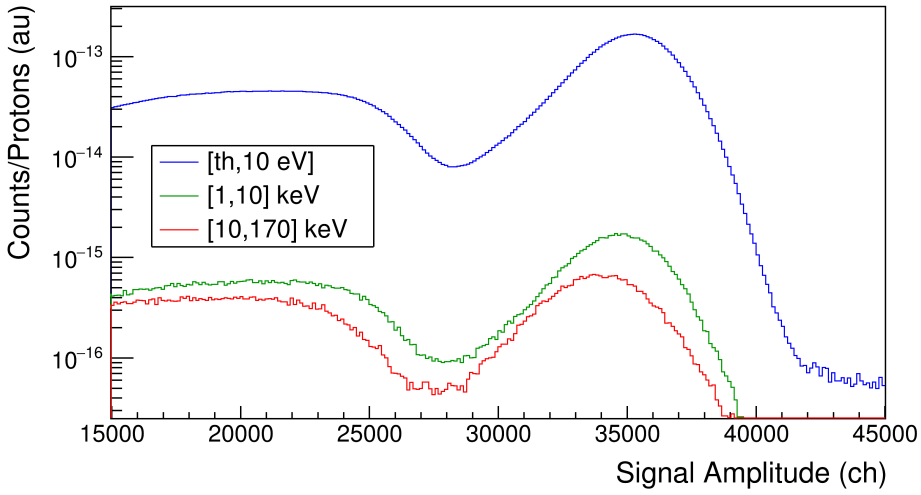

(b) Li_b

Figure 3.8: Projection of the two-dimensional plots of figure 3.7 on the vertical axis for three neutron energy intervals of interest. Top: amplitude spectra for the detector in the forward direction, where the spectra move to higher values as increasing the neutron energy. Bottom: same figure for the backward detector, in this case the spectrum shifts to slightly smaller values (see text).

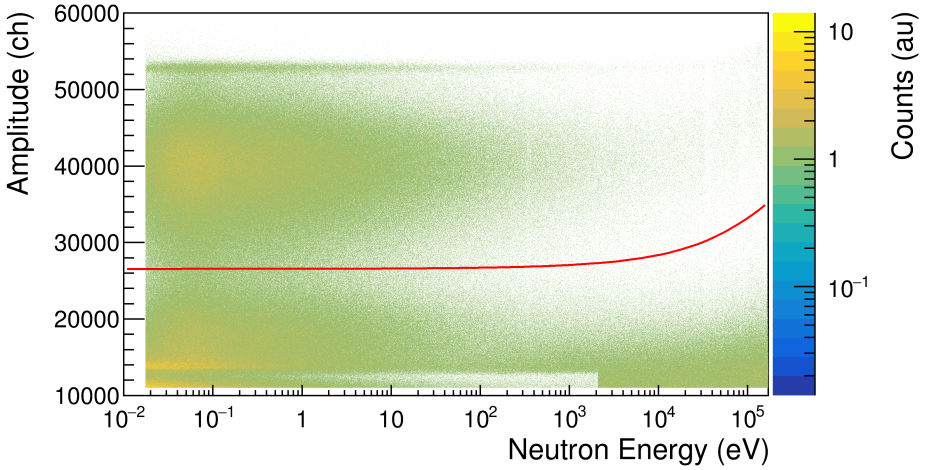

(a) B_f

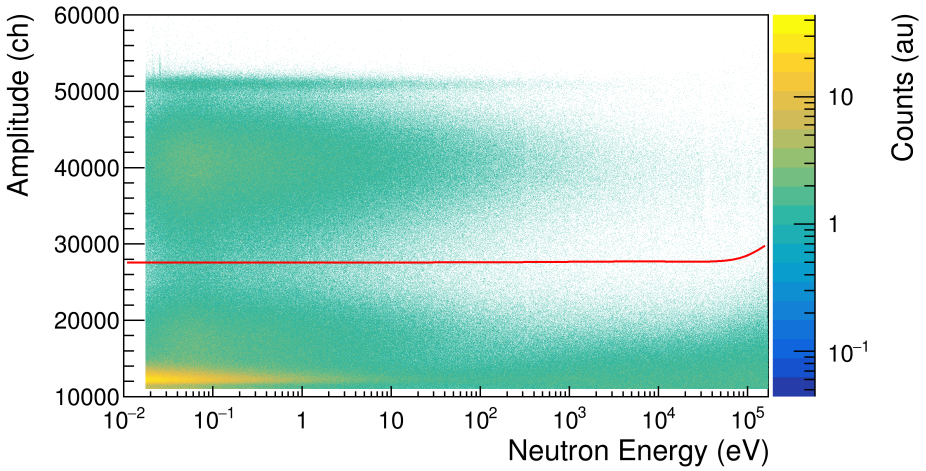

(b) B_b

Figure 3.9: Two-dimensional scatter plot of the deposited energy *versus* the incident neutron energy for the detectors coupled with boron carbide samples.

the incident neutron is negligible, because of the very high Q-value of the fission reaction, that is around 200 MeV, and of the low velocity acquired by the fissioning nucleus (1/236 of the incoming neutron). The

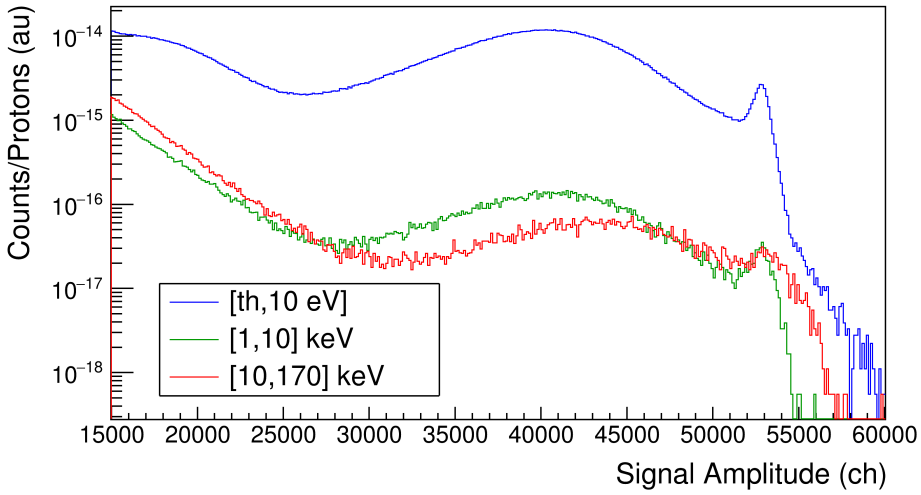

(a) B_f

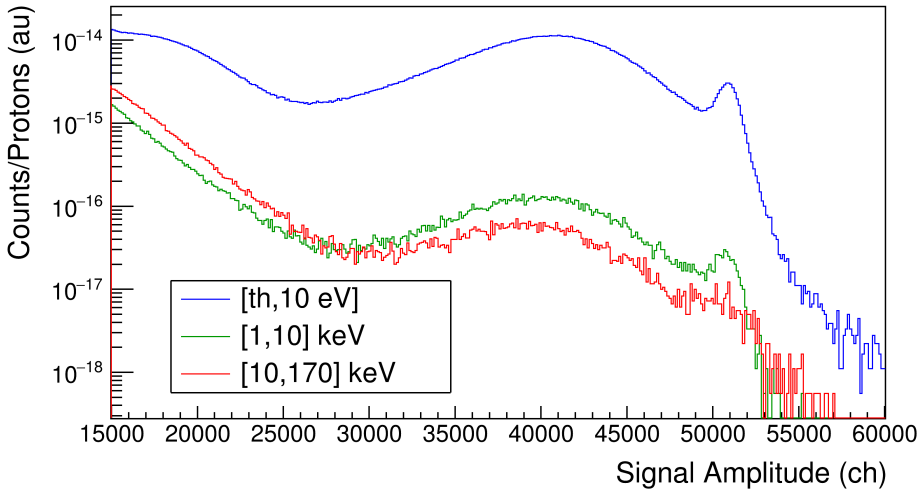

(b) B_b

Figure 3.10: Projection of the two-dimensional plots of figure 3.9 on the vertical axis for three neutron energy intervals of interest. Top: amplitude spectra for the detector in the forward direction, where the spectra move to higher values as increasing the neutron energy. Bottom: same figure for the backward detector, in this case the spectrum shifts to smaller values (see text).

two-dimensional scatter plots related to the uranium samples are shown in figure 3.11. The red line represents the experimental threshold used to separate the signals produced by the fission fragments from the background. In addition to the electronic noise, the main source of background comes from the alpha particles emitted by the spontaneous decay of the ^{235}U, with kinetic energy of 4.68 MeV. Due to the large Q-value of this reaction the fission fragments, with their kinetic energy of about 100 MeV, are well separated from the background as can be seen in the two plots. As expected, the number of detected alpha particles decreases with increasing neutron energy, because the time window corresponding to the neutron energy bin gets narrower.

The response of the preamplifier employed for the measurement has significantly conditioned the amplitude spectra, in particular for the two fission detectors. As said, in order to reduce the effects of the γ-flash during each beam bunch, we used the semi-logarithmic MESYTECH preamplifier. The high energy pulses produced in the silicon detector by the fragments were therefore compressed by the preamplifier. By looking at the plots one observes that starting from neutron energy of a few tens of keV the signal amplitude gradually decreases, a behavior due to the recovery time needed to recharge the preamplifier after the γ-flash, that reduces the effective gain of the preamplifier. Despite this gain loss, the separation between alpha and fission fragments was excellent over the full neutron energy range explored. The energy dependent selection threshold was defined accordingly.

Figure 3.12 shows the amplitude spectra by the U_f detector, integrated over different neutron energy intervals. The spectra have been roughly corrected for the gain loss of the preamplifier in the keV neutron energy, by using a polynomial function that compensates it. This function has been obtained by fitting the mode of the higher energy peak of the fission fragments. From the top panel can be observed the typical two-bump structure of bell-shaped curves corresponding to the fission fragments, despite the compression by the preamplifier. Moreover the quality of the discrimination between the alpha particles and the fission fragments results well evident. A threshold fixed at 10500 channel has been used in this detector, just over the alpha peak, in order to maximize the detection efficiency for the FF (Fission Fragments). To better esti-

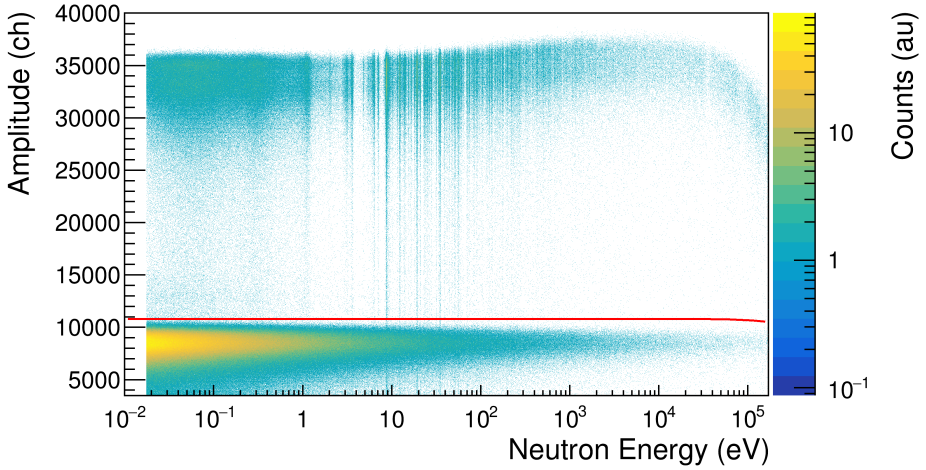

(a) U_f

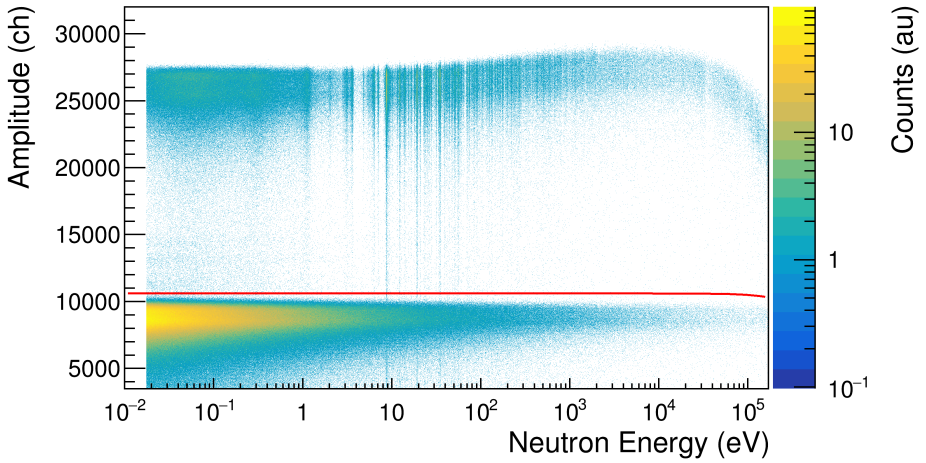

(b) U_b

Figure 3.11: Two-dimensional scatter plot of the deposited energy *versus* the incident neutron energy for the detectors coupled with the uranium hydroxide samples.

mate the fraction of lost FF due to the applied threshold, in the bottom panel the amplitude spectra normalized in the integral above the threshold (10500) are shown. This confirms that the low energy tail is the same

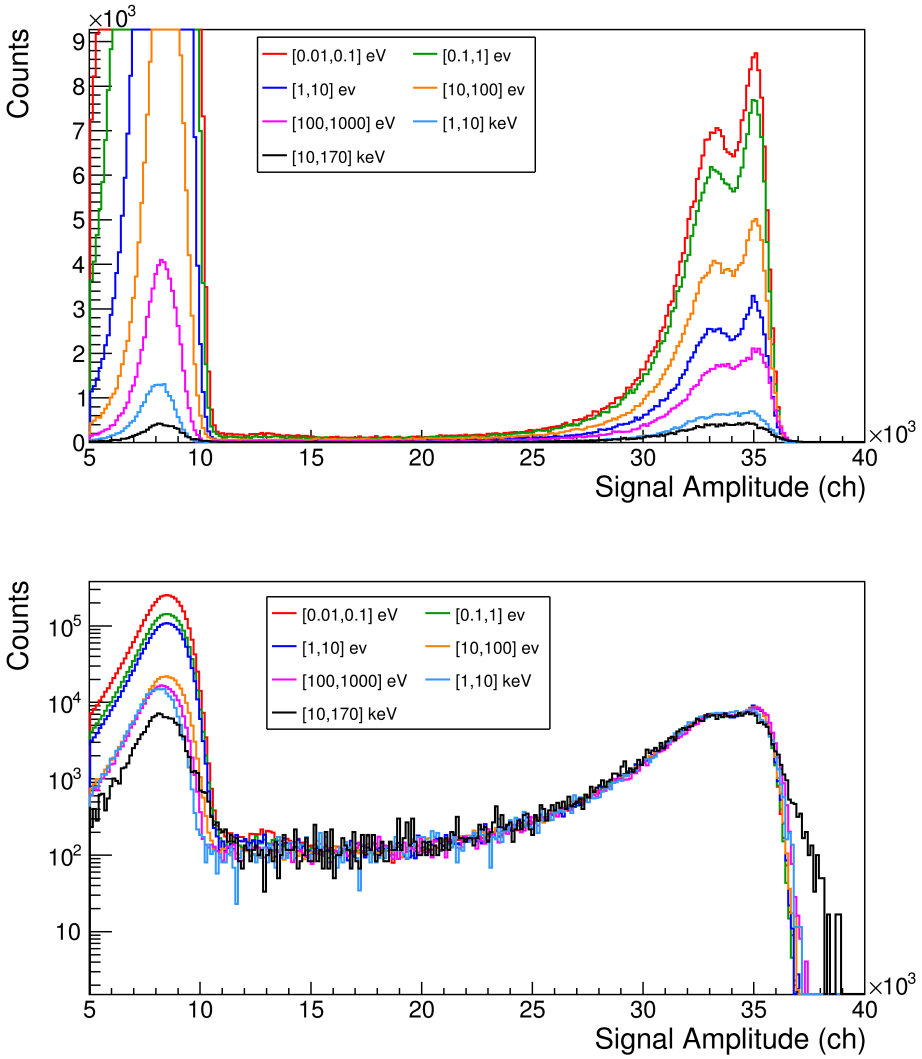

Figure 3.12: Top: Y-projection of figure 3.11a, for seven neutron energy intervals, after straightening the plot by means of a polynomial function. The two-bump structure of the bell-shaped curves confirms that these are fission events. Bottom: the same plot, after normalizing the curves to the same integral between 10500 (threshold) and 40000, in log-scale to prove that the fraction of fission fragments lost below the threshold is independent from the neutron energy.

independently of the neutron energy, thus implying that the fraction of fission events lost below the threshold is the same for all the neutron energies. Consequently the efficiency of the selection cut for fission fragments was evaluated as 0.9680(34).

3.4 Count rates

The counts as a function of the neutron energy in each silicon detector after applying the experimental threshold, are shown in figures 3.13, 3.14 and 3.15. In order to evaluate the different sources of background, two additional configurations were employed during the experimental session:

- **Sample BeamOn:** all the samples in place and neutron beam on.
- **Dummy BeamOn:** the samples were replaced with dummies, namely aluminum backing without the converter deposition, and neutron beam on.
- **Sample BeamOff:** all the samples in place and neutron beam off, with a dedicated trigger starting the data acquisition in replacement of the accelerator trigger.

The measurement of the background due to the neutron beam with the **Dummy BeamOn** configuration was particularly relevant for the detectors coupled with boron carbide samples, because of the lower S/N with respect to the other reactions. On the other hand, the **Sample BeamOff** configuration was required only for the detectors coupled to the uranium samples, because of the alpha radioactivity of ^{235}U of half-life 7.04 10^8 years. The Dummy BeamOn data shown in the following plots have been scaled to the Sample BeamOn, using the whole number of protons sent on the spallation target, while the Sample BeamOff data have been normalized to the Sample BeamOn by the number of triggers.

In figure 3.13 the total counts for the lithium fluoride samples are shown, where the extremely high signal to background ratio over all the neutron energy range is clearly visible. As expected, no counts were

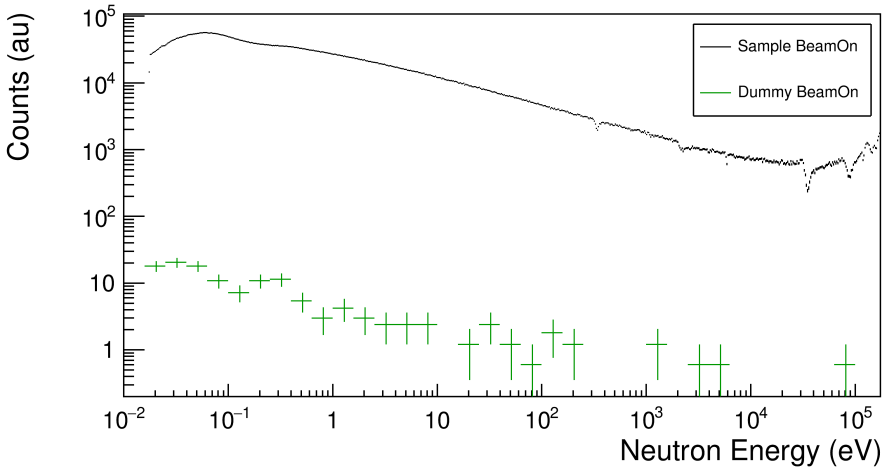

(a) Li_f

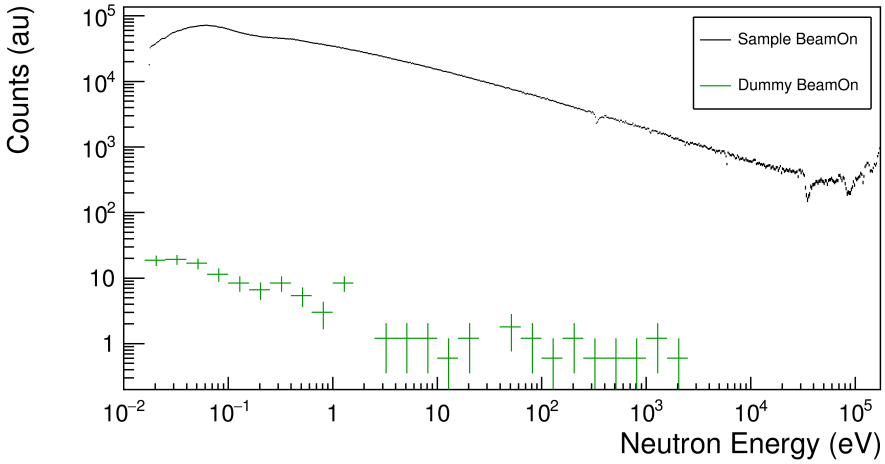

(b) Li_b

Figure 3.13: Experimental counts in the detectors coupled with lithium fluoride samples for the BeamOn (black) and Dummy (green) data acquisition.

registered in the detectors when the neutron beam was off and the corresponding spectra is not reported. The only source of background was due

to the neutron beam itself and was evaluated by means of the Dummy BeamOn configuration. In this case there were three orders of magnitude between the Sample and Dummy data.

The same plots for the detectors coupled with boron carbide samples are shown in figure 3.14. As expected the background induced by the neutron beam is more relevant compared to the lithium case, as can be seen from the comparison between the black and green points, in particular in the keV neutron energy region. The lower signal to background ratio arises partially from the smaller number of signals per neutron pulse, due to the much lower areal density of boron samples, and mainly from the relatively low experimental threshold applied to select the alpha particles due to the small Q-value, that introduces a significant amount of electronic noise especially in the keV energy region, where this component is large because of the proximity to the γ-flash. Comparing the Dummy BeamOn measured with Li and B detectors, the background measured with the B detectors resulted to be approximately a factor 3 larger as compared to the Li detectors.

Due to the natural radioactivity of the uranium hydroxide samples, the data measured with the BeamOff configuration were essential to evaluate the alpha background. The comparison of the total counts in these detectors with the Dummy and BeamOff configurations are shown in figure 3.15. The contributions of both background sources were comparable, two orders of magnitude lower than the Sample BeamOn data in the valleys between the resonances and much lower in the continuous. Moreover it is interesting to remark that the neutron beam background, was lower than 10 counts per bin at thermal, lower than lithium, where it was of the order of 20 counts per bin.

3.5 Detectors stability

The radiation resistance of the detectors was verified by calculating the ratios between the total counts in the first 10% and the last 10% of data for the U_f and U_b detectors, which were normalized to the number of protons on the spallation target and then shown in figure 3.16. In both cases the ratio fluctuates around unity, proving that after 4-weeks of mea-

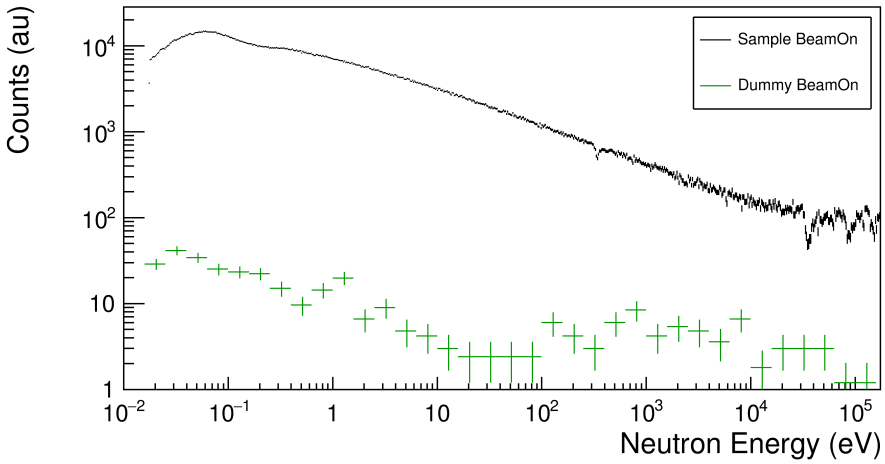

(a) B_f

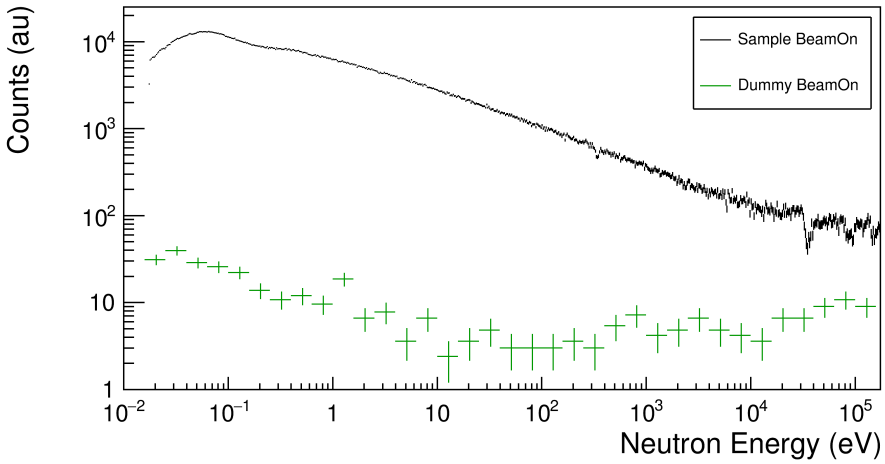

(b) B_b

Figure 3.14: Experimental counts in the detectors coupled with boron carbide samples for the BeamOn (black) and Dummy (green) data acquisition.

surement on the neutron beam the fission detectors did not suffer relevant radiation damage. The clear evidence of the detectors stability was of par-

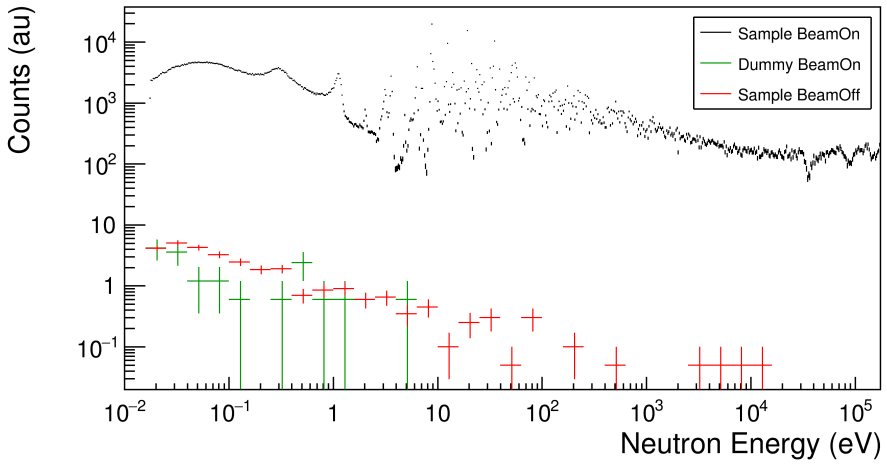

(a) U_f

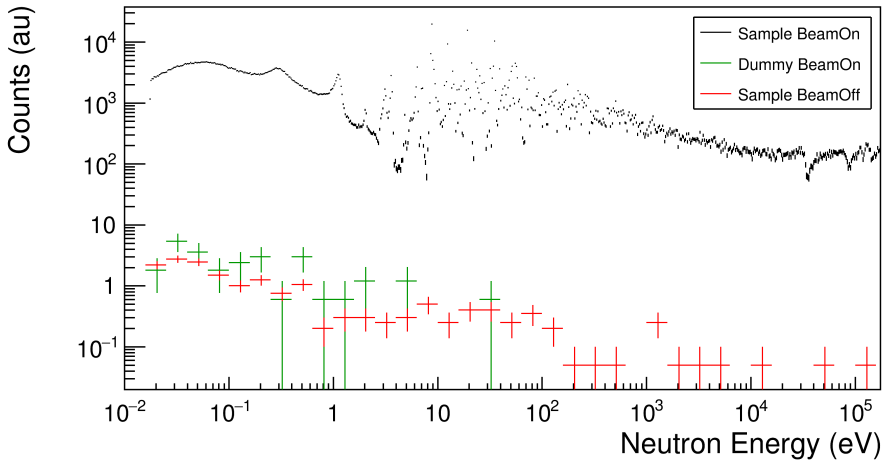

(b) U_b

Figure 3.15: Experimental counts in the detectors coupled with uranium hydroxide samples for the BeamOn (black), Dummy (green) and BeamOff (red) data acquisition.

ticular importance because this approach represents the first case where silicon detectors have been employed to measure fission cross section at

n_TOF. The demonstrated excellent performances in terms of stability and resolution, that ensure high quality data, opens the possibility of a more widespread use of silicon detector for other fission measurements at n_TOF.

3.6 Ratio method

The experimental setup has been conceived to measure the ^{235}U(n,f) cross section by using the so-called *Ratio Method*, where the two standard reactions ^{6}Li(n,t) and ^{10}B(n,α) have been used as reference. The formula used to obtain the ^{235}U(n,f) cross section is reported in 3.3, where the thin target approximation has been applied for the U and B detectors, while for the lithium expression $\rho_{ref} \cdot \sigma_{ref}(E_n)$ has been replaced with $(1 - e^{-\rho_{Li} \cdot \sigma_{Li}(E_n)})$. The suffix ^{235}U refers to the physical quantities related to the detectors coupled to the uranium hydroxide samples and ref indicates the detectors measuring a reference reaction:

$$\sigma_{^{235}U}(E_n) = \frac{C_{^{235}U}(E_n) f_{ref}(E_n) \rho_{ref} \varepsilon_{ref}(E_n)}{C_{ref}(E_n) f_{^{235}U}(E_n) \rho_{^{235}U} \varepsilon_{^{235}U}} \sigma_{ref}(E_n) \tag{3.3}$$

where C_X are the total counts after the background subtraction, ρ_X are the samples' areal densities, f_X are the absorption correction factors and ε_X are the detection efficiencies for the corresponding reactions. With the exception of ρ_X and $\varepsilon_{^{235}U}$, all these quantities are function of the neutron kinetic energy. Considering that all the detectors and the samples are stacked along the beam axis, the neutron flux on the uranium and reference samples is almost the same, so that with the applied *Ratio Method* the measurement is totally self-consistent, in the sense that no external neutron flux measurement is required, as shown in 3.3. To be pointed out that the detection efficiency of $\varepsilon_{^{235}U}$ is constant over the energy interval of interest, since the two fission fragments of ^{235}U(n,f) are emitted isotropically and the boost of kinetic energy due to the incident neutrons can be neglected. In order to reduce the systematic uncertainty, in our data analysis the physical quantities not depending on the neutron energy have been grouped and estimated thought the normalization procedure de-

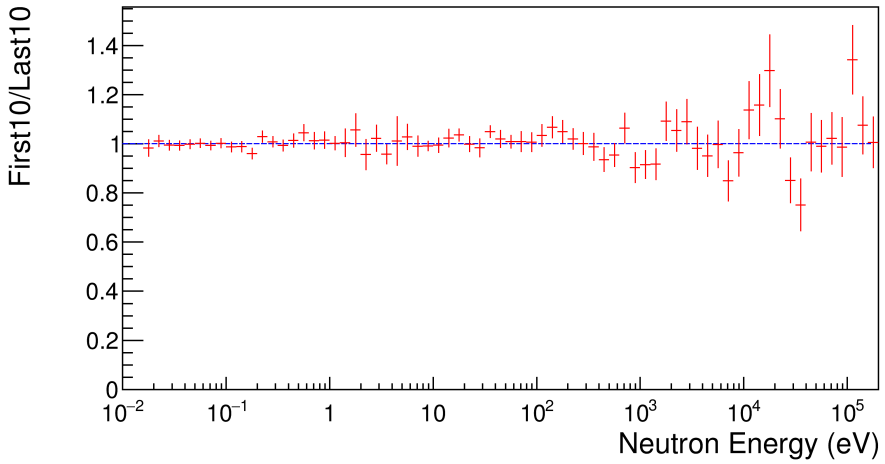

(a) U_f

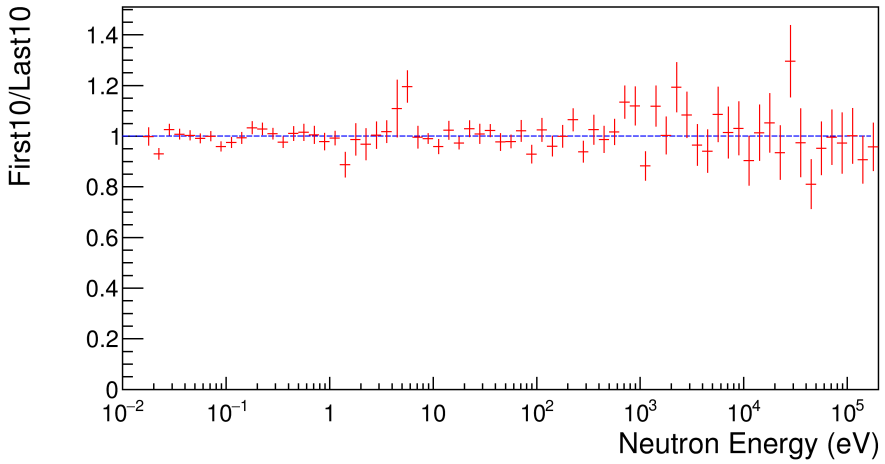

(b) U_b

Figure 3.16: Ratio between the total counts in the U_f and U_b detectors registered in the first 10% and the last 10% of data, after a proper normalization to the number of protons on the spallation target has been applied.

scribed in detail in section 3.8. The expression for the ^{235}U(n,f) becomes:

$$\sigma_{^{235}U} = K\frac{C_{^{235}U}(E_n)f_{ref}(E_n)\varepsilon_{ref}(E_n)}{C_{ref}(E_n)f_{^{235}U}(E_n)}(E_n)\sigma_{ref}(E_n) \tag{3.4}$$

where:

$$K = \frac{\rho_{ref}}{\rho_{^{235}U}\varepsilon_{^{235}U}} \tag{3.5}$$

The small differences in the neutron flux on each sample, related to the geometrical shape of the samples and to the absorption of the neutron beam in the various samples and detectors are taken into account with the correction factor f_{ref} and $f_{^{235}U}$. These corrections have been evaluated by means of a dedicated Monte Carlo simulation, that is described in detail in section 4.2. The Monte Carlo simulation employed for the evaluation of the correction factor has also been used to estimate the efficiencies as a function of the neutron energy, as described in detail in section 4.3.

3.7 Measured flux

The neutron beam in a time-of-flight facility is characterized by *fluence* (F_E) and *flux* ($\Phi(E_n)$) that are defined as:

$$F_E = \frac{dN_e}{dt \cdot da} \quad \text{and} \quad \Phi(E_n) = \frac{dN_e}{dt} \tag{3.6}$$

where dN_e indicated the density distribution of neutrons reaching the sample with energy between E_n and $E_n + dE_n$, dt the time element and da the cross-sectional area of a spherical element. However at n_TOF, given the pulsed time structure of the neutron beam, the term *flux* is (improperly but conveniently) used to indicate the time integrated *fluence*, namely the total number of neutrons for a proton pulse integrated over the whole beam spatial profile. During the measurement the two reference reactions have been used to measure independently the neutron flux incident on the experimental setup, and have been compared to the official n_TOF flux [1] in order to verify their mutual consistency. For

each reference reaction the neutron flux was obtained by the following expressions:

$$\begin{aligned}\Phi_B(E_n) &= \frac{C_B(E_n)}{f_B(E_n)\varepsilon_B(E_n)\rho_B\sigma_B(E_n)} \\ \Phi_{Li}(E_n) &= \frac{C_{Li}(E_n)}{f_{Li}(E_n)\varepsilon_{Li}(E_n)(1-e^{-\rho_{Li}\cdot\sigma_{Li}(E_n)})}\end{aligned} \tag{3.7}$$

where C_{ref} are the counts after the background subtraction, ρ_{ref} are the sample areal density, f_{ref} are the absorption correction factors, ε_{ref} are the detection efficiency for the corresponding reaction and σ_{ref} are the reaction cross section. In order to reduce the uncertainty arising from ρ_{ref}, it was estimated through the normalization of the flux measured with the four detectors in the energy interval between 1 and 100 eV. After the normalization the flux measured with each couple of detectors, namely Li_f & Li_b and B_f & B_b, was combined in a weighted average using the formula 3.8.

$$\Phi(E_n) = \frac{\frac{1}{\sigma_f^2(E_n)}\Phi_f(E_n) + \frac{1}{\sigma_b^2(E_n)}\Phi_b(E_n)}{\frac{1}{\sigma_f^2(E_n)} + \frac{1}{\sigma_b^2(E_n)}} \tag{3.8}$$

The fluxes measured with the reactions ^{6}Li(n,t) (red curve) and ^{10}B(n,α) (blue curve) are compared in the top panel of figure 3.17, in the same panel the χ^2 between the two curves is shown (filled green curve), with the Y-axis reported on the right, obtained with the expression:

$$\chi^2(E_n) = \frac{(\Phi_{Li}(E_n) - \Phi_B(E_n))^2}{\sigma_{Li}^2(E_n) + \sigma_B^2(E_n)} \tag{3.9}$$

It is important to highlight that all the statistical indicators confirm that the two versions of the flux are mutually consistent. As a matter of fact the reduced χ^2 value has values close to one, and the difference between the two curves in units of standard deviation, that it is shown in the middle panel, results below 3σ in the whole energy range. Finally, in the bottom panel where the ratio between the boron and lithium flux is shown, it can be noted that below 1 keV the ratio is well within 2%, while at higher

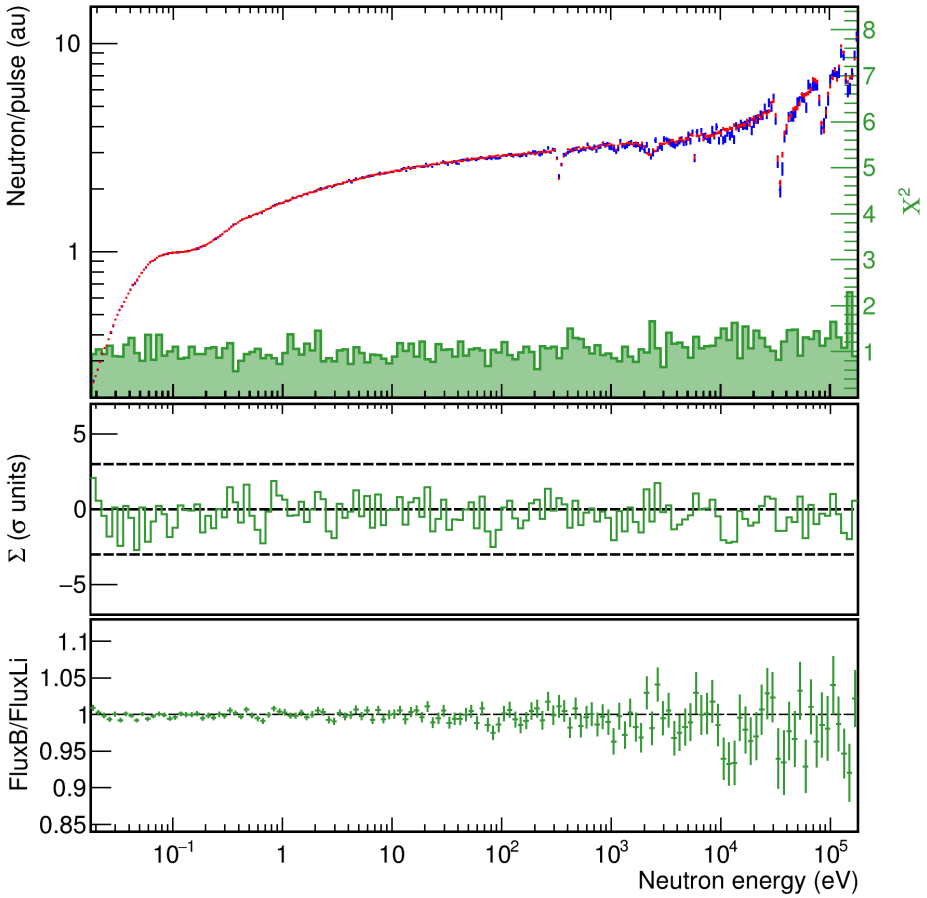

Figure 3.17: Top panel: flux measured with the reactions ^{6}Li(n,t) (red curve) and ^{10}B(n,α) (blue curve), and χ^2 between the two (filled green curve, right axis). Middle panel: deviation between the two curves in units of standard deviation. Bottom panel: ratio between the fluxes.

energies the lower statistic implies larger fluctuations, still compatible with unity anyway.

In figure 3.18 the comparison between the flux measured with the two reference reactions and the official n_TOF flux published on 2011 is shown. In the top panel the 2011 flux highlights a very good agreement with the new experimental data, with the exception of the low energy part. Such a difference is due to the changes during the years of the

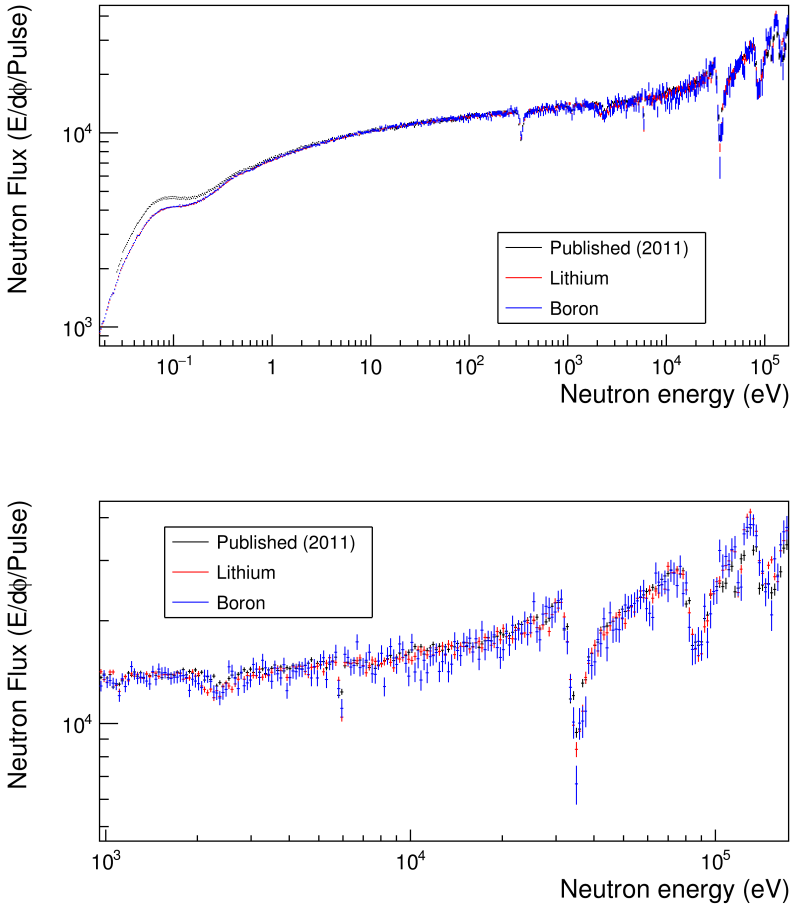

Figure 3.18: Top: flux measured with the two reference reactions compared with the official n_TOF flux. Bottom: detail of the flux above 1 keV.

boric acid (H_3BO_3) concentration in the target moderator, that produce significant differences in the low energy part of the spectra, because of the large cross section of the $^{10}B(n,\alpha)$ reaction in this energy range. In the bottom panel the flux for neutron energies above 1 keV shows in detail the presence of the absorption resonances. That confirms once again the consistency of the time to energy conversion and of the flight path evaluation. However, the choice of the *Ratio Method* based on the two reference

reactions prevented any possible source of systematic uncertainties arising from possible differences in the official flux.

3.8 Normalization

A crucial point of the analysis concerns the normalization of the ^{235}U(n,f) cross section with the standard values. The analysis method we adopted allowed to largely reduce the systematic uncertainty due to the physical quantities not depending on the neutron energy, grouping them in a single normalization constant that was calculated by normalizing the experimental data to the IAEA standard with the integral of the cross section between 7.8 and 11 eV. This was based on the recommendations in the latter paper dedicated to the evaluation of the neutron data standard [19].

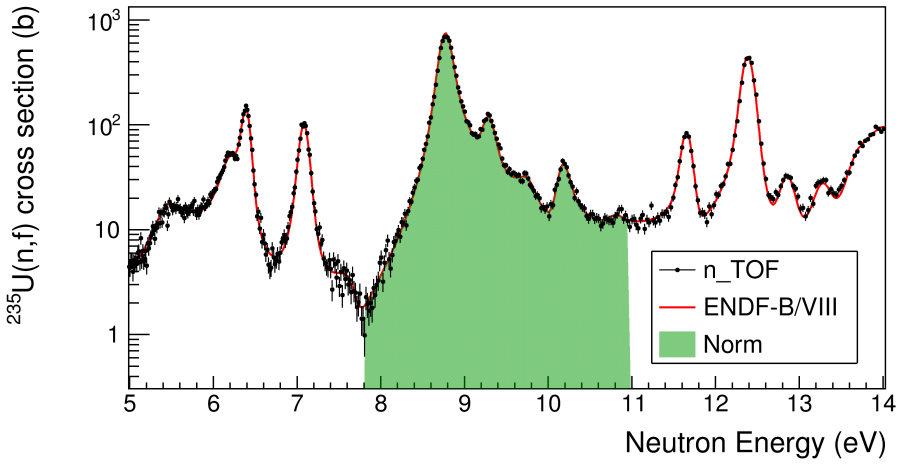

Figure 3.19: The green area represents the integral used to normalize the experimental data. The black points are the ^{235}U(n,f) cross section obtained with the weighted average of Li+B flux, while the red line is the ^{235}U(n,f) cross section provided by ENDF/B-VIII.

Moreover, this choice provides several advantages compared to the alternative normalization to the standard value at thermal energy. Firstly, an

integral value univocally defined is independent of the chosen data binning and no fitting procedure is needed; secondly, the integral limits are located in two cross section minima around a large resonance, meaning that any uncertainty arising from the time to energy calibration can be neglected. In addition, the large value implies a larger number of counts with respect to the thermal point, and therefore a much smaller statistical error. Finally, this procedure minimizes the source of uncertainty arising from the constant quantities, namely sample areal densities and detection efficiency of the ^{235}U(n,f) reaction. The integral used to normalize the experimental data is highlighted in figure 3.19 (green area), together with the ^{235}U(n,f) cross section obtained with the weighted average of Li+B flux and the evaluated cross section provided by ENDF/B-VIII.

Table 3.1: Comparison of the relevant standard values between IAEA and the present work computed using ^{6}Li and ^{10}B reference fluxes.

	Ratio σ (0.0253 eV) / Integral (σ) [7.8,11]eV [eV^{-}1]	**Integral (σ) [7.8,11]eV [eV^{-}1]**
IAEA	2.373 $\pm$ 0.029	247.5 $\pm$ 3
^{6}Li ref.	2.353 $\pm$ 0.013(stat) $\pm$ 0.007(syst)	249.6 $\pm$ 1.4(stat) $\pm$ 0.94(syst)
^{10}B ref.	2.343 $\pm$ 0.019(stat) $\pm$ 0.007(syst)	250.7 $\pm$ 2.0(stat) $\pm$ 0.95(syst)
^{6}Li + ^{10}B	2.352 $\pm$ 0.013(stat) $\pm$ 0.007(syst)	249.7 $\pm$ 1.4(stat) $\pm$ 0.94(syst)

The alternative option was the normalization of the experimental data at thermal neutron energy, where the ^{235}U fission cross section is defined as a neutron standard. In order to verify the consistency between the thermal point and integral value normalization procedures, we estimated the cross section value at thermal neutron energy by fitting the cross section data between 0.02 and 0.03 eV using a function having a $1/\sqrt{(Energy)}$ dependence. The cross section thermal value was then obtained through a linear interpolation at 0.0253 eV. In the first column of table 3.1 the ratio between the thermal value and the integral between 7.8 and 11 eV is reported; in the second column we listed the value of the same integral

that would be obtained in case the cross section was normalized at thermal point. The comparison of the experimental values obtained for these quantities with those provided by the IAEA [19] (first row) shows a good agreement for both reference reactions, separately and for the combination of the two by weighted average.

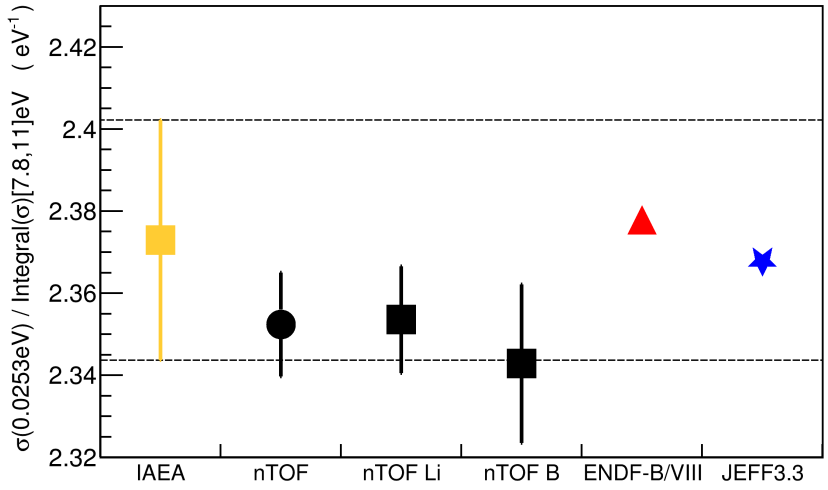

Figure 3.20: Ratio between the ^{235}U(n,f) cross section value at thermal and the integral between 7.8 and 11 eV, the error bar reports the statistic uncertainty for the experimental points.

In figure 3.20 the ratio σ (0.0253 eV) / Integral (σ) [7.8,11]eV [eV^{-}1] are shown, the black points are the experimental values obtained with the two references and the combination of the two, the yellow square is the value provided by the IAEA, the values obtained with the values by ENDF/B-VIII and JEFF3.3 are reported in red triangle and blue star respectively. The error bars report the statistical uncertainty for the experimental points, the weighted average between the two references is much closer to the lithium value because it has a larger yield compared to boron.

Chapter 4

Monte Carlo simulations

The *Ratio Method* adopted for the data analysis and described in section 3.6, required the evaluation of the quantities f_X and ε_{ref}, respectively the correction for the neutrons absorption by the detector components and the efficiency of Li and B detectors. Even if these corrections can be in principle calculated analytically, it would be rather difficult and would require approximations affecting the global uncertainty. A more effective and accurate evaluation of those quantities has been achieved throught Monte Carlo simulations by using the Geant4 code [106], that allowed the simulation and the complete characterization of the experimental setup. Despite being developed for the field of high energy physic, the use of the Geant4 (release 10.0.4) code has already proved to be suitable to cope with neutron induced reactions at n_TOF [107]. The full experimental setup of the measurement has been implemented, with particular care to quantify correctly the attenuation effects on the neutron beam, due to all the detector components (named *volumes* in the MC code) crossed by the neutrons, namely the samples with their respective backing and the silicon detectors. In section 4.1 the main features of the Monte Carlo simulation are described, while the analysis of the simulation results relatively to the neutron beam absorption and detectors efficiency are discussed, respectively in section 4.2 and 4.3.

4.1 Simulation features

Figure 4.1 shows the experimental setup consisting of six detectors and six samples deposited on aluminum backing of different thickness, which has been implemented in the Geant4 simulation code. The aluminum case made of three blocks, one bottom and two on both the sides of the detector, is kept nearly transparent in the figure. Each of the six silicon detectors is represented in yellow and is placed in front of the respective sample: the LiF is in red, B_4C in blue and H_2O_2U in green. Of course the simulated setup is totally realistic and any detail reflects the property of each component. Also the aluminum dead layer on the surface of the detectors has been included, according to the description provided by detector datasheet. Its thickness is 500 nm and provides a significant contribution to determine the shape of the energy spectra, in particular for the low energy alpha particles with E < 2MeV.

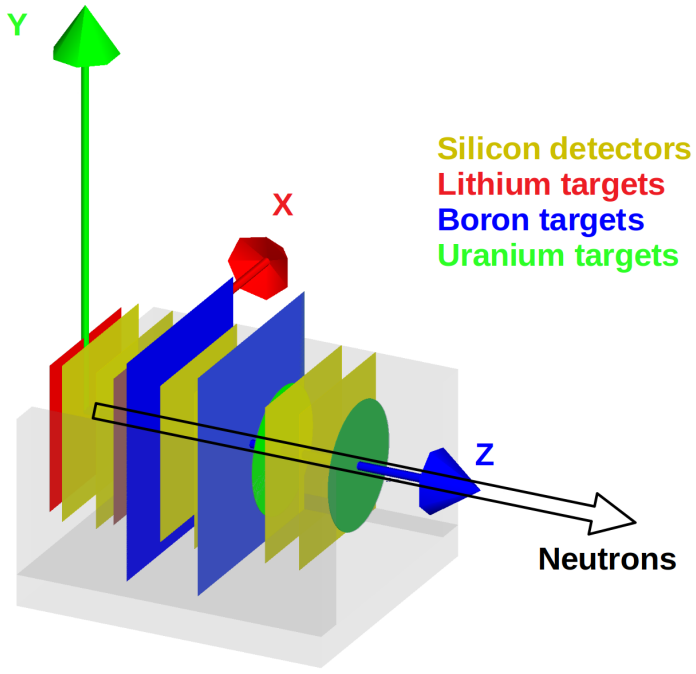

Figure 4.1: Simulated experimental setup. Silicon detectors are in yellow, samples are the red (lithium), blue (boron) and green (uranium) volumes.

Considering the three axis in the figure 4.1, the first volume encountered by the neutron beam (the backing of the first lithium sample) is placed with its rear surface lying on the XY plane with Z = 0. All the volumes of the detector are centered on the Z axis, that corresponds to the direction of the beam. The neutron beam properties, *i.e.* the shape, size and position on the samples and silicon detectors, have to be well known in order to perform a reliable and realistic simulation. We made use of the realistic n_TOF beam, measured during the n_TOF-Phase1 [108] and later confirmed during n_TOF-Phase2 [109]. Depending on the collimator used for the measurement, the shape is characterized by a Gaussian profile with sigma 0.7 cm. In figure 4.2 the XY simulated neutron beam profile centered on the first LiF sample is shown.

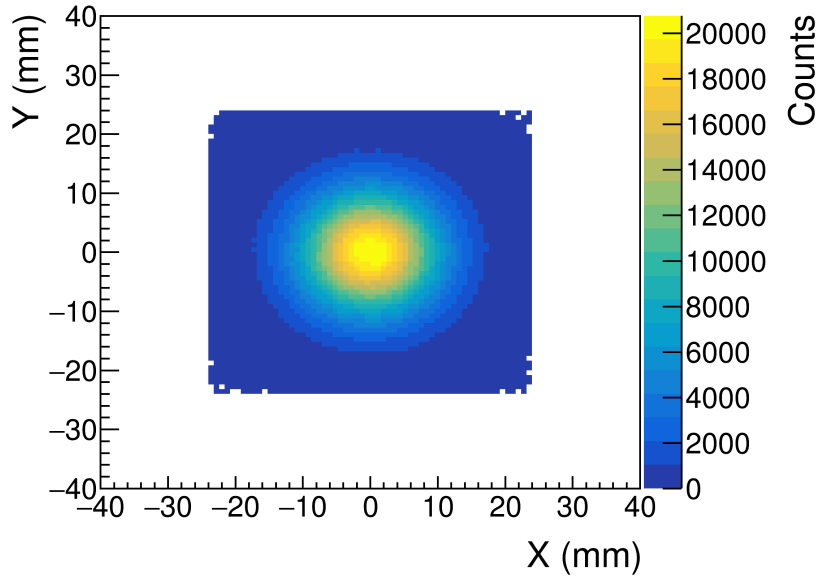

Figure 4.2: Beam profile of neutrons in the first lithium sample. It is clearly visible the adopted Gaussian distribution of neutrons on the perpendicular plane and the sample dimensions (47x47 mm^2).

Whilst the approach consisting on the use of the neutron beam interacting with the detector is well suitable to calculate the absorption correction factor, it can not be applied to calculate the detector efficiency.

In fact the combination of the neutrons transport code, which is very costly in terms of machine time, and the relatively small cross sections of all the interactions, make the simulations too long in time to accumulate the needed statistic. This is in particular relevant for Boron samples, which have a small reaction yield due to their small thickness, for which it would need several weeks to register some hundred reactions in the corresponding detectors. In order to significantly reduce the computational time to just a few minutes, but maintaining a high accuracy at the same time, we had chosen to directly generate the reaction products in the volumes corresponding to each sample. The beam properties, the angular distribution of the products and the kinematics of each reaction, have been implemented in the simulation code, in order to reproduce as best as possible the neutron interactions with all the samples.

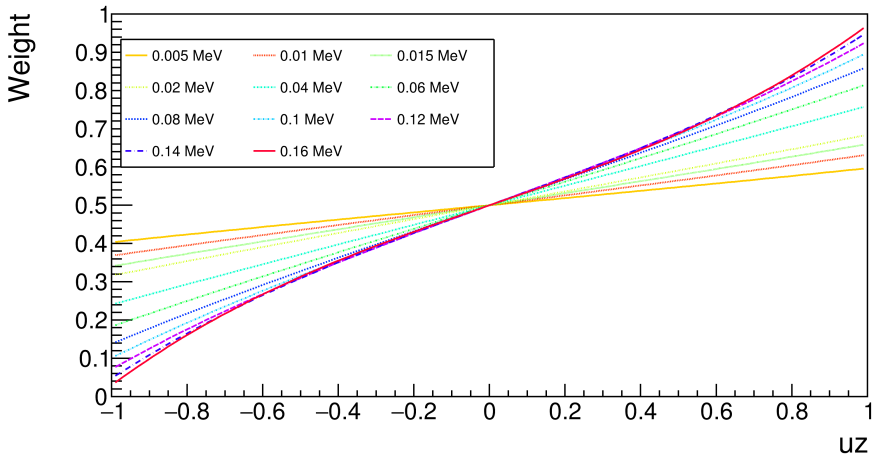

Figure 4.3: Angular distribution of tritons in the center of mass for the reaction ^{6}Li(n,t), obtained with the ENDF/B-VIII Legendre coefficients.

The angular distributions of the reaction products have been deduced by the coefficients of the Legendre polynomials provided by ENDF/B-VIII. In figure 4.3 the probability density function of the angular distribution in the center of mass as a function of the Z director cosine for the reaction ^{6}Li(n,t) is shown, calculated at different kinetic energies of the incident neutrons. In this case the angular distribution above a few

keV results to be strongly asymmetric, with the forward direction clearly predominant. Nevertheless the uncertainty arising from these distributions resulted to be relatively small, due to the large angular acceptance of the experimental setup and to the detection efficiency of the reaction products in the forward and backward directions.

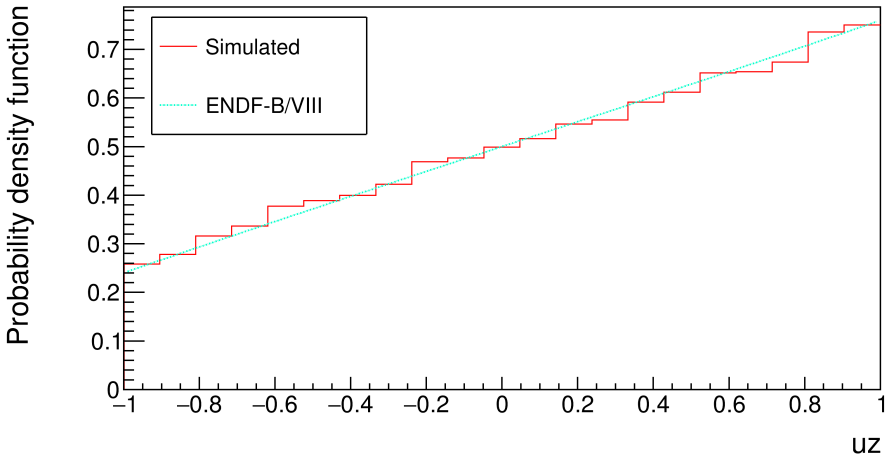

Figure 4.4: Comparison between the angular distribution in the direction of the neutron beam provided by ENDF/B-VIII and the simulated tritons of the reaction ^{6}Li(n,t), at 40 keV neutron energy.

Special care has been addressed to the validation of the simulation while writing the Geant4 code, in particular for the angular distribution of the reaction products. Just as an example, in figure 4.4 the simulated distribution in the center of mass of the tritons Z-cosine at 40 keV neutron energy is shown, compared to the ENDF/B-VIII distribution used as input for the simulation. As one can expect the two curves agree within the small statistical fluctuations, and the same check has been made for all the reactions and at different neutron energies, thus allowing the code to be continuously verified and validated. In addition, figure 4.5 shows the distribution of the direction cosines along the neutron beam for the tritons leaving the first Li sample and at different neutron energy. The events are registered when the triton move from the sample to vacuum, hence only in the forward direction, since in the backward the aluminum

backing is present. As expected, for low energy neutrons the distribution is flat, while at 40 keV the tritons are focused in the forward direction.

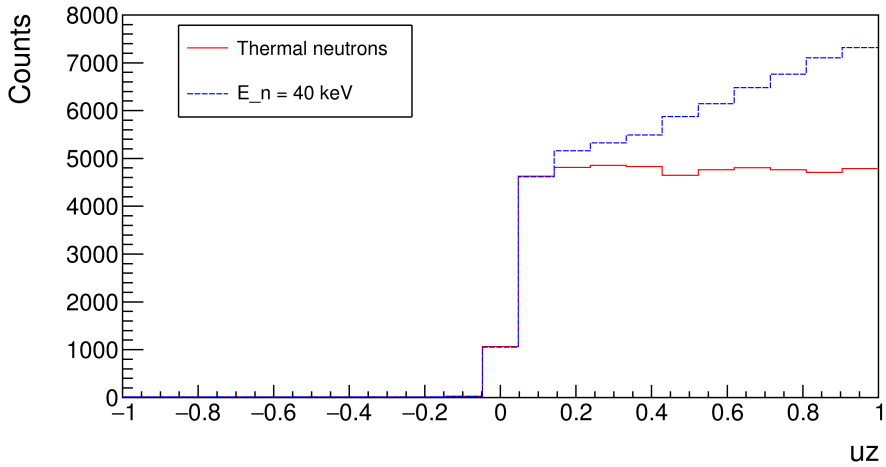

Figure 4.5: Simulated distribution of the direction cosines, along the neutron beam direction, for the tritons moving from the first Li sample to the vacuum, in the case of low energy neutrons and at 40 keV.

In addition to the angular distribution in the center of mass, also the kinematic effects arising from the incident neutron energy are considered, in order to define the initial energy of the particles and their emission direction. It is interesting to compare the resulting simulated spectra of the energy deposited in the detectors, in the case of forward and backward detectors. In figure 4.6 the simulated spectra of the energy released in the detectors coupled with the lithium sample are reported. At this stage the detectors resolution has not been taken into account yet. The blue curve is obtained at thermal neutron energy, in which the reaction products are emitted isotropically, therefore there is no difference between forward and backward detectors. The red curve represents the spectrum in the forward detector for neutrons at 40 keV, with a significant shift at higher energy due both to the neutron kinetic energy and to the larger fraction of tritons emitted at small angles, that means in average a shorter path into the crossed dead layer. In the backward direction, for neutrons at 40 keV the green curve shows a shift towards lower energies, where the

energy loss in the dead layer is increased because of the wider angular distribution of the backward emission. Due to the higher energy loss in the dead layer of alpha particles, that are mostly emitted at wider angles, the separation with respect to the tritons is increased, as can be seen in the spectrum. Figure 4.7 shows the same plot referred to the ^{10}B(n,α) reaction.

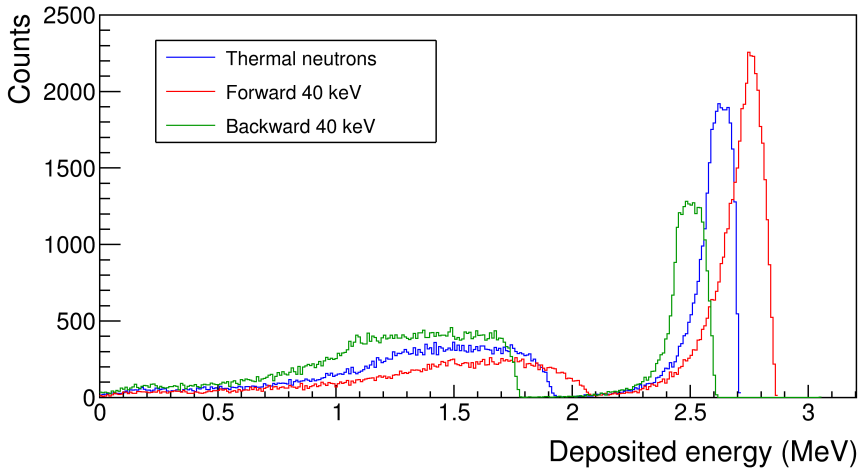

Figure 4.6: Spectra of the deposited energy in the corresponding detector for ^{6}Li(n,t) reaction at thermal (blue line) and at 40 keV of neutron energy in the forward (red) and backward (green) direction.

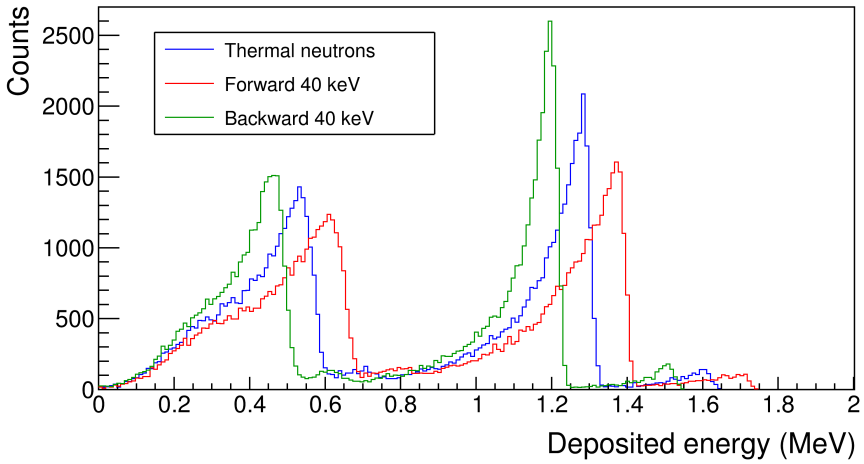

Figure 4.7: Spectra of the deposited energy in the corresponding detector for ^{10}B(n,α) reaction at thermal (blue line) and at 40 keV of neutron energy in the forward (red) and backward (green) direction.

4.2 Absorption correction

According to the *Ratio Method* described in section 3.6, the ^{235}U(n,f) is measured relative to the two references, assuming all the samples are crossed by the same neutron beam. Because the experimental setup has been placed on the beam, the neutron flux undergoes attenuation while crossing each volume along its path, and a correction for the neutrons lost is therefore needed. The energy distribution of the neutrons interacting with the i-th sample is extracted starting from the entering neutron flux and correcting it by the attenuation in all the layers before the sample itself. To calculate the correction factor relative to each sample, a dedicated simulation has therefore been performed. The neutron beam has been simulated as mentioned before, that is a Gaussian shape of σ = 0.7 cm and coaxial to the experimental setup. Since during the analysis the logarithmic binning was used for the neutron energy spectra, the simulated energy spectra of the neutron flux was chosen to be flat in logarithmic scale in the range 0.01 eV to 1 MeV, thus to accumulate statistics evenly over the full energy interval of interest.

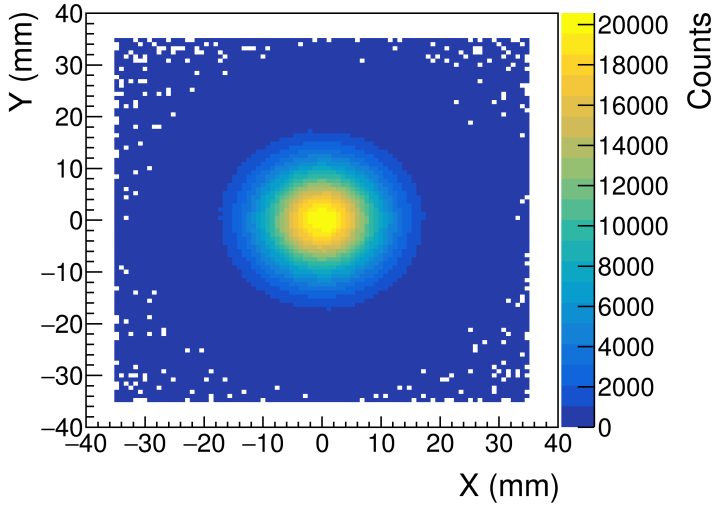

Figure 4.8: Neutron beam profiles in the plane of the first boron sample (square 70x70mm^2).

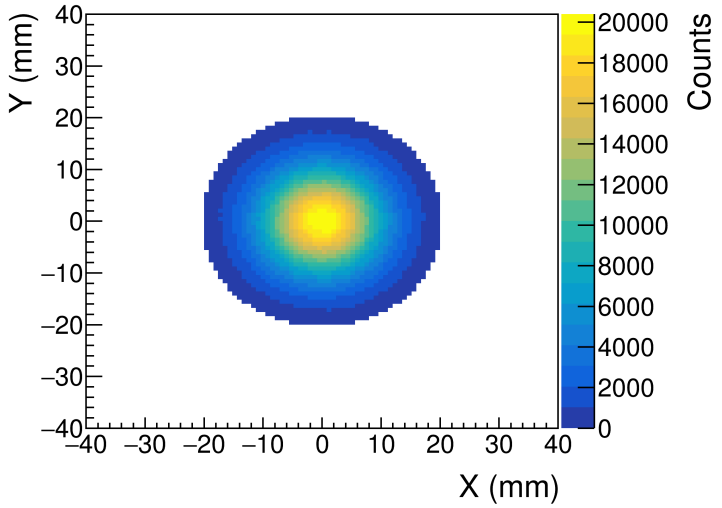

Figure 4.9: Neutron beam profiles in the plane of the first uranium sample (circle 40 mm diameter).

In figures 4.8 and 4.9 the beam profiles onto the boron and uranium samples are shown. Similarly to what has been said for figure 4.2, the shape of the boron and uranium samples, respectively a square 70x70 mm and a circle with 40 mm diameter, can clearly be distinguished. For each of the six samples, the Monte Carlo simulation code records the position and the kinetic energy of the impinging neutrons.

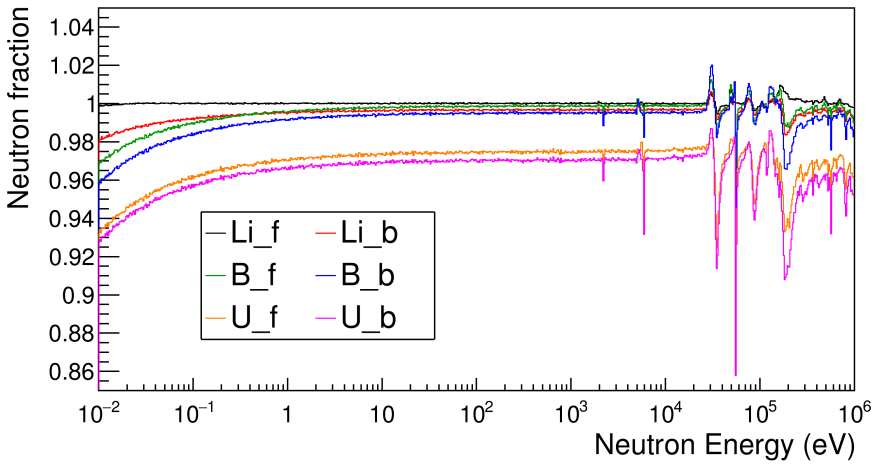

Figure 4.10: Correction factor as a function of neutron energy for the six samples.

The correction factor is calculated as the ratio between the energy spectra of the neutrons hitting the i-th sample and the flat energy distribution of the generated neutrons. In case of no attenuation this factor would 1 in the whole energy range. In realistic conditions the layers crossed before the i-th sample absorb or scatter a certain amount of neutrons, presenting characteristic dips at the resonance energies. The resulting correction factors for all the samples are shown in figure 4.10. It is worth observing that the main effects are present for low energy neutrons, mainly because of the typical 1/v trend of the ^{6}Li(n,t), ^{10}B(n,α) and ^{235}U(n,f) cross sections. Moreover the signature of aluminum capture resonances is clearly visible at higher neutron energies, starting from the first narrow resonance located at 5.9 keV. All the sample backings are made of aluminum and the correction is particularly significant for the

uranium samples, since the corresponding backing thicknesses are larger compared to those of lithium and boron (250 μm *versus* 50 μm and 18 μm respectively). Moreover, the smaller size of the uranium sample determines a small but constant correction independent of the neutron energy, due to the neutrons in the Gaussian tails that do not intercept the sample. The neutron beam profile along the horizontal axis is reported in figure 4.11 for the first (lithium, red line) and last sample (uranium, blue line). As expected, the Gaussian shape does not change, being the neutrons loss independent from the horizontal position in the samples before the uranium.

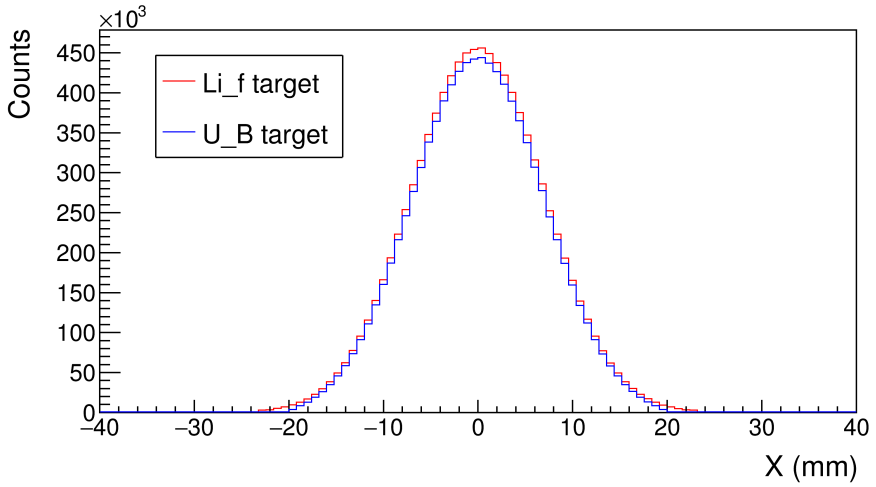

Figure 4.11: Profile on the horizontal axis of the neutrons hitting the first (lithium, red line) and last (uranium, blue line) sample.

4.3 Efficiency

As illustrated in the section 3.6, the number of events registered in each detector has to be corrected for the detection efficiency. This parameter is defined as the fraction of reaction products that reach the detectors and overcome the experimental thresholds, described in detail in section 3.3. For the Li and B detectors this quantity is not a constant value, since it

depends on the kinetic energy of the incident neutron starting from a few keV. A dedicated Monte Carlo simulation has been performed to evaluate the detection efficiency of Li and B detectors as a function of the incident neutron energy, while it was not needed for the U detectors, since their efficiency is constant over all the neutron energy range of interest. For each sample of Li and B, 10^5 reactions have been simulated for each neutron energy value that has been chosen. As said the coefficients of the Legendre polynomials provided by ENDF/B-VIII have been used to determine the angular emission of the products and a correction for the boost provided by the incident neutron has been also implemented. For each simulation the energy deposited into the each silicon detector has been recorded, as well as all the particle cosine and initial position, which were required to validate the code. In order to compare the simulated spectra with the experimental ones the experimental thresholds and the detectors resolution have been implemented in the MC code, the simulated spectra had to be convoluted with a Gaussian response, thus to reproduce the detector resolution.

The simulated spectra have been calibrated from energy to channel, since the thresholds were initially defined in units of *DAQ channels* in the experimental spectra. The conversion from *MeV* to *DAQ channels* accords to a linear calibration function, typical of silicon detectors, with two free parameters:

$$channel = p_1 * energy(MeV) + p_0 \tag{4.1}$$

the convolution with a Gaussian curve, to include the detector resolution, employed a standard deviation sigma depending on the deposited energy as:

$$\sigma = p_2 / \sqrt{Energy[MeV]} \tag{4.2}$$

The three parameters were optimized in order to minimize the χ^2 between the experimental data and the Monte Carlo spectra for low energy neutrons, where the experimental spectra have more statistics, thus optimizing the mutual agreement.

Figure 4.12 reports the comparison between Monte Carlo and experimental spectra of the Li detectors for very low energy neutrons. The black

line represents the experimental spectra measured for neutron energy below 1 eV, for which the angular emission of products can be considered completely isotropic. The red line is the deposited energy simulated by the Monte Carlo code for low energy neutrons with applied the Gaussian convolution. The dashed blue vertical line represents the experimental threshold used to select the tritons, while the yellow shaded region is the amplitude interval where the χ^2 between the experimental data and the simulation has been minimized. The Monte Carlo spectra have been normalized to the experimental data in the region above the experimental threshold.

For the Li_b detector the curves show a nice agreement even outside the mentioned interval, proving that the chosen calibration and experimental resolution are reasonable. Small discrepancies can be ascribed to minor differences due to a possible inhomogeneity in the thickness of the aluminum dead layer, that unfortunately is not specified on the detector datasheet and cannot be included in the code. Anyway the achieved agreement is more than sufficient for an accurate efficiency evaluation. This is not true for the Li_f detector: indeed it has already been pointed out in section 3.3 that it did not show the usual linear behaviour of silicon detectors. In this case the alpha particles peak resulted closer than expected to the tritons peak. Moreover, the shape of this alpha peak is anomalous, probably to be ascribed to a problem in the detector bias voltage or to an anomalous behaviour of the preamplifier. However, in light of the good agreement with the tritons peak we decided to employ a higher experimental threshold in order to to exclude most of the alphas while selecting the majority of triton events.

In the case of B detectors (figure 4.13), the comparison shows an excellent agreement in the region of interest between Monte Carlo simulations and the experimental data. Unfortunately the function adopted to describe the detector resolution cannot reproduce the higher energy peak due to alphas emitted with ^{7}Li in the ground state: indeed such a peak is too narrow because compressed by the set-in of the logarithmic behaviour of the preamplifier. In any case this does not represent an issue, because no events related to this peak are lost.

In principle, the parameters fitted at low neutron energies are valid over the entire energy range of interest, till to 170 keV. In figure 4.14

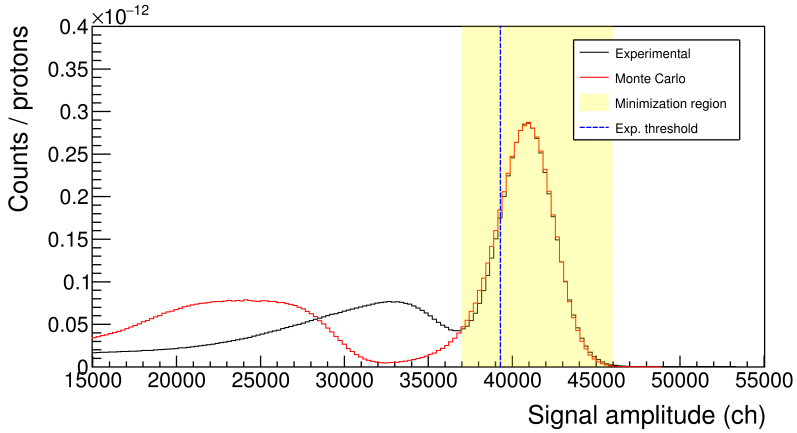

(a) Li_f

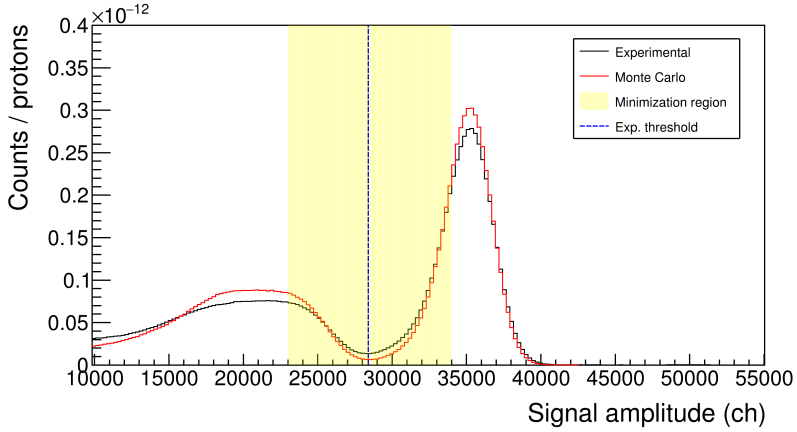

(b) Li_b

Figure 4.12: Comparison between Monte Carlo and experimental spectra of the deposited energy for low energy neutrons (< 1 eV) in Lithium detectors.

and 4.15 the comparison between experimental data and the simulated spectra for neutrons at 40 keV are reported. In particular the experimental spectra were obtained by selecting the events between 35 keV and 45 keV. Due to the 1/v behaviour of the cross sections, the total counts in the experimental spectra strongly decrease at higher neutron energy and

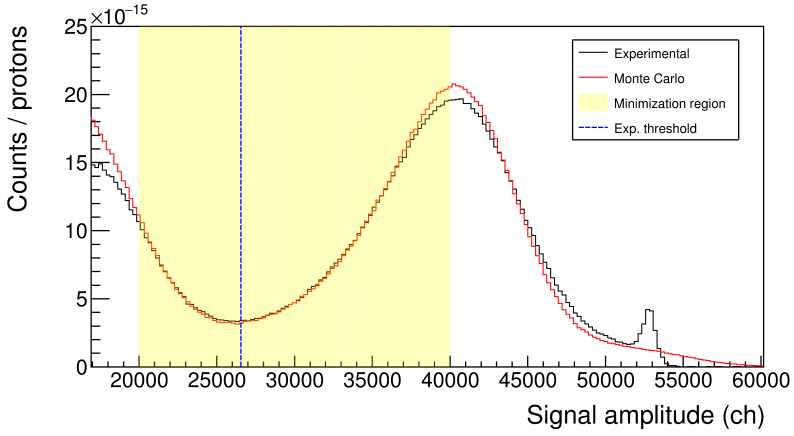

(a) B_f

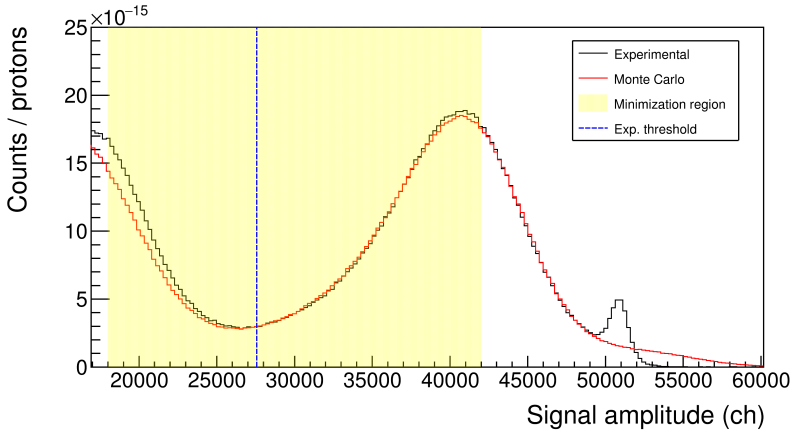

(b) B_b

Figure 4.13: Comparison between Monte Carlo and experimental spectra of the deposited energy for low energy neutrons (< 1 eV) in Boron detectors.

therefore present significant fluctuations. This effect is more important for the ^{10}B(n,α) reaction, while in the case of the ^{6}Li(n,t) reaction it is partially mitigated by the resonance located at 250 keV. Similarly to what showed for low neutron energy, the alpha peak shape in the Li_f detector is not well reproduced, while a reasonable agreement is found for the

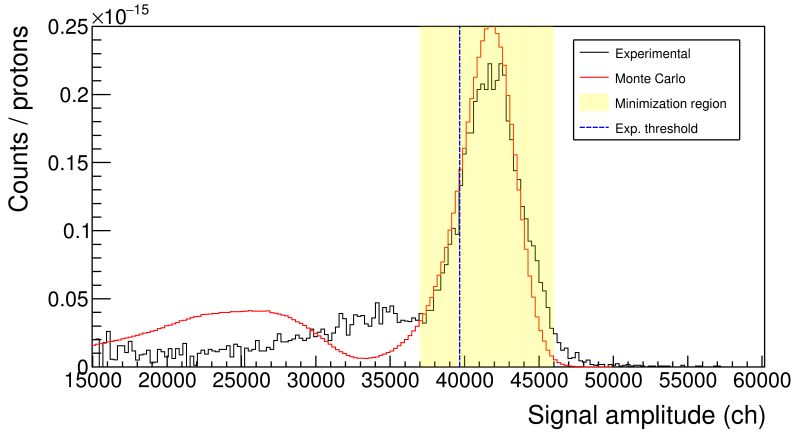

(a) Li_f

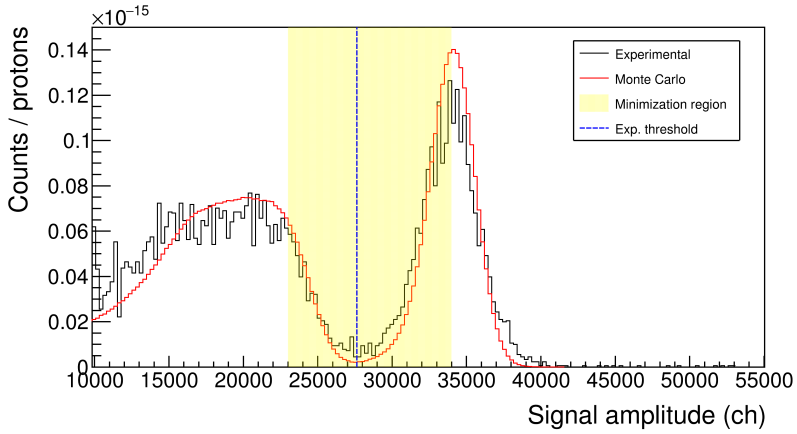

(b) Li_b

Figure 4.14: Comparison between Monte Carlo and experimental spectra of the deposited energy for 40 keV neutrons in Lithium detectors.

tritons. Once again, the agreement for the Li_b detector is excellent.

The comparison for the B detectors is reported in figure 4.15, where it is evident that the adopted resolution is not again suitable to reproduce the high energy peak. In any case the discrepancies are under control and the agreement remains good by increasing the neutron energy, proving that the correction for the angular distribution and kinetic energy

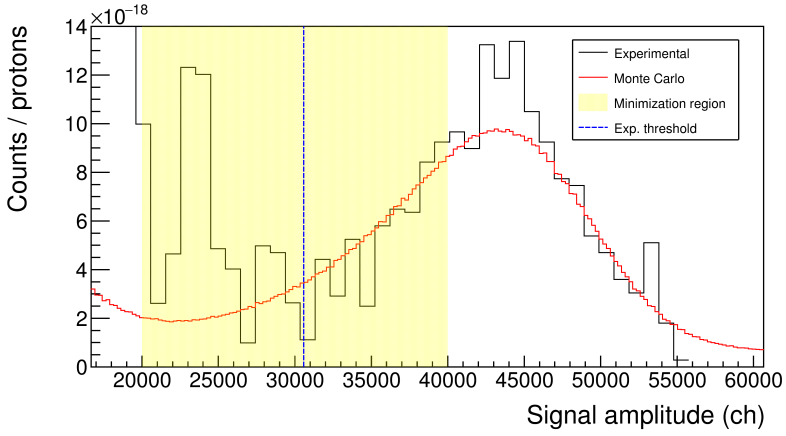

(a) B_f

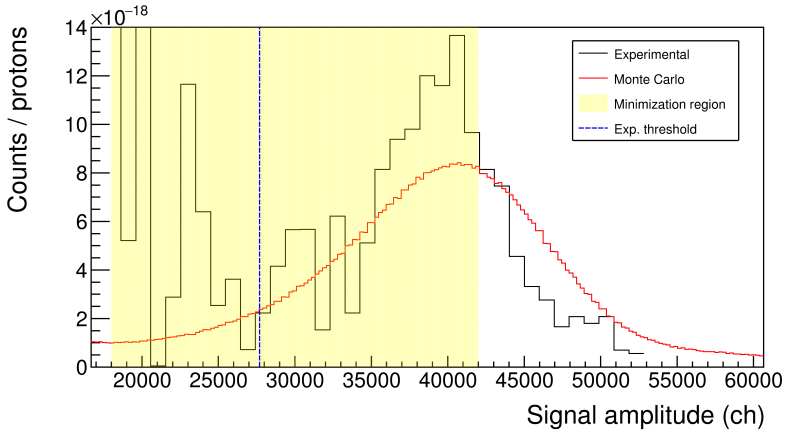

(b) B_b

Figure 4.15: Comparison between Monte Carlo and experimental spectra of the deposited energy for 40 keV neutrons in Boron detectors.

was quite reasonable. For each Li and B detector the point-wise value of the efficiency has been evaluated for 11 neutron energies, in order to study its energy dependence. The energy values are: 10^{-4}, 5, 10, 15, 20, 40, 60, 80, 100, 120, 140, 160 keV. The first point refers to the efficiency for low energy neutrons, for which the angular emission of the reaction products is isotropic. The remaining energy values are those for which

the ENDF/B-VIII library provides the Legendre coefficients within the energy interval of interest for the measurement, *i.e.* below 170 keV, and it was hence possible to determine the angular distribution of the products. For each simulation the resulting spectra have been converted from *MeV* to *DAQ channels* and convoluted with the resolution previously determined. Therefore the point-wise value of the efficiency is given by the ratio between the events that overcome the threshold and the 10^5 reactions that have been simulated. The obtained values were fitted with a 3-th degree polynomial and the resulting efficiency is reported in figures 4.16 and 4.17.

It is clear that the neutron dependence is more relevant for the ^{6}Li(n,t) reaction, because of the pronounced anisotropy of the angular distribution of the reaction products in the keV region. The low efficiency for the forward detector at low energies, compared to the backward detector, is due to the high experimental threshold used to separate alphas and tritons, that as said partially exclude the lower energy tail of the triton peak. Nevertheless the strong forward emission of tritons in the reaction leads to an increasing efficiency in the keV energy region, efficiency that reaches 45% at 100 keV. The backward detector presents an efficiency around 38% at low energies, a reasonable value considering that the alpha/tritons discrimination is quite good but its effective angular coverage in the laboratory reference frame is decreased by the kinematic boost. Therefore, the efficiency decreases and reaches a minimum value of 21% at 100 keV.

The anisotropic emission of ^{10}B(n,α) reaction is less evident, and produces a smaller energy dependence of the efficiency. Nevertheless a small increase for the forward detector, and a complementary decrease for the backward one, can be observed for neutron energy larger than 1 keV. It is interesting to notice that at low energy the detectors have a similar efficiency around 33%, as expected considering the isotropic emission of the products and the equivalent experimental thresholds. The lower value with respect to the Li_b detector is related to the lower energy of the alpha particles, whose angular acceptance is significantly affected by the dead layer of the silicon detectors.

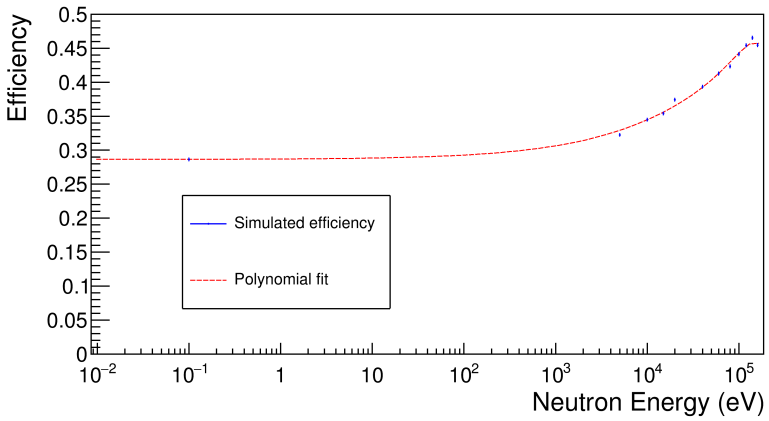

(a) Li_f

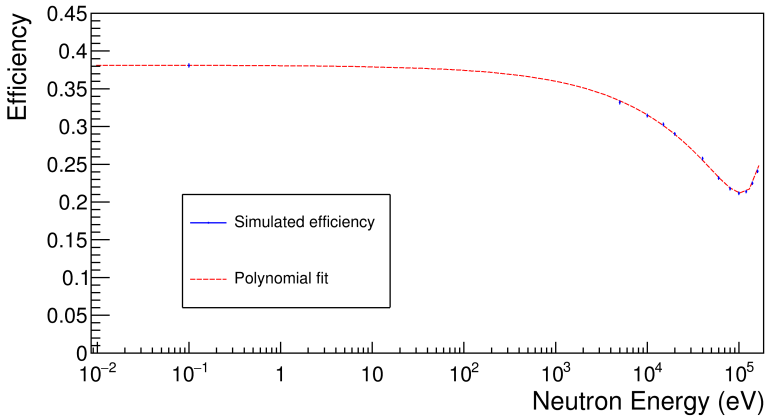

(b) Li_b

Figure 4.16: Detector point-wise efficiency for the Lithium detectors, and polynomial fit.

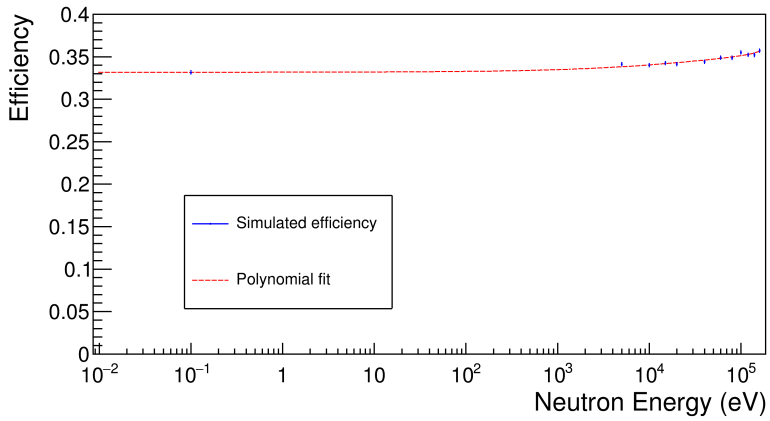

(a) B_f

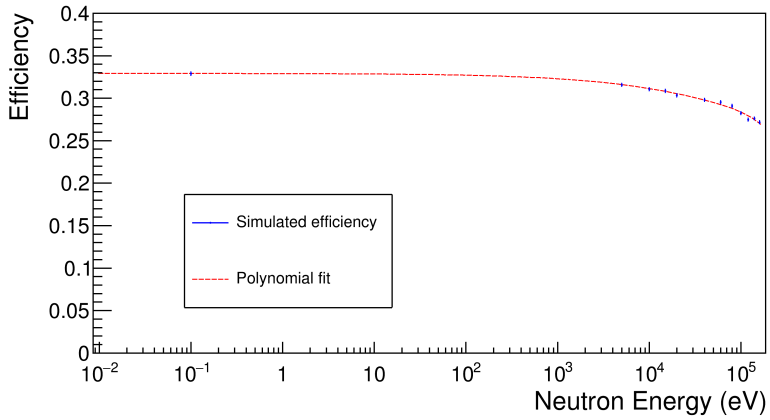

(b) B_b

Figure 4.17: Detector point-wise efficiency for the Boron detectors, and polynomial fit.

Chapter 5

Results

Even though the initial purpose of the experiment was to investigate the ^{235}U fission cross section in the neutron energy range between 10 keV and 30 keV [110], the combination of the unique features of the n_TOF neutron beam with the highly performing experimental apparatus, has led to high accuracy and high-resolution data in a much wider neutron energy range compared to previous measurements, from thermal to 170 keV. The present data, encompassing the full energy range in a single measurement, could definitively solve all the existing discrepancies with the most recent official libraries of neutron data.

In the present chapter, the ^{235}U(n,f) cross section calculated with the flux obtained combining the data of the two reference reactions is taken into account, in light of their good agreement. In addition, the ^{235}U(n,f) cross section respect to each reference have been calculated, since this have been required by the standard evaluators, and are currently available on EXFOR.

In the first section of this chapter the measured ^{235}U(n,f) cross section is compared to the values present in the major evaluated neutron data libraries, in the range between thermal and 170 keV. These libraries provide evaluated cross sections based on several experimental datesets of neutron induced reactions, which are mutually normalized. In particular the libraries taken into account and considered the most reliable are: the most recent ENDF/B-VIII and JEFF3.3, and the slightly older ENDF/B-VII and JENDL-4.0, which were available when the measurement has been pro-

posed in 2014. In section 5.2 only the last release of IAEA standard cross section [19] is taken into account, reporting the comparison for energies above 1 keV. The comparison in the energy region between 9 keV and 170 keV is then discussed in more detail, integrating the experimental and evaluated cross sections over wide energy intervals and highlighting the results concerning the statistically significant discrepancies found in the range 10 keV to 30 keV. Finally, the measured ratio between the ^{10}B(n,α) and ^{6}Li(n,t) cross sections is shown. It confirms the high quality of the measured data and it is also of great interest for the community of the evaluators of nuclear standard cross sections.

5.1 Comparison of ^{235}U(n,f) cross section with major libraries

The ^{235}U(n,f) cross section in the neutron energy range between 0.02 eV and 170 keV, is reported in the top panel of figure 5.1, with a logarithmic binning in the energy axis at 200 bins per decade (later indicated as BPD). In the same figure the comparison between experimental data and cross sections reported by ENDF/B-VIII (in red) and the JEFF3.3 (in blue) libraries is shown, using three statistical indicators at 20BPD, to highlights the possible discrepancies in terms of shape or average behaviour. In figure 5.2 the comparison is extended to the cross section values provided by ENDF/B-VII (green) and JENDL-4.0 (purple) libraries.

For each figure the χ^2 of the measured cross section with respect to each library is reported in the bottom part of the top panel, with the vertical axis on the right side of the panel. The χ^2 has been evaluated according to the expression:

$$\chi^2 = \frac{1}{10}\sum_{i=1}^{10}\frac{(xs_i^{exp} - xs_i^{lib})^2}{(\sigma_i^{exp})^2} \tag{5.1}$$

where xs^{exp} and xs^{lib} are the experimental and evaluated ^{235}U(n,f) cross section respectively and σ^{exp} is the experimental statistical uncertainty. This quantity is a useful indicator of the shape (dis)agreement. The middle panel shows the normalized deviation $\mathbf{\Sigma}$ in units of standard devi-

ation σ between the experimental data and the libraries calculated with the equation:

$$\mathbf{\Sigma} = \frac{\sum_{i=1}^{10}(xs_i^{exp} - xs_i^{lib})}{\sqrt{(\sigma_i^{exp})^2}} \tag{5.2}$$

Finally, the ratio data/library is reported in the bottom panel. While the ratio provides a numerical clue of the deviation in relative units, the normalized deviation $\mathbf{\Sigma}$ indicated the statistical relevancy of such difference.

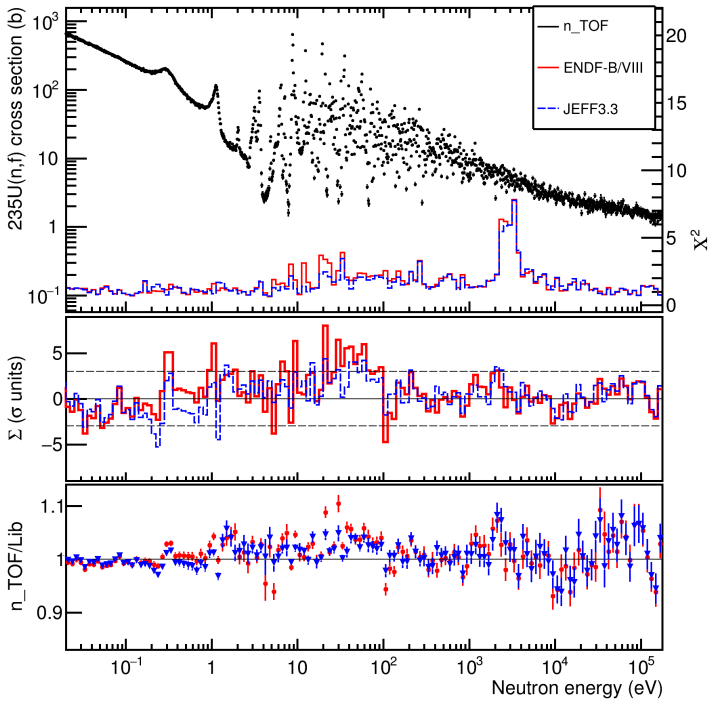

Figure 5.1: Top panel: the final measured ^{235}U(n,f) cross section, relative to the weighted average of the ^{6}Li(n,t) and ^{10}B(n,α) data; in the lower part the reduced χ^2 with respect to the ENDF/B-VIII (red) and the JEFF3.3 (blue) evaluations is shown. Middle panel: the normalized deviation Σ between the current data and the two libraries; the dashed lines indicate the $\pm 3\sigma$ level. Bottom panel: the ratio of the data to the two libraries.

In both figures 5.1 and 5.2 we can distinguish different behaviour of the cross section, corresponding to different energy intervals: below 1 eV,

between 1-100 eV, between 100-1000 eV and above 1 keV. In the first the experimental data agree with ENDF/B-VIII and JEFF3.3, indeed the ratios reported in the bottom panel of figure 5.1 agree within few percent and the χ^2 value is close to the unity over the full interval. Moreover below 1 eV $|\Sigma|$ is always smaller than 3σ with the exception of the small, but significant, difference at 0.25 eV, where the first resonance of ^{235}U(n,f) is located. The ratio and deviation highlight an experimental value initially lower than the libraries, followed by a higher value. The deviations reach values around 5 σ indicating a misalignment of the resonance energy between experimental data and the libraries. Nevertheless this issue does not affects the data quality and it will be shortly treated in a dedicated resonance analysis. On the contrary, the cross sections reported by ENDF/B-VII and the JENDL-4.0 present large discrepancies in term of deviation and ratio (up to 5%) below 1 eV, failing to reproduce correctly the experimental data.

Between 1 and 100 eV, where many resonances are located, large discrepancies between n_TOF data and all the libraries are present. Such discrepancies are most likely related to local mismatches in the amplitude or shape of some resonances. A larger value of χ^2 indicates a mismatch in terms of shape, while the sharp fluctuations of $\mathbf{\Sigma}$ denote a mismatch of the cross section integral, thus probably indicating a lower accuracy of the evaluation in that region. A better agreement has been found with the JEFF3.3 library, which has generally deviation $|\mathbf{\Sigma}|<4\sigma$ and slightly lower than ENDF/B-VIII, which in a few bins exceeds 5σ. The systematic differences in the ratio demonstrate that those deviations are not simply due to shape differences (χ^2»1), but a statistically systematic deviation around $\approx$ 3% between 1 and 100 eV is evident. The present data reveal the need to improve the evaluated ^{235}U fission cross section in this energy interval. In the next future these n_TOF data will undergo an accurate resonance analysis, in order to extract the required high precision resonance parameters. The agreement between the measured cross section and the ENDF/B-VII and JENDL-4.0 libraries resulted to be even worse, in particular the deviation $|\mathbf{\Sigma}|$ exceeds somewhere the value of 10σ and a systematic deviation around $\approx$ 5% is observed.

Above 100 eV the resonances are not well separated, mainly because of the Doppler broadening effect, and the statistical tools include several

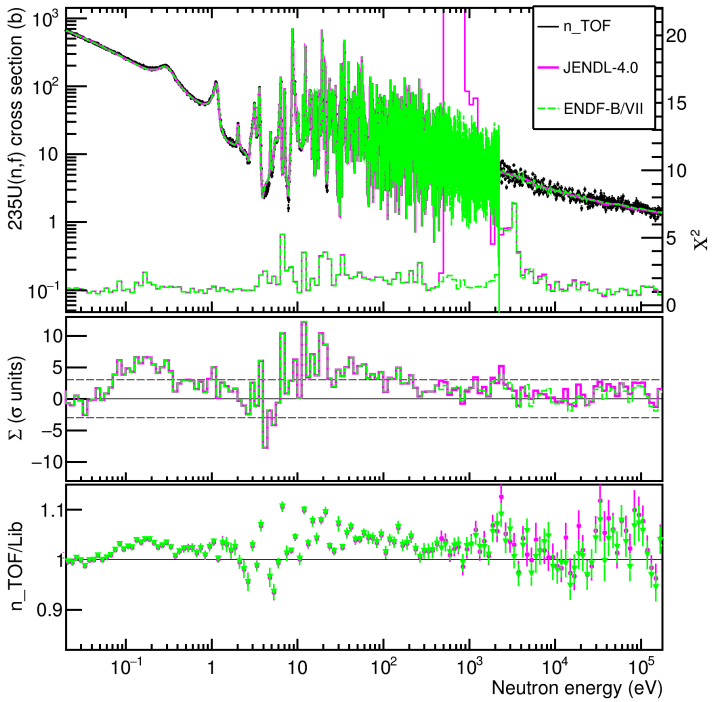

Figure 5.2: Top panel: the final measured ^{235}U(n,f) cross section, relative to the weighted average of the ^{6}Li(n,t) and ^{10}B(n,α) data; in the lower part the reduced χ^2 with respect to the ENDF/B-VII (green) and the JENDL-4.0 (purple) evaluations is shown. Middle panel: the normalized deviation $\mathbf{\Sigma}$ between the current data and the two libraries; the dashed lines indicate the $\pm 3\sigma$ level. Bottom panel: the ratio of the data to the two libraries.

of them in each bin, hence being sensitive to an average behaviour. Nevertheless the agreement between the experimental data and the libraries ENDF/B-VIII and JEFF3.3 is reasonably good up to $\approx$ 10 keV, showing a ratio n_TOF/Lib within $\approx$ 2% and deviation $|\mathbf{\Sigma}|$ lower than 3 σ almost everywhere. On the contrary the χ^2 distribution presents a large structure between 2.2 and 4 keV, not found in the other statistical indicators, that arises from the somewhat arbitrary definition of the boundary between resolved (RRR) and unresolved (URR) resonance regions. Indeed above 2.2 keV whilst resonance-like structures are present in n_TOF data, in

both libraries the cross section is reported with a smooth average shape. In the zoom shown in figure 5.3, the correspondence between the end of the RRR, that is the start of the smooth behaviour in the two libraries, and the sharp rise of χ^2, is even more evident. A similar structure of χ^2 is present in figure 5.2 with respect to ENDF/B-VII, since the boundary between the RRR and URR is the same of ENDF/B-VIII and JEFF3.3. The χ^2 calculated with respect to JENDL-4.0 presents a prominent structure with a sharp edge starting from 500 eV, where this library defines the RRR limit.

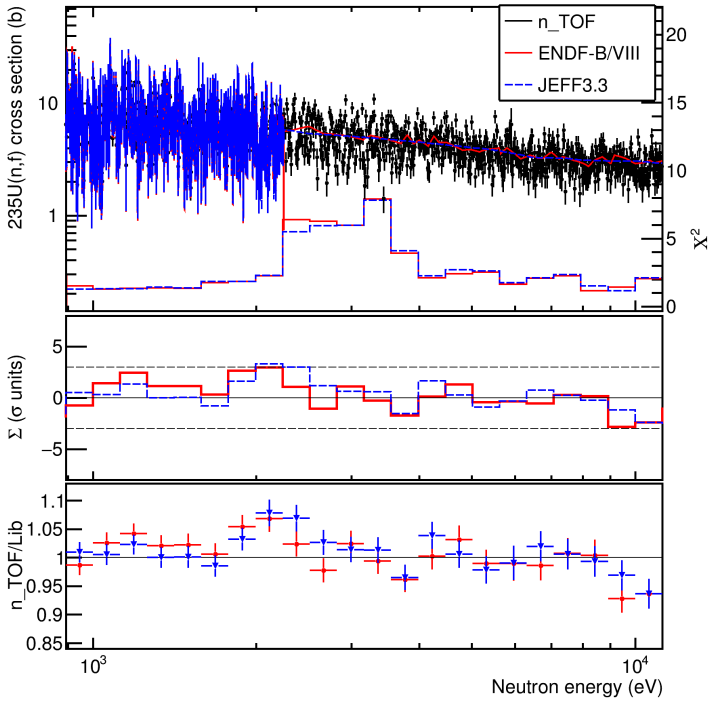

Figure 5.3: Top panel: the final measured ^{235}U(n,f) cross section, in the 1-10 keV neutron energy range; in the lower part the reduced χ^2 with respect to the ENDF/B-VIII (red) and the JEFF3.3 (blue) evaluations is shown. Middle panel: the normalized deviation Σ between the current data and the two libraries; the dashed lines indicate the $\pm 3\sigma$ level. Bottom panel: the ratio of the data to the two libraries.

The presence of resonance-like structures above the RRR boundary

has already been observed at n_TOF [111]. They arise from the grouping of individual resonances mainly due to the Doppler broadening. The level sequence of compound states distribution in ^{235}U+n was simulated just above the neutron separation energy S(n) = 6.544 MeV, assuming a Gaussian orthogonal ensemble (GOE) known as the Wigner surmise [112] and adopting an average level spacing D_0 = 0.54 eV. The ^{235}U(n,f) cross section, resulting from the simulated sets of neutron resonances and including the Doppler broadening at temperature T = 0 and at room temperature T = 300 K, has been calculated in a restricted neutron energy range, and was reported in Figure 5.4a. As ascertained by the simulation, for neutron energy below 4 keV the Doppler is the dominant effect that determines the resonance broadening. By reporting the experimental data in the same energy range as comparison (Figure 5.4b), one can observe that the resonance grouping resulting from the simulation is qualitatively compatible with the structures observed in the data.

For energy higher than $\approx$ 4 keV the χ^2 decreases rapidly, because of the increasing level density and worsening of the experimental resolution: no significant statement about possible structures in the measured cross section in this range is possible, so that it is well described by the smooth line provided by all the libraries. Nevertheless the data show systematic deviations from the evaluations, as can be clearly observed in figure 5.5. The trend is not unique: below 9 keV the n_TOF cross section agrees with the evaluations, whereas between 9 and 18 keV the experimental data are systematically lower, with $\mathbf{\Sigma}$ close to 3σ. For neutron energy above 30 keV a cross section slightly higher than evaluations has been measured. The observed discrepancy in the 10-30 keV region seems to confirm the previous indication of a shortcoming of major evaluated data libraries in that energy region [1], and therefore a more in-depth analysis has been carried out.

5.2 Comparison of ^{235}U(n,f) cross section with IAEA standard

The ^{235}U(n,f) cross section is provided by the IAEA in the form of GMA nodes[19], between 0.15 keV and 200 MeV, from which the cross section

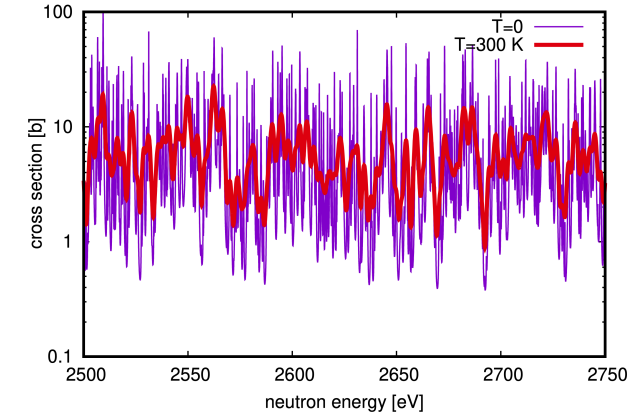

(a) Simulated

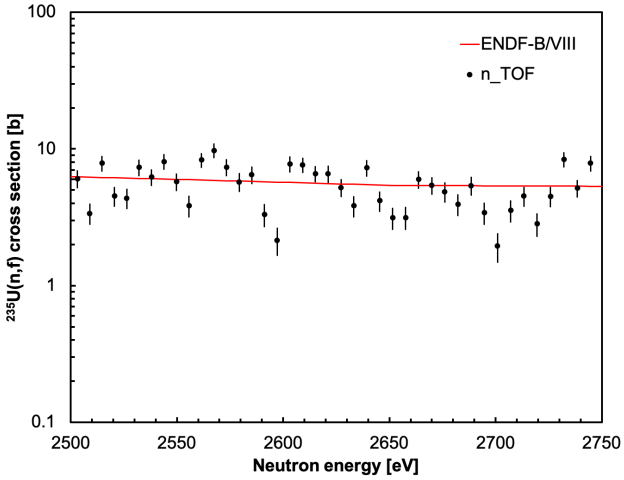

(b) Experimental

Figure 5.4: Top panel: simulation of the ^{235}U(n,f) cross section in a short energy interval where a resonance grouping, due primarily to Doppler broadening at T=300 K is evident. Bottom panel: n_TOF and ENDF/B-VIII cross section data in the same energy range.

can be calculated with a proper interpolation procedure between the so-called GMA nodes reported in table 5.1. This interpolation has been the subject of a recent Corrigendum[113], triggered by the present work, which clarified some ambiguities in the interpretation of the GMA nodes. Following the most recent prescriptions, the ^{235}U(n,f) cross section has

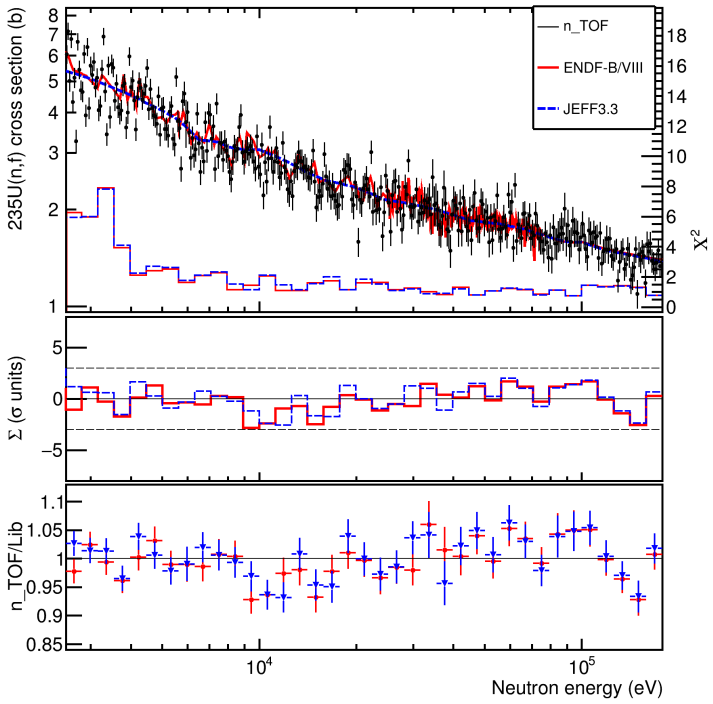

Figure 5.5: Top panel: the final measured ^{235}U(n,f) cross section, in the 2-170 keV neutron energy range; in the lower part the reduced χ^2 with respect to the ENDF/B-VIII (red) and the JEFF3.3 (blue) evaluations is shown. Middle panel: the normalized deviation Σ between the current data and the two libraries; the dashed lines indicate the $\pm 3\sigma$ level. Bottom panel: the ratio of the data to the two libraries.

been obtained by a logarithmic interpolation below 30 keV and linear interpolation above. The comparison between the IAEA cross section and the n_TOF data, in the neutron energy interval between 1 and 170 keV, is shown in figure 5.6. In the same figure the χ^2, $\mathbf{\Sigma}$ and ratio between the two cross sections are reported, in analogy with the comparison with the major evaluated libraries of section 5.1.

The interpolation procedure used to obtain the IAEA ^{235}U(n,f) cross section resulted in a smooth line, since the GMA nodes are quite distant in terms of neutron energy compared to the structures present in the n_TOF data. Not surprisingly, the χ^2 value below ≈ 4 keV is very large

Table 5.1: GMA nodes relative to the ^{235}U(n,f) cross section from [19].

Neutron energy (keV)	Cross Section [b]	Uncertainty [%]
0.950	7.50	1.3
1.50	7.30	1.3
2.50	5.39	1.3
3.50	4.78	1.3
4.50	4.26	1.3
5.50	3.84	1.3
6.50	3.30	1.3
7.50	3.24	1.3
8.50	3.01	1.3
9.50	3.12	1.3
15.0	2.49	1.3
20.0	2.34	1.8
24.0	2.16	1.3
30.0	2.07	1.3
45.0	1.85	1.3
55.0	1.81	1.3
65.0	1.75	1.3
75.0	1.67	1.3
85.0	1.60	1.3
95.0	1.57	1.3
100	1.58	1.3
120	1.49	1.3
150	1.43	1.3
170	1.39	1.4

if calculated with the formula 5.1. Furthermore below $\approx$ 2 keV the $\mathbf{\Sigma}$ and the ratio highlight large fluctuations, even though they are calculated with a small number of bins. For neutron energies larger than $\approx$ 2 keV the deviation $|\mathbf{\Sigma}|$ is always within the $\pm\sigma$ dashed lines, although in the interval 9-18 keV it reaches values close to 3σ and the ratio shows an average deviation of $\approx$ 5-6%. Above 30 keV the n_TOF and IAEA cross sections are substantially in good agreement and both the ratio and $|\mathbf{\Sigma}|$

behaviours are compatible with the statistical fluctuations.

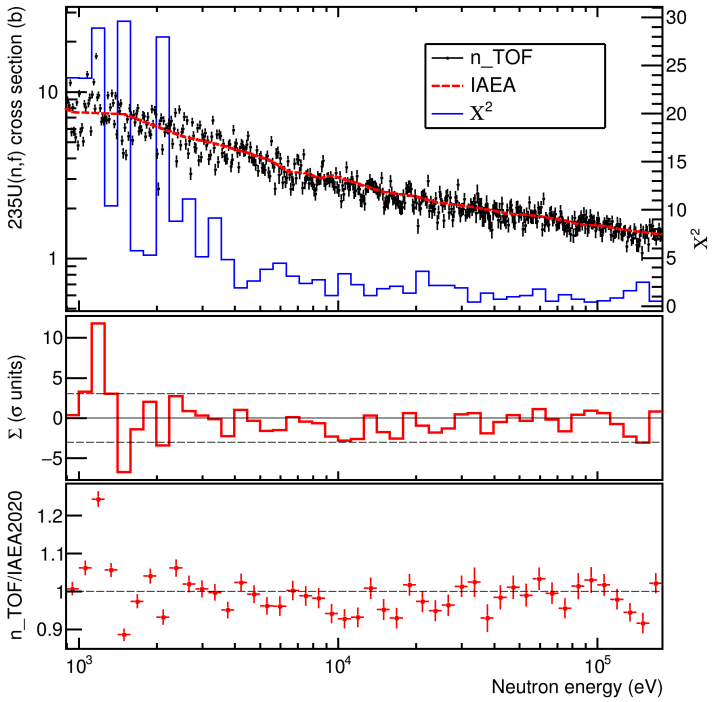

Figure 5.6: Top panel: the final measured ^{235}U(n,f) cross section, relative to the weighted average of the ^{6}Li(n,t) and ^{10}B(n,α) data; in the lower part the reduced χ^2 respect to the IAEA is shown. Middle panel: the normalized deviation $\mathbf{\Sigma}$ between the current data and the IAEA cross section; the dashed lines indicate the $\pm 3\sigma$ level. Bottom panel: the ratio of the current data to the IAEA cross section.

5.3 Integrals in keV energy region

For a more quantitative assessment of the observed discrepancy, figure 5.7 reports the ratio between the n_TOF measured cross section and the corresponding evaluated data of the main libraries, integrated in a few large intervals. The integral ranges have been chosen to investigate in detail the 10-30 keV neutron energy interval, where the discrepancies that motivated the measurement where found [1].

The evaluations from ENDF/B-VII, ENDF/B-VIII, JEFF3.3 and JENDL-4.0, together with the IAEA cross section have been taken into account for this comparison. In the 9-30 keV interval the n_TOF cross section presents a deviation between 1.5-2.5% relative to all the evaluations, with the exception of JENDL-4.0, highlighting a slight overestimate in the libraries. These deviations seemingly do not appear as statistically significant if the whole interval is considered, being $|\mathbf{\Sigma}|$ lower than 3σ with respect to all the evaluations. However, by splitting the energy interval in two sub-ranges, a large deviation up to 4.5% and a $\mathbf{\Sigma}$<-3 for the most recent evaluations is observed in the 9-18 keV region. In the second interval, 18-30 keV, the agreement is instead excellent. This is a significant confirmation that in that neutron energy range the cross section evaluations are overestimated and likely call for a revision of these libraries. In the other two intervals considered, 30-60 keV and 60-100 keV, the measured cross section is slightly larger than all the evaluations, whereas between 100 and 150 keV it agrees again within one standard deviation.

It is interesting to notice that the interpolation between GMA nodes, implies that a single inaccurate value of the cross section in a node can give rise to a systematic upward or downward shift of the interpolated cross sections in two adjacent energy intervals. In our case, the GMA node at 9.5 keV, where the IAEA reference cross section is markedly higher than measured in this work, influences the reconstructed cross section at higher energies, although a good agreement is observed for the node at 15 keV. Since the cross sections in the major evaluated libraries are based on the IAEA cross section it is not surprising that the most recent evaluations, namely ENDF/B-VIII and JEFF3.3, show results similar to the IAEA cross section. As a final remark, figure 5.7 also shows that the cross section integrated between 150 and 170 keV, *i.e.* where the ^{235}U(n,f) cross section is standard, is in very good agreement with the IAEA cross section and all the evaluations. This evidence further corroborates the robustness of the present results and the consequent conclusions.

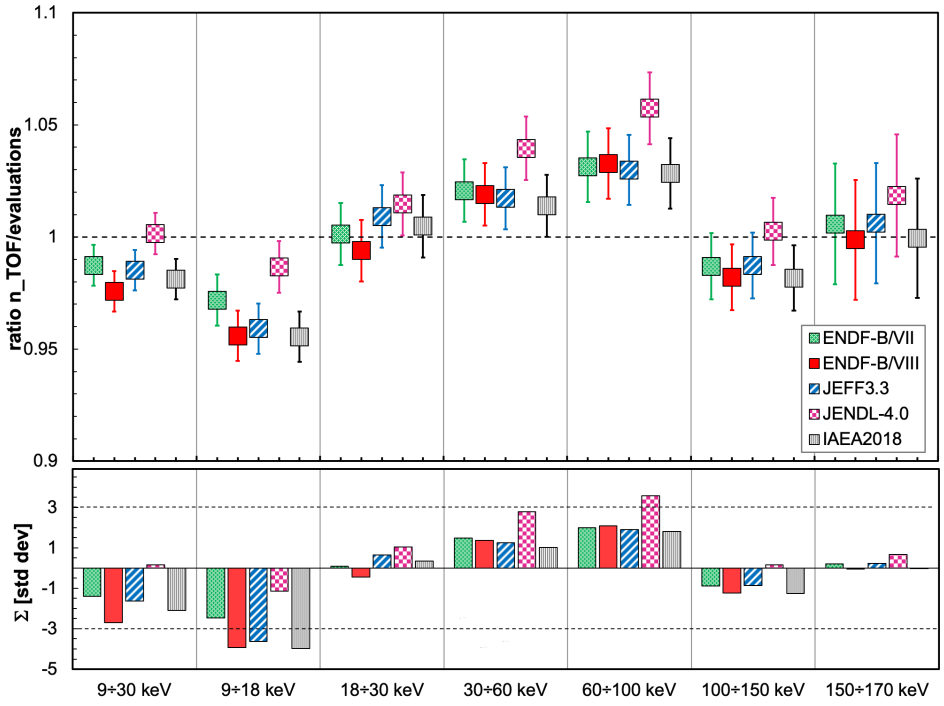

Figure 5.7: Top panel: ratio between the measured cross section, integrated in a few large intervals, and the corresponding values for the five reference libraries ENDF/B-VII, ENDF/B-VIII, JEFF3.3, JENDL-4.0, IAEA. Bottom panel: the corresponding normalized deviation $|\mathbf{\Sigma}|$ (standard deviation units).

5.4 Ratio between ^{10}B(n,α) and ^{6}Li(n,t) cross sections

Even though the use of two reference standard reactions was initially motivated by redundancy issues and in order to ensure the robustness of the results, the ratio between the two cross sections is of great interest for the neutron standards working group of IAEA. Indeed the ^{10}B(n,α) and ^{6}Li(n,t) are often used as references for neutron energies from 0.0253 eV to 1 MeV, thanks to the easy handling of such stable isotopes and their large cross section combined with a positive reaction Q-value. In fact these reactions are usually employed to measure the n_TOF neutron flux

between thermal and a few hundred keV, using silicon [63, 114] and gas detectors [64, 65].

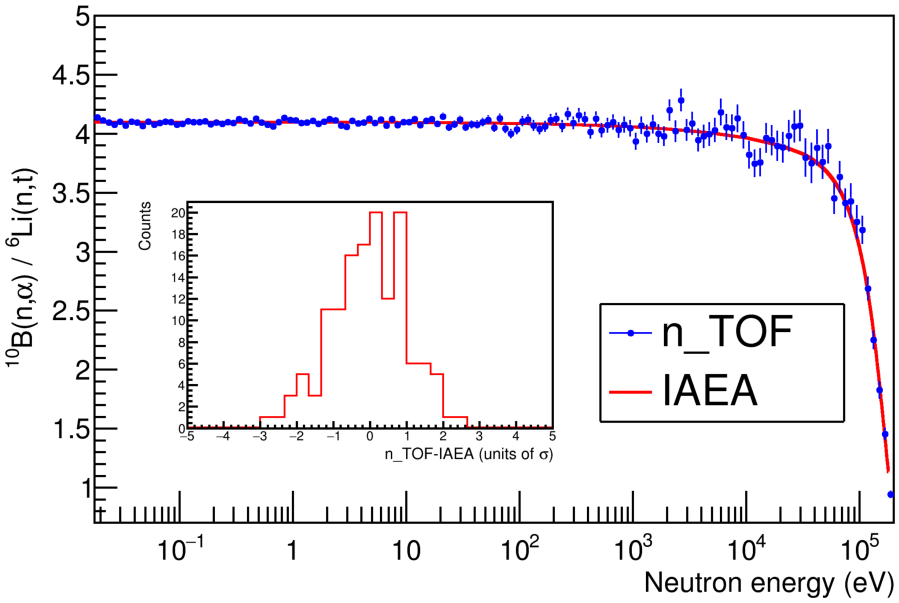

Figure 5.8: Experimental ratio between the ^{10}B(n,α) and ^{6}Li(n,t) cross sections normalized in the interval between 1 and 10 eV (blue points), compared with IAEA values (red line). The inset shows difference between the n_TOF data and the standard value measured in units of standard deviation σ.

Figure 5.8 shows the ratio between the ^{10}B(n,α) and ^{6}Li(n,t) cross sections, normalized to their standard values in the interval between 1 and 10 eV. The blue points represent the n_TOF data, while the red curve is the ratio between the IAEA cross sections. The experimental data agree with the IAEA values over the full range, even though the fluctuation due to the poor B statistic are significant above 1 keV. In the inset the difference between the n_TOF data and the standard value measured in units of standard deviation σ is reported for each point of the B/Li ratio. The Gaussian-shape of the distribution proves that the fluctuations are purely statistic. The present results confirm the good quality of the cross section value for the reactions ^{10}B(n,α) and ^{6}Li(n,t) present in the last release of IAEA standards. At the moment a dialogue with the evaluators

is ongoing to include the present data in the next standard evaluation.

5.5 Systematic uncertainties

According to the datasheet of the samples, the systematic uncertainties on their areal densities were 1% for U, 1.5% for Li and 6% for B. However, these uncertainties do not play any role, since the data were normalized during the analysis, as shown in section 3.8. Two additional sources has been investigated, namely the sensitivity to the experimental threshold used to select the reaction products and the dependence of the detection efficiency from the position of the neutron beam on the sample.

The first contribution impacts the number of counts measured in each detector and has been studied variating the selection threshold by $\pm$1%, $\pm$2% and $\pm$3%. Figures 5.9 and 5.10 shows the ratio of the count rates obtained with these threshold with respect to the default values, for a Li and B detector respectively. Small differences are observed for neutron energies larger than 1 keV, however these are <0.3% in the case of Li and <1% for B. Because of the wide separation between alphas and fission fragments, the sensitivity to the selection thresholds was negligible in the case of U detectors.

The contribution due to the alignment of the setup has been investigated by simulating the Li and B efficiency considering different positions of the beam on the samples. The effective beam center position was measured with the Gafchromic foil at 10.0 (7) mm and 5.0 (7) mm, respectively in the horizontal and vertical direction, with respect to the detector center. The efficiency has been simulated considering a shift of $\pm$2 mm (corresponding to 3σ) in both the direction. Such a shift determines a slight change of the efficiency, roughly linear with the displacement, resulting < 1% for a shift of one standard deviation. Finally, the IAEA indicates the presence of a unrecognized systematic uncertainty on the values we used for normalization, which has been taken in account. Combining all the sources in quadrature, the overall systematic uncertainty ranges from 1.2% below 1 keV to 1.5% above this neutron energy.

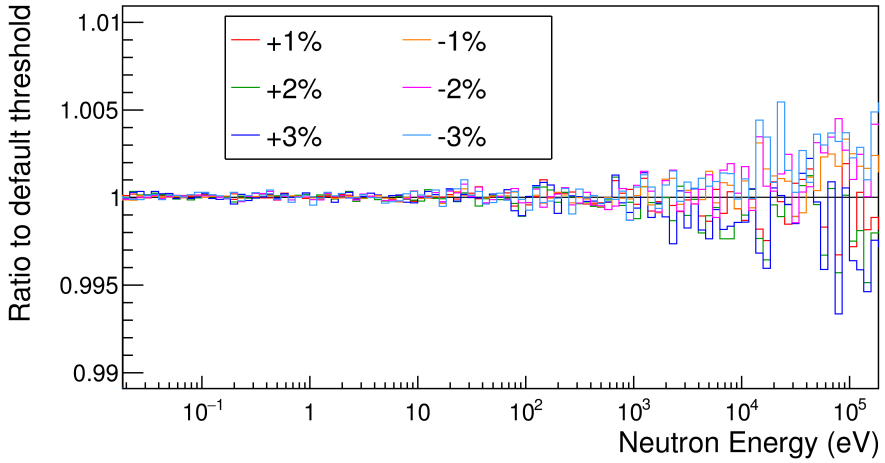

Figure 5.9: Ratio between the count rates measured with different thresholds and the default values for the Li_b detector.

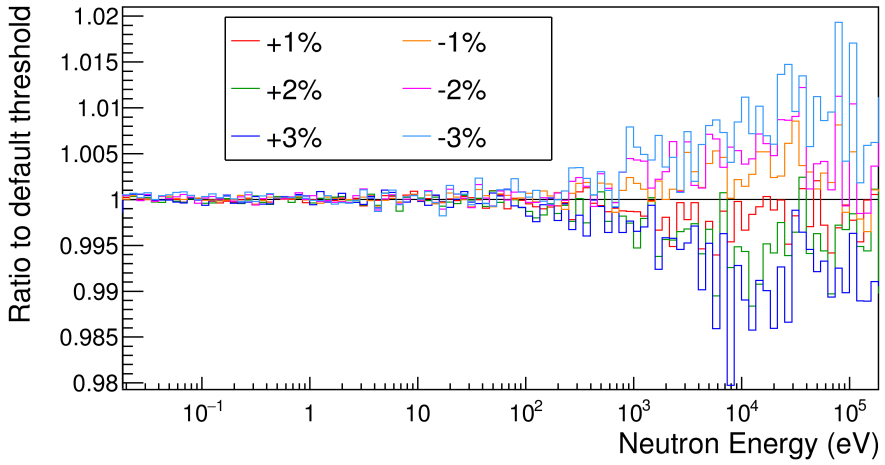

Figure 5.10: Ratio between the count rates measured with different thresholds and the default values for the B_f detector.

Conclusions

The present P.h.D. thesis describes the high resolution measurement of the ^{235}U(n,f) cross section, relative to ^{6}Li(n,t) and ^{10}B(n,α), performed at the n_TOF facility in 2016. This experiment was proposed after that recent measurements [1, 2] have drawn the attention to a possible discrepancy in the neutron energy range between 10 keV and 30 keV interpreted as an overestimation in the evaluations of the ^{235}U(n,f) cross section. The interest for this cross section derives from his role as *neutron standard*, being employed as a reference in the measurement of neutron fluxes and neutron induced reaction cross sections.

The measurement has been performed in the Experimental Area 1 of n_TOF, where a neutron beam with excellent energy resolution and high instantaneous flux was available. The experimental apparatus consisted of stacks of samples and silicon detectors placed directly in the neutron beam. It represented the first time a fission cross section has been measured with silicon detectors at n_TOF, that have proven to be extremely stable and resistant to the radiation damages.

In order to ensure the robustness of the final results, several checks were made during each stage of the data analysis. In particular, the consistency between the fluxes measured with each reference reaction was verified, as well as their agreement with the official n_TOF flux measured in 2011. Monte Carlo simulations were performed with a Geant4 code, to calculate the neutron absorption in the materials placed along the beam and the detectors efficiency as a function of the neutron energy. In particular the direct simulation of the reaction products represented

an important solution to overcome the requirement of high computing resources by neutrons but, at the same time, it required additional validation stages. A relevant phase of the analysis consisted in the experimental data normalization, indeed the experimental ^{235}U(n,f) cross section has been normalized using the standard integral between 7.8 eV and 11 eV in order to reduce the systematic uncertainties. Nevertheless, the consistency with the thermal point was also verified, in fact the ratio between thermal and the integral resulted to be 2.352 ± 0.013(stat) $\pm$ 0.007(syst) eV^{-1}, in agreement with the value reported by IAEA (2.373 ± 0.029 eV^{-1}).

The ^{235}U(n,f) n_TOF cross section was extracted relative to the weighted average of the two reference reactions from thermal energy to 170 keV and compared with the values provided by the major nuclear data libraries (ENDF/B-VIII, JEFF3.3, ENDF/B-VII, JENDL-4.0 and IAEA2018). The data are in good agreement with the libraries up to 10 eV, while statistically significant differences are observed in the resolved resonance region. Moreover, the presence of structures in the cross section is observed between 2.2 keV and 4 keV, arising from the grouping of individual resonances, which are not reported by the libraries.

The interval from 1 keV to 100 keV has been investigated in detail, by integrating the cross section over several energy ranges of interest. A good agreement is generally observed between the n_TOF data and the libraries with the exception of the 9-18 keV interval, where a statistically significant overestimation $\approx 5\%$ is present. Noteworthy, such difference can justify the experimental evidences which motivated the measurement. Moreover, since the IAEA cross section is provided as point-wise values which should to be interpolated, the n_TOF results suggest that the observed discrepancy may be due to an overestimation of the value at 9.5 keV, which determines the cross section in its surroundings. The robustness of the present results is further ensured by the good agreement with all the libraries in the energy interval from 150 keV to 170 keV, where the ^{235}U(n,f) cross section is a standard. The new n_TOF datasets, one for each reference reaction, may lead to a reduction of the uncertainty in the 1-100 keV energy region, with the perspective to possible extend the ^{235}U(n,f) standard energy interval toward lower values.

This accurate measurement can have a relevant impact in several fields, ranging from nuclear energy technology and the development of new so-

lution for handling radioactive waste to the refinement of theoretical fission models, which recently are of particular interest for the modeling of the heavy elements nucleosynthesis in explosive environment. Moreover, the excellent behaviour of the silicon detectors offers the perspective to investigate the fission chains performing systematic campaigns of fission cross section measurements for several isotopes of the same element.

Finally, this measurement provided a new dataset of the ratio between ^{10}B(n,α) and ^{6}Li(n,t) cross sections, which shows a good agreement with the IAEA values. In addition, it resulted to be a dataset of interest for the next evaluation of the standard cross sections.

Acknowledgments

Per mia natura, mettere per iscritto pensieri personali non è il mio forte, ma questi tre anni non possono passare senza lasciare tracce. Il primo pensiero è per Gigi, per essere stato sempre una guida paziente e sempre presente, soprattutto quando c'è stato da evidenziare qualche mancanza letteraria o cinematografica. Subito accanto Paolo, grande maestro di excel e nuova star del twitter (#pfcovidplots), esempio di lucidità e metodo scientifico.

Un ringraziamento ad Alice, in tre anni ne è passata di acqua sotto i ponti, ma ancora ci sopportiamo e complimenti per la vittoria indiscussa della CovidCup2020! Grazie alla famiglia n_TOF, in particolare a Massimo che spero di avere ancora attorno nel futuro, ai bolognesi, da cui in fondo tutto è iniziato: Cristian, Gianni, Alberto M. e Alberto V. a Mario per la sua schiettezza e a Nicola per avermi aiutato a tenermi in linea, chiedendomi se fossi ingrassato ad ogni meeting in persona.

Catania, e i Laboratori del Sud in particolare, sono stati per questi tre anni una seconda casa, dove ho avuto la possibilità di conoscere persone semplicemente eccezionali. A cominciare dallo zio Alfio e la sua saggezza inossidabile a Mimmo con la classe musicale (e non solo). Grazie ai ragazzacci di Ettore, che hanno trasformato le pause pranzo, al Presidente David che è impossibile cogliere impreparato, a Maria e il suo cuore immenso, a Peppe (ancora abbiamo quella partita di football da vedere assieme) e in particolare ad Eugenia, che non so come faccia ancora a sopportare il mio modo di fare. Sono stati anni più spacchiusi anche per merito delle storie di Gianfranco (pragmatico, ironico, scettico,

razionale e saittuni di catena), la leggerezza e sconfinata cultura musicale dello sbraccamenatore Gianni – pardòn Giorgio – ed Enza, che mi ha insegnato l'importanza di condividere.

Un grazie agli amici di vecchia data, che anche da lontano non si sono persi ai tre dell'Ave Maria con cui spartisco il tempo da oramai oltre 23 anni (and counting) Ales, Paso e Mircus. Ai regiz degli anni '90, con cui a sto punto ho messo assieme una scusa per fare una cena! A Betta, unica persona che ho convinto a provare eu4, conquista che supera di gran lunga il dottorato. Ai ragazzi del Grande Torino Campo e buon Poldo con cui prima o poi vinceremo sto Mondiale. A Silvia, che mi ricoda ogni domenica mattina quanto siano diversi i nostri ritmi di sonno/veglia. A Fra che ha sempre saputo darmi il consiglio giusto. Grazie agli amici di Vicchio, che mi han sempre fatto tenere a mente l'importanza del pensiero laterale.

Tre anni sono lunghi, ma da casa non è mai mancato l'appoggio e il sostegno per ciò che stavo facendo. A cominciare dagli zii Giuliana e Marcello, Dada Franca e Mauro, Babbo, Mamma e Giulia (e perché no? Mauri e Piera).

Bibliography

[1] M. Barbagallo et al., European Physical Journal A **49**, 156 (2013).

[2] M. Jandel et al., Physical Review Letters **109**, 202506 (2012).

[3] J. Chadwick, Royal Society London **A136**, 692 (1932).

[4] E. Fermi, Nature **133**, 757 (1934).

[5] E. Fermi, Nature **133**, 898 (1934).

[6] F. Strassmann O. Hahn, L. Meitner, Naturwissenschaften **26**, 475 (1938).

[7] O. Frisch L. Meitner, Nature **143**, 471 (1939).

[8] O. Frisch, Nature **143**, 276 (1939).

[9] N. Bohr and J.A. Wheeler, Physical Review **56**, 426 (1939).

[10] G. Gamow, Procedings of the Royal Society **126**, 632 (1930).

[11] C.F. von Weizsacker, Zeitschrift fur Physik A Hadrons Nuclei **96**, 431 (1935).

[12] A. Stamatopoulos, Study of the 240Pu(n,f) and 237Np(n,f) reaction cross sections at the new experimental area (EAR2) of the CERN n_TOF facility, 2019.

[13] S. Cohen and W.J. Swiatecki, Annals of Physics **19**, 67 (1962).

[14] V.M. Strutinsky, Nuclear Physics A **122**, 1 (1968).

[15] A. Tsinganis, Measurement of the 242Pu(n,f) reaction cross-section at the CERN n TOF facility, 2014.

[16] S. Bjornholm and J.E. Lynn, Review Modern Physic **52**, 725 (1980).

[17] W.E. Shoupp and J.E. Hill, Physical Review **77**, 785 (1949).

[18] Yu.V.Melikov et al., Nuclear Physics A **180**, 241 (1972).

[19] A.D. Carlson et al., Nuclear Data Sheets **148**, 143 (2018).

[20] A.D. Carlson et al., Nuclear Data Sheets **110**, 3215 (2009).

[21] M.B. Chadwick et al., Nuclear Data Sheets **107**, 2931 (2006).

[22] W.P. Poenitz, Report BNL-NCS-51363 **1**, 249 (1981).

[23] S.E. Aumeier W.P. Poenitz, The simultaneous evaluation of the standards and other cross sections of importance for technology, 1997.

[24] F. Tovesson et al., Physical Review C **79**, 014613 (2009).

[25] D. Karadimos et al., Physical Review C **89**, 044606 (2014).

[26] M. Diakaki et al., Physical Review C **93**, 034614 (2016).

[27] F. Belloni et al., European Physic Journal A **49**, 2 (2013).

[28] IAEA, `www.iea.org/reports/electricity-information-overview`.

[29] J. Magill et al., Nuclear Energy **42**, 263 (2003).

[30] J. Magill et al., Nuclides.net: An integrated Environment for Computations on Radionuclides and their Radiation, 2003.

[31] NEA OECD, Accelerator-driven Systems (ADS) and Fast Reactors (FR) in Advanced Nuclear Fuel Cycles (2002), `www.oecd-nea.org/ndd/reports/2002/nea3109.html`.

[32] A. Stanculescu, Annals of Nuclear Energy **62**, 607 (2013).

[33] R.H. Cyburt et al., Reviews of Modern Physics **88**, 015004 (2016).

[34] C. Pitrou et al., Physics Reports **754**, 1 (2018).

[35] N. Prantzos, Astronomy&Astrophysics **542**, A67 (2012).

[36] W.M. Howard et al., The Astrophysical Journal **175**, 201 (1972).

[37] S. Curtis, The Astrophysical Journal **870**, 2 (2019).

[38] F. Hoyle et al. E.M. Burbidge, G.R. Burbidge, Review Modern Physics **29**, 547 (1957).

[39] A.G.W. Cameron, Stellar Evolution, Nuclear Astrophysics, and Nucleogenesis, 1957.

[40] J.J. Cowan et al., Origin of the Heaviest Elements: the Rapid Neutron-Capture Process, 2020, `arXiv:1901.01410`.

[41] R. Reifarth et al., Journal of Physics G **41**, 053101 (2014).

[42] D. Käppeler et al., Review of Modern Physics **83**, 157 (2011).

[43] O. Straniero et al., The Astrophysical Journal **440**, 85 (1995).

[44] J.J. Cowan et al., Physics Reports **208**, 267 (1991).

[45] M. Arnould et al., Physics Reports **450**, 97 ((2007)).

[46] J.M. Lattimer et al., The Astrophysical Journal **192**, L145 (1974).

[47] K. Thielemann et al., Annual Review of Nuclear and Particle Science **67**, 253 (2018).

[48] D.N. Schramm et al., The Astrophysical Journal **185**, 293 (1973).

[49] A. Arcones and F-K Thielemann, Journal of Physics G **40**, 013201 (2013).

[50] J.W. Truran et al., The Astrophysical Journal **222**, L63 (1978).

[51] M. Obergaulinger et al., Journal of Physics G **45**, 084001 (2018).

[52] E.M.D. Symbalisty et al., The Astrophysical Journal **291**, L11 (1985).

[53] M. Obergaulinger et al., Journal of Physics G **45**, 084001 (2018).

[54] F-K Thielemann et al., Zeitschrift für Physic A Hadronic Nuclei **309**, 301 (1983).

[55] N. Vassh et al., Journal of Physics G **46**, 065202 (2019).

[56] S. Goriely and G. Martinez-Pinedo, Nuclear Physic A **944**, 158 (2015).

[57] J. Lippuner and L.F. Roberts, The Astrophysical Journal **233**, 18 (2017).

[58] N. Colonna et al., European Physic Journal A **56**, 48 (2020).

[59] C. Zhang et al., Physical Review C **94**, 064323 (2016).

[60] M.R. Mumpower et al., Physical Review C **101**, 054607 (2020).

[61] N. Vassh et al., The Astrophysical Journal **896**, 28 (2020).

[62] Wu et al., Physical Review Letters **122**, 062701 (2019).

[63] S. Marrone et al., Nuclear Instruments and Methods in Physics Research A **517**, 389 (2004).

[64] I. Giomataris et al., Nuclear Instruments and Methods in Physics Research A **376**, 29 (1996).

[65] S. Andriamonje et al., Journal of the Korean Physical Society **59**, 1597 (2011).

[66] D.B. Gayther et al., Metrologia **27**, 221 (1990).

[67] C. Paradela et al., Physical Review C **82**, 034601 (2010).

[68] D. Tarrio et al., Physical Review C **83**, 044620 (2011).

[69] K. Shibata et al., Journal of Nuclear Science and Technology **48**, 1 (2011).

[70] N. Otuka et al., Nuclear Data Sheets **120**, 272 (2014).

[71] M. S. Moore et al., Physical Review C **18**, 1328 (1978).

[72] G. A. Keyworth J. R. Lamley and B. C. Diven, Nuclear Science and Engineering **43:3**, 281 (1971).

[73] C. Wagemans and A.J. Deruytter, Annals of Nuclear Energy **3**, 437 (1976).

[74] R.B.Perez et al., Nuclear Science and Engineering **55**, 203 (1974).

[75] C. Rubbia et al., CERN-LHC-98-002-EET, 1998, `http://cds.cern.ch/record/357112`.

[76] R. Serber et al., Physical Review **72**, 1114 (1947).

[77] J.-C. David et al., European Physic Journal A **51**, 68 (2015).

[78] A. Boudard et al., Physical Review C **87**, 014606 (2013).

[79] J.P. Bondorf et al., Nuclear Physics A **443**, 321 (1985).

[80] J.P. Bondorf et al., Nuclear Physics A **444**, 460 (1985).

[81] H.W. Barz et al., Nuclear Physics A **448**, 753 (1986).

[82] E. Fermi, Nuclear Physics A **5**, 570 (1950).

[83] E. Chiaveri et al., Journal of the Korean Physical Society **59**, 1620 (2011).

[84] M. Calviani et al., Roadmap for the Implementation of a New Target Mobile Shielding and a NEAR Experimental Station at the n_TOF Facility, 2019, eDMS 2158356 v.1.0, TOF-PM-WD-0001 v.1.0.

[85] M. Flaska et al., Nuclear Instruments and Methods in Physics Research A **531**, 392 (2004).

[86] R. Reifarth et al., Nuclear Instruments and Methods in Physics Research B **241**, 176 (2005).

[87] K. Kino et al., Nuclear Instruments and Methods in Physics Research A **58**, 626 (2011).

[88] D.B.Syme et al., Nuclear Instruments and Methods in Physics Research **198**, 357 (1928).

[89] M. Barbagallo et al., Physical Review Letters **117**, 152701 (2016).

[90] L. Damone et al., Physical Review Letters **121**, 042701 (2018).

[91] F. Gusing et al., Physical Review C **85**, 064601 (2012).

[92] N. Larson, Updated Users' Guide for SAMMY: Multilevel R-Matrix fits to neutron data using Bayes' equations, 2006, oRNL/TM-9179/R8 ENDF-364/R2.

[93] C.J. Dean M.C. Moxon, T.C. Ware, REFIT-2009 A Least-Square Fitting Program for Resonance Analysis of Neutron Transmission, Capture, Fission and Scattering Data, 2010, users' Guide for REFIT-2009-10.

[94] C. Coceva et al., Nuclear Instruments and Methods in Physics Research A **489**, 346 (2002).

[95] G. Battistoni et al., AIP Conference Proceedings **896**, 31 (2006).

[96] J. Ranft A. Fassò, A. Ferrari, Fluka: A multiparticle transport code, 2005, technical Report CERN-2005-10, INFN/TC 05/11, SLAC-R-73.

[97] L.S. Waters et al., AIP Conference Proceedings **896**, 81 (2007).

[98] G. Lorusso et al., Nuclear Instruments and Methods in Physics Research A **532**, 622 (2004).

[99] Ming-Chen Hsiao and Shiang-Huei Jiang, Applied Radiation and Isotopes **143**, 79 (2019).

[100] `http://www.mesytec.com/product-list.html#multichanneLipreamps`.

[101] `https://www.ortec-online.com/products/electronics/amplifiers/474`.

[102] A. Masi et al., The CERN n_TOF facility data acquisition system, 2017.

[103] Daniel C. van der Ster et al., Journal of Physics **664**, 042054 (2015).

[104] P. Zugec et al., Nuclear Instruments and Methods in Physics Research Section A **812**, 134 (2016).

[105] F.J. Harris, PROCEEDINGS OF THE IEEE **66**, 51 (1978).

[106] S. Agostinelli et al., Nuclear Instruments and Methods in Physics Research A **506**, 250 (2003), official web site: http://geant4.cern.ch/.

[107] S. Lo Meo et al., European Physic Journal A **51**, 160 (2015).

[108] J. Pancin et al., Nuclear Instruments and Methods in Physics Research A **524**, 102 (2004).

[109] F. Belloni et al., Physica Scripta **T150**, 014004 (2012).

[110] M. Barbagallo et al., High accuracy measurement of the ^{235}U(n,f) reaction cross-section in the 10-30 keV neutron energy range, 2014.

[111] C. Lederer et al., Physical Review C **83**, 034608 (2011).

[112] M.V. Berry and P. Shukla, Journal of Physics A: Mathematical and Theoretical **42**, 485102 (2009).

[113] A.D. Carlson et al., Nuclear Data Sheets **163**, 280 (2020).

[114] L. Cosentino et al., Review of Scientific Instruments **86**, 073509 (2015).